SLAC – 320
UC – 34D
(E)

MEASUREMENT OF THE B HADRON LIFETIME*

René Ashwin Ong

Stanford Linear Accelerator Center
Stanford University
Stanford, California 94305

September 1987

Prepared for the Department of Energy
under contract number DE-AC03-76SF00515

Printed in the United States of America. Available from the National Technical Information Service, U.S. Department of Commerce, 5285 Port Royal Road, Springfield, Virginia 22161. Price: Printed Copy A11, Microfiche A01.

* Ph.D. Dissertation

Abstract

This thesis presents an experimental determination of the average B hadron lifetime. B hadrons, particles that contain bottom quarks, are produced from electron-positron collisions in the PEP storage ring at a center of mass energy of 29 GeV. Using data taken by the Mark II detector, the decays of B hadrons are tagged by identifying leptons at high transverse momentum relative to the event axis. By means of a precision inner drift chamber, the impact parameters of these lepton tracks are measured with respect to the B hadron production point. From this impact parameter distribution, the average B hadron lifetime is then deduced. Based on a sample of 617 leptons, this lifetime is found to be:

$$\tau_b \;=\; (0.98 \pm 0.12 \pm 0.13) \times 10^{-12} \text{ sec} \;,$$

where the first error is statistical and the second systematic.

It is believed that the B hadron lifetime is largely determined by the lifetime of the bottom quark. This thesis therefore presents a measurement of a fundamental property of bottom quark decay via the weak interaction. In addition, in conjunction with other experimental results, this measurement can be used to place constraints on models of quark mixing.

Acknowledgments

This thesis builds upon the careful and detailed work of a great many people. First and foremost, I wish to thank all the members, past and present, of the Mark II collaboration. With pleasure, I acknowledge the guidance and motivation provided by my advisor John Jaros, and the help and warm friendship offered to me by my office-mate Ken Hayes. These gentlemen were always available for long discussions and keen insight concerning my work. I also thank Lydia Beers for much assistance and *joie de vivre* over the years.

The measurement presented in this thesis uses many of the ideas (and even some of the bug-free computer code) of physicists who have done similar analyses on the Mark II experiment, namely Nigel Lockyer, Larry Gladney, Dan Amidei, and Mark Nelson. I received invaluable day-to-day help from my comrades Ray Cowan, Keith Riles, Dean Karlen, and Bruce LeClaire, and numerous useful suggestions from George Trilling and Vera Lüth. I also acknowledge the members of my Ph.D. committee, the staff and faculty of the Stanford Physics department, and all the people who helped proofread the thesis.

I first became interested in science from discussions with my father. After discovering I was too messy for chemistry, I turned to particle physics thanks to the motivating influences of Dan Sinclair, Howard Gordon, and Larry Sulak. I ended up at Stanford largely because of the encouragement of Martin Perl, who has been especially supportive of me over the years.

Graduate school was a wonderful experience, in no small part because of the friends that I have made. I will miss Chris Wendt and Alex Harwit, roommates that have put up with me. I will also fondly remember time spent with Natalie Roe, tennis matches with Fred Bird, and dinners with Patricia Stuart. My good pals Robert Johnson and Steve Wagner have helped me to enjoy myself, and the love of Anna Green has brightened up my life. Most of all, however, it was the strong and enduring friendship of Harry Nelson, and the love from my parents and sister, that helped me to complete this endeavour.

Table of Contents

List of Tables

List of Figures

Introduction

This thesis presents an experimental determination of the lifetime of hadrons containing bottom quarks (B hadrons). B hadrons are produced from electron-positron collisions in the PEP storage ring at a center of mass energy of 29 GeV. These hadrons travel a short distance (typically 600 μm) and decay via the weak interaction into a number of particles. The decay particles are then observed in the Mark II detector which surrounds the interaction point. Approximately 25 % of B hadrons decay to leptons (an electron, muon, or tau). Because of the heavy bottom quark mass, these leptons often carry a large amount of momentum perpendicular to the original quark direction. This transverse component of momentum (p_t) is used to separate B hadron decays from the decays of lighter hadrons. Figure 1.1, shows a high p_t lepton event observed in the Mark II detector.

Since the lepton track is reliably known to have come from B hadron decay, its trajectory contains information about the parent lifetime. In this thesis, we measure the distance of closest approach between the lepton track and the point where the B is produced. The B hadron lifetime is then determined from the distribution of such distances for a sample of 617 lepton tracks.

The remainder of this chapter provides a brief summary of the relevant theoretical considerations associated with the measurement. The Standard Model of electro-weak interactions is introduced, followed by a description of heavy quark production and decay. The possible constraints on Standard Model parameters from the B lifetime measurement are discussed. At the end of the chapter, the analysis objectives and an outline of the thesis are presented.

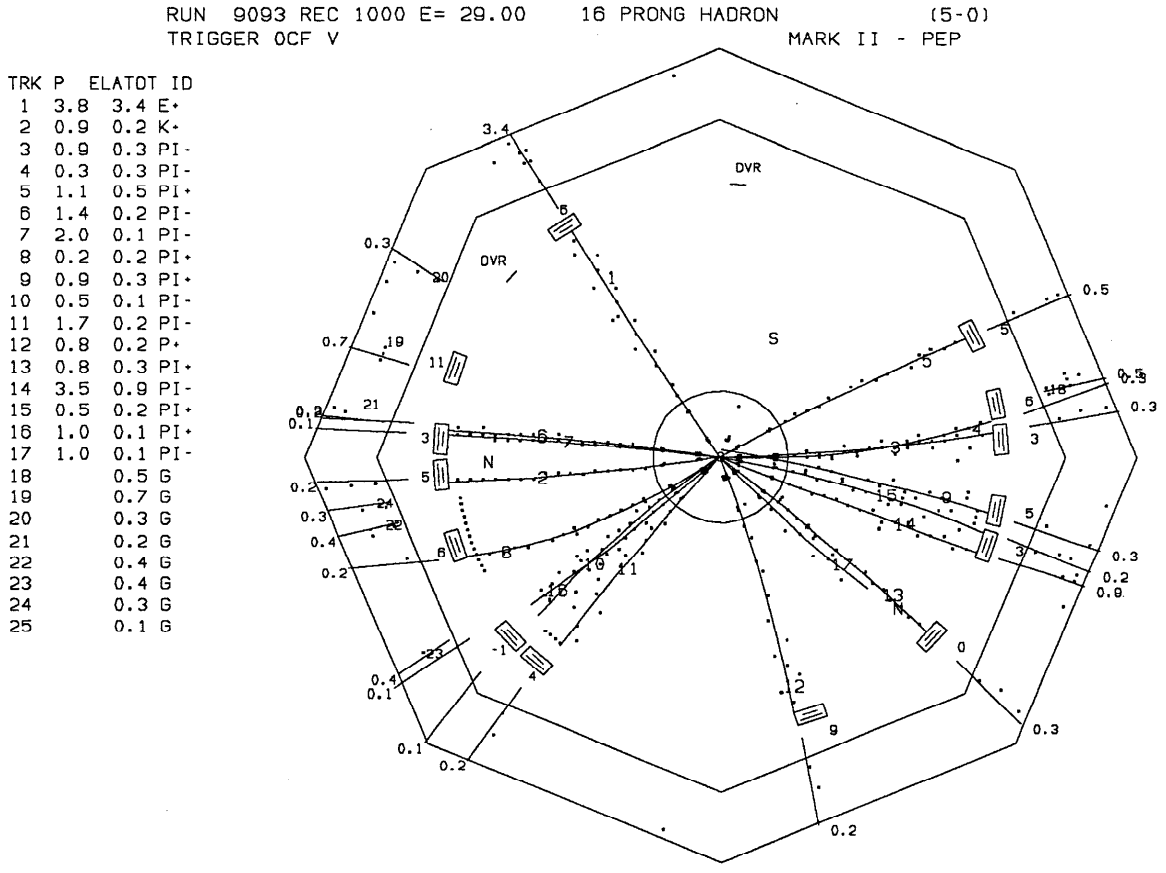

Figure 1.1: Example of a high transverse momentum lepton event. This figure is a computer reconstruction an event in the Mark II detector at the PEP storage ring. The e^+e^- collision occurred in the center of the figure; the lines drawn indicate the trajectories of charged particles produced from the collision through a cylindrical drift chamber of 1.5 m radius. The lepton is track 1; it is a 3.8 GeV/c electron, identified by the large fraction of its energy deposited in one of the eight calorimeter modules surrounding the drift chamber.

1.1 The Standard Model

Elementary particle physics is the study of the basic constituents of matter and of the interactions between these constituents. At the present time, it is believed that all matter is made up of the quarks and leptons listed in Table 1.1. The particles that are shown in this table are called fermions because they have half integer spin. The fermions in each successive column or generation are more massive than those in the preceding one. Ordinary matter is made up of the constituents of the first generation, but there exist two additional generations of fermions apparently just as fundamental. In this thesis, the u, d, and s quarks are often referred to as the

Table 1.1: The elementary fermions. The six quarks are named up, down, charm, strange, top, and bottom. There are three charged leptons (electron, muon, and tau) and three neutral leptons (the electron, muon, and tau neutrinos). The top quark and the tau neutrino have yet to be observed experimentally, although there are good theoretical reasons for their existence. For each particle given in this table there is an associated anti-particle.

Quarks

charge			
$\begin{pmatrix} +\frac{2}{3} \\ -\frac{1}{3} \end{pmatrix}$	$\begin{pmatrix} u \\ d \end{pmatrix}$	$\begin{pmatrix} c \\ s \end{pmatrix}$	$\begin{pmatrix} t \\ b \end{pmatrix}$

Leptons

charge			
$\begin{pmatrix} 0 \\ -1 \end{pmatrix}$	$\begin{pmatrix} \nu_e \\ e \end{pmatrix}$	$\begin{pmatrix} \nu_\mu \\ \mu \end{pmatrix}$	$\begin{pmatrix} \nu_\tau \\ \tau \end{pmatrix}$

"light" quarks, while the c and b quarks are referred to as "heavy" quarks.

There is good evidence for the existence of quarks [1-3]. In the same way as the atomic model explains the Periodic Table of elements, the quark model is able to explain and predict a large number of subatomic particles. Although the quarks are fractionally charged, they apparently combine in such a way so as to only produce stable particles with integer charge. These composite particles, called hadrons, are composed of quark anti-quark combinations (mesons) or three quark combinations (baryons). The proton, for example, consists of a uud combination of quarks. The heaviest quark discovered so far is the $-\frac{1}{3}$ charged bottom (b) quark, which has a mass approximately five times that of a proton. In this thesis we consider the production and decay of hadrons composed of b quarks and lighter quarks (u and d). There is currently no complete understanding of why free quarks are not found in nature. There is also no satisfactory explanation for the replication of the fermions into three generations. We do not know whether additional generations exist.

We now turn our attention to the forces between the particles. There are four known fundamental forces; three of these are listed in Table 1.2, along with the spin one particles (bosons) that mediate them. Gravity is the only interaction not

Table 1.2: The fundamental interactions. This table lists the fundamental interactions of relevence to this thesis and the particles that mediate them.

Interaction	Particle	Range (cm)
Electromagnetic	γ	∞
Weak	W^+, W^-, Z^0	10^{-16}
Strong	g	10^{-13}

listed; for the work presented here its effects are negligible.

All charged particles interact via the electromagnetic force, transmitted by the massless photon (γ). The weak interaction is mediated by the heavy intermediate vector bosons (W^+,W^-,Z^0). This force affects all particles, but over a limited range. The strong interaction is the force between quarks which holds hadrons together; it is mediated by gluons and acts over a greater range than the weak force.

An important goal in particle physics is to reduce the number of forces by unifying two or more of them. In doing so, it is hoped that a deeper understanding of the forces will emerge from the overall framework. For example, Maxwell unified the forces of electricity and magnetism. The important principle underlying the unified electromagnetic theory is the Lorentz invariance of space-time. The theory predicted and explained the existence of electromagnetic waves. The extension of Maxwell's theory to incorporate quantum mechanics and relativity lead to the theory of Quantum Electrodynamics (QED). This theory accounts for all electromagnetic phenomena, and has been tested by experiments to enormous accuracy.

Over the last twenty years, similar success has been achieved with the unification of the electromagnetic and weak forces into a single electro-weak interaction [4]. The mathematical structure of this theory rests upon an underlying symmetry called local gauge invariance. For that reason, it is often called a gauge theory and the particles in Table 1.2 are referred to as gauge bosons. The electro-weak theory predicted the existence of the W and Z^0 gauge bosons eventually discovered at CERN in 1983 [5]. The W bosons are the particles that mediate

quark decay.

Similarly, the concept of local gauge invariance has been applied to the force between quarks, the strong interaction. This application has yielded the gauge theory of Quantum Chromodynamics (QCD) based on the symmetry properties of a quantity known as color. The color force is mediated by gluons, whose existence is supported by the observation of three jet events in e^+e^- annihilation [6].

The Standard Model of particle physics incorporates the electro-weak theory, QCD, and the particles listed in Table 1.1 and Table 1.2.* This model contains a number of parameters that are not fixed by the model but which must come from experiments.† We will see later that, by using the results presented in this thesis, we can put constraints on two of these parameters.

1.2 B Hadron Production

1.2.1 Quark production in e^+e^- annihilations

Quark pair production from e^+e^- annihilation proceeds via the diagram shown in Figure 1.2. At center of mass energies of 29 GeV, all the quarks listed in Table 1.1 can be produced except the top quark, which is apparently too massive.

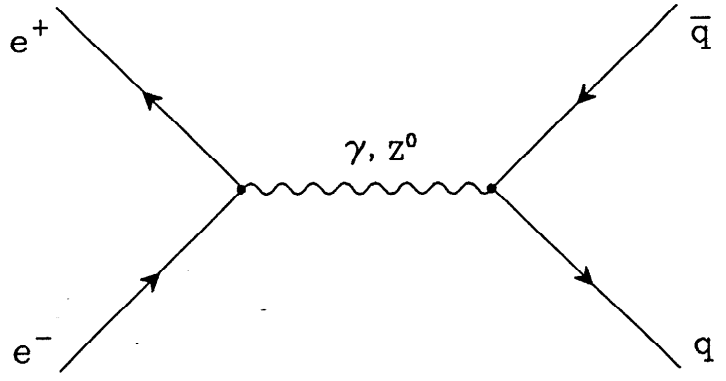

Figure 1.2: Quark pair production in e^+e^- annihilation. In this figure, quark production is shown mediated by both the electromagnetic (photon) and weak (Z^0) propagators, although the weak contribution is relatively small (~1 %).

* There is one additional particle needed to complete the Standard Model. This particle, known as the Higgs boson, is incorporated into a mechanism that breaks the electro-weak symmetry and provides mass to the W^+, W^-, and Z^0 bosons.

† The minimal number of parameters in the Standard Model is 19 [7]. For an excellent review of the Standard Model, see Ref. 8.

The cross section for fermion pair production from single-photon annihilation can be calculated from QED:

$$\sigma(e^+e^- \to f^+f^-) = C\frac{4\pi\alpha^2 q^2}{3E_{\rm cm}^2} \quad , \tag{1.1}$$

where α is the QED coupling constant ($\sim 1/137$), $E_{\rm cm}$ is the center of mass energy, and q is the fermion charge. C is a color factor, which for the production of lepton pairs (e.g. $\mu^+\mu^-$) is equal to 1, while for the production of quark pairs (e.g. $b\bar{b}$) is equal to 3. In Eqn. 1.1, phase space effects, QED loop corrections, and QCD corrections to the cross section are ignored.

From Eqn. 1.1, we see that quarks are produced in e^+e^- annihilation in proportion to their charge squared. Therefore, c quark production should comprise 4/11 and b quark production 1/11 of the total quark production. The produced quarks do not appear as free particles in the final state; they combine with other quarks in a process called fragmentation. The principal hadrons containing heavy quarks are given in Table 1.3 . The relative production of these various hadrons is discussed in Chapter 3.

1.2.2 Quark fragmentation

The fragmentation process describes the transformation of quarks into observable final state hadrons. This process cannot be calculated by perturbative QCD and is only phenomenologically understood. This phenomenology is illustrated in Figure 1.3. A bare outgoing quark is turned into a hadron by the production of a $q\bar{q}$ pair and the subsequent "dressing" of the bare quark by the anti-quark half of the pair. The quark half of the $q\bar{q}$ pair is free to carry on the fragmentation process. This process continues until there is insufficient energy to produce new $q\bar{q}$ pairs.

It is customary to parameterize fragmentation by a probability function (or fragmentation function), $f(z)$, where z is defined as the fraction of energy and momentum parallel to the quark direction carried away by the hadron:

$$z \equiv \frac{(E+P_{\|})_{\rm hadron}}{(E+P_{\|})_{\rm quark}} \quad . \tag{1.2}$$

Note that in this definition, the energy and momentum used in the denominator are not equal to the beam energy because of gluon and initial state radiation.

Table 1.3: Hadrons containing charm and bottom quarks. In this table, the principal charm and bottom hadrons are listed, along with their quark compositions and masses. For each hadron there exists an anti-particle with the opposite quark content. The mass values are taken from a compilation done by the Particle Data Group [9]. Particles without mass values have not been unambiguously observed. The D^{*0} and D^{*+} are higher angular momentum states of the D^0 and D^+.

Charm Hadrons		
Hadron Symbol	Quark Content	Mass (GeV/c^2)
D^0	$c\bar{u}$	1.865
D^+	$c\bar{d}$	1.869
D_s^+	$c\bar{s}$	1.971
D^{*0}	$c\bar{u}$	2.010
D^{*+}	$c\bar{d}$	2.010
Λ_c^+	cud	2.281
Bottom Hadrons		
Hadron Symbol	Quark Content	Mass (GeV/c^2)
B^0	$\bar{b}d$	5.275
B^+	$\bar{b}u$	5.271
B_s^0	$\bar{b}s$	-
Λ_b^0	bud	-

The most commonly used parameterization of the fragmentation function for heavy quarks is:

$$f(z) = \frac{1}{z \cdot \left(1 - \frac{1}{z} - \frac{\epsilon}{1-z}\right)^2} \quad , \tag{1.3}$$

a form that was suggested by Peterson *et al.* [10]. Other parameterizations have been suggested [11]. In Eqn. 1.3, ϵ is a parameter that is different for each quark flavor. Kinematical arguments suggest that the fragmentation functions for heavy quarks (charm and bottom) peak at higher values of z than those for lighter quarks [12].

One way to study the fragmentation functions for heavy quarks is through the use of the inclusive lepton spectra. Leptons produced at moderate to high momenta ($p > 2$ GeV/c) are used to tag the semi-leptonic decays of charm and

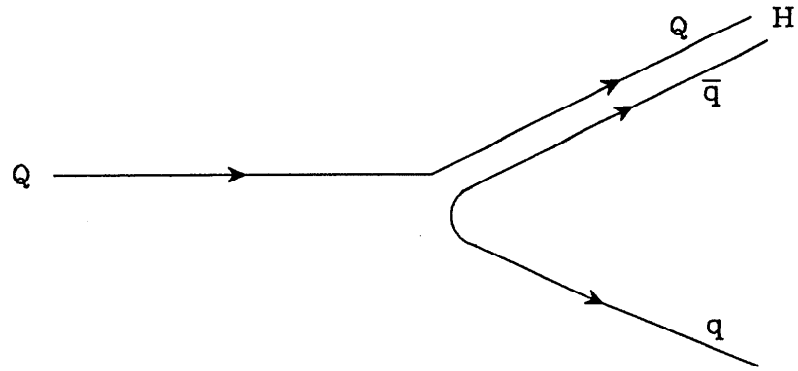

Figure 1.3: Quark fragmentation. This figure represents the phenomological picture of quark fragmentation as incorporated into the Monte Carlo. The quark Q is fragmented into the hadron H by the production of a $q\bar{q}$ pair. The use of the Monte Carlo is discussed in Chapter 3.

bottom hadrons. The measured momentum spectrum of the leptons can be used to infer the average hadron energy, and thus the mean z (written here as $< z >$) of the fragmentation function. In addition, since bottom and charm semi-leptonic decays can be partially separated on the basis of the lepton transverse momentum, one can measure $< z >$ for bottom and charm separately. This technique is used in this thesis to determine $< z >$ for the bottom fragmentation function.

Inclusive leptons have been used to measure $< z_c >$ and $< z_b >$ by a number of groups at the PEP and PETRA accelerators. These results are summarized in review articles by Bethke [13] and in a recent measurement by the JADE group [14]. The results from different experiments are in good agreement with one another, giving an $< z_c > = 0.63 \pm 0.04$ and an $< z_b > = 0.80 \pm 0.05$. In addition, the inclusive lepton analyses determine the semi-leptonic charm and bottom branching ratios.

The determination of the heavy quark fragmentation functions by the means of the inclusive lepton spectra has a number of systematic problems. Since C and B hadrons are not fully reconstructed, the determination of their fragmentation functions is somewhat subject to assumptions made on the momentum distribution and multiplicity of the remaining particles from their decay. In addition, the lepton signal does not completely separate charm and bottom decays and there is a significant background to the signal from mis-identified hadrons and non-prompt leptons.

In principle, it is preferable to reconstruct exclusive hadron decays. This technique has been used to determine the charm fragmentation function by the reconstruction of D^* mesons. The quantities that have been measured by this method are:

$$x_E \equiv \frac{E_{\rm hadron}}{E_{\rm beam}} \quad \text{or} \quad x_p \equiv \frac{P_{\rm hadron}}{\sqrt{E^2_{\rm beam} - m^2_{\rm hadron}}} \; . \tag{1.4}$$

Numerous measurements of these quantities for D^* production have been made at PEP and PETRA, as well as at the $\Upsilon(4S)$ resonance. These measurements are consistent with one another and are summarized in Ref. 13.

The quantities $x_{\rm E}$ and x_p defined above are more directly accessible than z defined in Eqn. 1.2. Unfortunately, these quantities are not themselves a measure of the fraction of energy carried away in the fragmentation process. Gluon radiation and initial state photon radiation precede the fragmentation process, reducing the quark energy. Therefore, x_E and x_p differ from z ($x < z$). This difference can be quite substantial, as discussed in Ref. 13. In order to compare the results from the exclusive charm decays with those from the inclusive lepton analyses, it is necessary to "translate" the x results into equivalent z results. In doing so, it is necessary to account for subtle differences in the definition of $< z >$ for various Monte Carlo programs. This translation has been done by Bethke and a value of $< z_c > \; = 0.704 \pm 0.010$ has been determined. Combining these results with additional contributions from other charmed hadrons ($D^0, D^+, D_s^+, \Lambda_c^+$, etc.), gives an overall $< z_c >$ from the exclusive measurements of approximately 0.68 ± 0.03. This value is in rough agreement with the average value from the inclusive lepton analyses.

In this thesis, the average B hadron lifetime is determined from the impact parameter distribution of leptons from B decay. We will see later that this impact parameter distribution depends on the average B energy ($< z_b >$). To address this problem, we will make a measurement of $< z_b >$ in order to "calibrate" the Monte Carlo. The value of $< z_b >$ is determined by comparing the lepton (p, p_t) distributions found in the data to similar distributions from $b\bar{b}$ Monte Carlo. The Monte Carlo distributions are generated at various values of $< z_b >$ using the Peterson parameterization (Eqn. 1.3).

Because C hadrons are more relativistic than B hadrons, the impact parameter distribution for leptons from charm decay is significantly less sensitive to fragmentation than that for bottom. For this reason, we choose not to measure $< z_c >$, and instead assume a world average value of 0.68.

1.3 B Hadron Decay

The simplest model for heavy hadron decay is called the spectator model. In this model, the bottom quark decays via the weak charged current mediated by the W boson, as shown in Figure 1.4.*

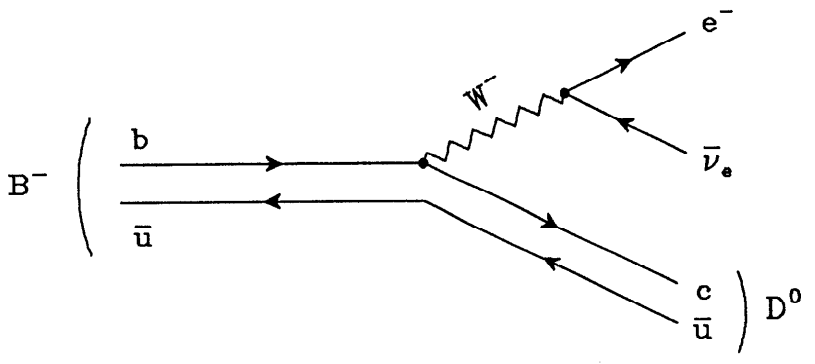

Figure 1.4: Spectator model decay. In this figure the process $B^- \rightarrow D^0 e^- \bar{\nu}_e$ is shown mediated by the weak charged current within the spectator model.

The light quark (the $\bar{u}$ in Figure 1.4) merely acts as a spectator to the weak decay process. The heavy quark is considered to be a free particle and its decay properties determine those of the hadron. In the context of this model, the B hadron lifetime τ_b is simply the reciprocal of the b quark decay width Γ_b.† With this relation in mind, we now summarize the relevant details of quark decay and then proceed to calculate the decay rate for b quarks.

1.3.1 Quark decay and the Kobayashi-Maskawa matrix

The weak charged current which mediates the decay process of Figure 1.4 can

* The neutral current associated with the Z^0 does not contribute to quark decays; there are strong experimental limits on such neutral current transitions. (e.g. $K_L^0 \rightarrow \mu^+\mu^-$).

† As a convention, we use lower case b to refer to bottom quarks and capital B to refer to bottom hadrons.

be written for quarks and leptons as:

$$\begin{aligned} J_{-}^{\mu} &= \frac{g_2}{2\sqrt{2}} \left(\bar{u} \;\; \bar{c} \;\; \bar{t} \right) \gamma^{\mu} (1-\gamma_5) \begin{pmatrix} d' \\ s' \\ b' \end{pmatrix} \\ &+ \frac{g_2}{2\sqrt{2}} \left(\bar{\nu}_e \, \bar{\nu}_{\mu} \, \bar{\nu}_{\tau} \right) \gamma^{\mu} (1-\gamma_5) \begin{pmatrix} e^- \\ \mu^- \\ \tau^- \end{pmatrix} \quad , \end{aligned} \tag{1.5}$$

where the row vectors are the eigenstates corresponding to the charge $+\frac{2}{3}$ quarks and the neutrinos. The column vectors are the eigenstates corresponding to the charge $-\frac{1}{3}$ quarks and the charged leptons. The weak coupling constant $g_2 = 2\sqrt[4]{2}\sqrt{G_F}\, m_W$. An analogous expression to Eqn. 1.5 can be written for the charged current associated with the W^+.

The weak eigenstates corresponding to the charge $-\frac{1}{3}$ quarks are written in primed notation in Eqn. 1.5 to indicate that they are not the same as the mass eigenstates for these quarks. In other words, there is quark mixing between generations. † This mixing can be expressed in matrix form as:

$$\begin{pmatrix} d' \\ s' \\ b' \end{pmatrix} = \begin{pmatrix} V_{ud} & V_{us} & V_{ub} \\ V_{cd} & V_{cs} & V_{cb} \\ V_{td} & V_{ts} & V_{tb} \end{pmatrix} \begin{pmatrix} d \\ s \\ b \end{pmatrix} \quad . \tag{1.6}$$

The matrix V is called the Kobayashi-Maskawa (KM) matrix [15]. It is the three dimensional analogue of the Cabibbo matrix that describes mixing in the four quark model [16].

The elements of the KM matrix are complex; therefore a total of eighteen numbers are needed to describe all the terms of the matrix. By imposing the constraint of unitarity, and by redefining the quarks fields to remove unphysical phases, the number of parameters can be reduced from eighteen to four. These four parameters can be chosen as three angles (θ_{12}, θ_{13}, θ_{23}) and one phase (δ). A number of different parameterizations of the KM matrix exist [15, 17]. The differences in these parameterizations do not represent fundamental physical

† It is merely convention to have the charge $-\frac{1}{3}$ quarks mixed while leaving the charge $+\frac{2}{3}$ quarks unmixed.

differences, so a particular choice is mostly a matter of convenience. We adopt the parameterization first introduced by Chau and Keung and later extended to any number of dimensions by Harari and Leurer [17]. In this form, the KM matrix can be written as the product of three separate matrices, each one analogous to a rotation between two generations:

$$V = \Omega_{23}\,\Omega_{13}\,\Omega_{12} \quad ,$$

$$V = \begin{pmatrix} 1 & 0 & 0 \\ 0 & c_{23} & s_{23} \\ 0 & -s_{23} & c_{23} \end{pmatrix} \begin{pmatrix} c_{13} & 0 & s_{13}e^{-i\delta} \\ 0 & 1 & 0 \\ -s_{13}e^{i\delta} & 0 & c_{13} \end{pmatrix} \begin{pmatrix} c_{12} & s_{12} & 0 \\ -s_{12} & c_{12} & 0 \\ 0 & 0 & 1 \end{pmatrix} \quad , \qquad (1.7)$$

where $c_{ij} \equiv \cos\theta_{ij}$ and $s_{ij} \equiv \sin\theta_{ij}$. The middle matrix in Eqn. 1.7 has the additional term in δ because it describes a rotation between fermions two generations apart. Multiplying these matrices, we obtain:

$$V = \begin{pmatrix} c_{12}c_{13} & s_{12}c_{13} & s_{13}e^{-i\delta} \\ -s_{12}c_{23}-c_{12}s_{23}s_{13}e^{i\delta} & c_{12}c_{23}-s_{12}s_{23}s_{13}e^{i\delta} & s_{23}c_{13} \\ s_{12}s_{23}-c_{12}c_{23}s_{13}e^{i\delta} & -c_{12}s_{23}-s_{12}c_{23}s_{13}e^{i\delta} & c_{23}c_{13} \end{pmatrix} \quad . \qquad (1.8)$$

This parameterization has the advantage that the elements above the diagonal are simple. Using a number of experimental results, Eqn. 1.8 will be simplified later in this chapter.

1.3.2 Heavy quark decay

The first calculations for heavy quark decay were made in the charm sector [18]. These calculations were initially done within the spectator model. From the semi-electronic branching ratios of the D^0 and D^+ mesons [19], it was soon realized that the spectator model is not sufficient to explain charm hadron decay. Current measurements of these branching ratios give:

$$\begin{aligned} \mathrm{BR}\,(D^0 \to e^+\nu_e X) &= 7.0 \pm 1.1\,\% \\ \mathrm{BR}\,(D^+ \to e^+\nu_e X) &= 18.2 \pm 1.7\,\% \quad , \end{aligned} \qquad (1.9)$$

where X represents one or more hadrons [9]. In the spectator model, these two branching ratios should be equal; the only difference between the D^0 and D^+ lies

in their respective spectator quarks. There has been considerable effort made to understand charm hadrons by including non-spectator diagrams (such as the annihilation, exchange and Penguin diagrams) [20], and by the development of models for exclusive charm decay [21]. Although the subject of charm decays is a fascinating one, our main concern is with the decays of bottom hadrons.

1.3.3 *Bottom quark decay*

In the absence of generation mixing (i.e. V diagonal), quarks would couple only to their doublet partners. This situation would result in a stable b quark since it is lighter than its top quark partner. In the KM scheme, the bottom quark can decay into the lighter u and c quarks, with amplitudes proportional to the terms V_{ub} and V_{cb} respectively. These b quark decays are illustrated in Figure 1.5.

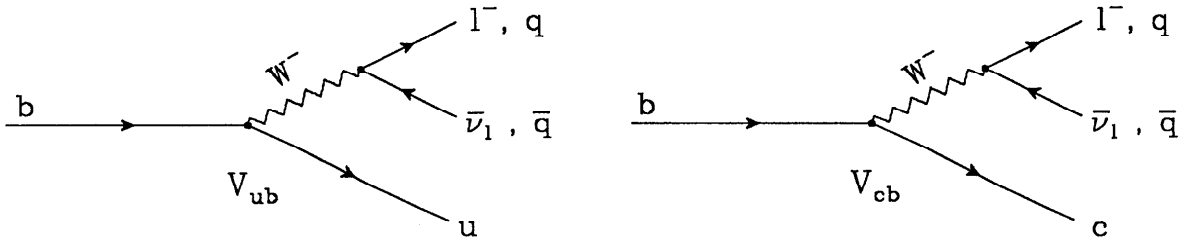

Figure 1.5: Contributions to b quark decay. The amplitude for each diagram is proportional to the KM matrix terms V_{ub} and V_{cb} respectively. The $q\bar{q}$ pair produced can be any of the quark combinations present in the KM matrix.

The total b quark decay rate can then be written as the sum of contributions from $(b \to u)$ and $(b \to c)$ transitions:

$$\Gamma_{tot} = \sum_{q=u,c} \Gamma(b \to q) \ . \tag{1.10}$$

The decay rate for each particular quark transition $(b \to q)$ can be broken up into semi-leptonic and hadronic parts:

$$\Gamma(b \to q) = \Gamma_{sl}(b \to q) + \Gamma_{had}(b \to q) \ . \tag{1.11}$$

Let us first consider $\Gamma_{sl}(b \to q)$. The matrix element for this process can be written:

$$M_{sl}(b \to q) \;=\; -\frac{G_F}{\sqrt{2}} V_{qb}\, \bar{q}\, \gamma_\mu\, (1-\gamma_5)\, b\, \bar{l}\, \gamma_\mu\, (1-\gamma_5)\, \nu_e \quad . \tag{1.12}$$

This matrix element is similar to that for muon decay; therefore after squaring it and integrating over phase space we obtain:

$$\Gamma_{sl}(b \to q) \;=\; \frac{G_F^2\, m_b^5}{192\, \pi^3}\, |V_{qb}|^2\, I(\epsilon) \quad . \tag{1.13}$$

The first factor in Eqn. 1.13 corresponds to the muon decay rate with the b quark mass substituted for the muon mass. The second factor is the appropriate KM matrix element and the last one is the phase space factor:

$$I(\epsilon) \;=\; 1 - 8\epsilon^2 + \epsilon^6 - \epsilon^8 - 24\, \epsilon^4 \ln \epsilon \quad , \tag{1.14}$$

for $\epsilon \equiv m_q/m_b$. The factor $I(\epsilon)$ is close to unity for muon decay and $(b \to u)$ transitions, but is approximately 0.5 for $(b \to c)$ transitions ($\epsilon \sim 0.3$).

Returning to Eqn. 1.11, we note that the hadronic part for $(b \to q)$ transitions is simply 3 times Γ_{sl} given in Eqn. 1.13. The factor of 3 comes about because of color. Therefore, considering the possible lepton and quark combinations* from the W decay, and neglecting phase space effects, the decay rates for the $(b \to q)$ transition are in the ratio:

$$e\nu_e : \mu\nu_\mu : \tau\nu_\tau : \bar{u}d : \bar{c}s \;=\; 1:1:1:3:3 \quad . \tag{1.15}$$

This simple picture of b quark decay predicts a semi-leptonic branching ratio of $\frac{1}{9}$ ($\sim 11\,\%$) for each lepton type.

1.3.4 Improvements to the spectator decay model

To improve the calculation of the b quark decay rate, we now consider the

---

* Although all quark combinations connected by an element of the KM matrix are possible, those combinations connected by a diagonal element (Cabibbo-favored) have much larger decay rates than the off-diagonal combinations (Cabibbo-supressed).

following refinements to the spectator model:

- First order gluon radiation.
- Short distance QCD effects.
- Mass effects from the final state particles.

The first refinement includes gluon radiation effects that are soft in comparison with the b quark mass. These effects lower the predicted decay rate for both the hadronic and semi-leptonic modes. The second category contains gluon effects that are hard in comparison with the b quark mass, but are soft in comparison with the W (e.g. gluon exchange). These effects substantially increase the hadronic decay rate but leave the semi-leptonic rate untouched. The third refinement lowers the predicted decay rate for both the hadronic and semi-leptonic modes.

Gluon radiation:

Two diagrams contributing to first order gluon radiation are illustrated in Figure 1.6. These diagrams were originally studied in the context of charm decay [22]. In these studies, it was observed that the QCD corrections for heavy quark decay can be easily related to the QED corrections for muon decay [23]. In this comparison, the following substitution is made:

$$\alpha \rightarrow \frac{4}{3}\alpha_s \quad . \tag{1.16}$$

The quantity α_s is given by:

$$\alpha_s = \frac{12\,\pi}{(33-2n_f)\ln(m_b^2/\Lambda^2)} \quad , \tag{1.17}$$

where n_f is the number of effective quark flavors, m_b is the mass of the bottom quark, and Λ is the QCD renormalization point. For typical values of the parameters ($n_f = 4$, $m_b = 4.8$ GeV/c^2, and $\Lambda = 0.2$ GeV/c^2), one gets a value $\alpha_s = 0.24$.

Using the results given in Ref. 23, the corrections to the b quark semi-leptonic rate due to first order gluon radiation have been calculated [24]. These corrections modify Eqn. 1.13 to become:

$$\Gamma_{sl}(b\rightarrow q) = \frac{G_F^2\, m_b^5}{192\,\pi^3}\,|V_{qb}|^2\, I(\epsilon)\left(1-\frac{2}{3\pi}\alpha_s g(\epsilon)\right) \quad , \tag{1.18}$$

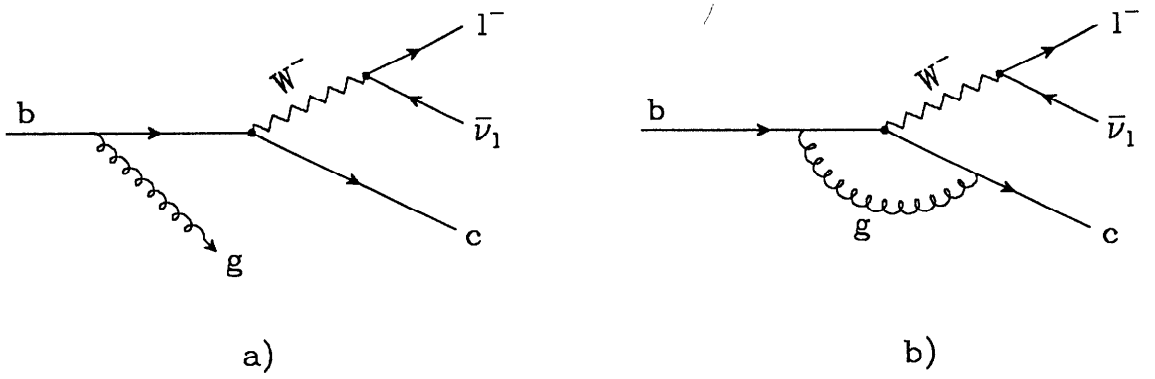

Figure 1.6: First order gluon radiation. These diagrams illustrate real (a) and virtual (b) gluon bremsstrahlung. In a) the radiated gluon can be emitted from the final quark leg as well. In b) The gluon can be emitted and reabsorbed entirely on either the initial and final quark legs as well.

for $\epsilon \equiv m_q/m_b$. The function $g(\epsilon)$ is tabulated in the paper by Cabibbo and Maiani in Ref. 22. With $m_b = 4.8$ GeV/c^2, $m_c = 1.5$ GeV/c^2, and $m_u = 0.15$ GeV/c^2, one obtains values of $I(\epsilon) = 0.99$ and $g(\epsilon) = 3.5$ for $(b \to u)$ transitions and $I(\epsilon) = 0.49$ and $g(\epsilon) = 2.5$ for $(b \to c)$ transitions. Using Eqn. 1.18, the numerical estimate for the total semi-leptonic rate in the spectator model becomes:

$$\Gamma(b \to X l\nu) \;=\; 2.53 \times 10^{-11} \left[1.90\,|V_{ub}|^2 \,+\, |V_{cb}|^2 \right] \;(\mathrm{GeV}) \;, \qquad (1.19)$$

where X represents any hadronic final state.

Short distance QCD effects:

Short distance effects, such as hard gluon exchange, do not affect the semi-leptonic decay rate. In hadronic decays, however, they effectively renormalize the weak current from a momentum scale corresponding to M_W to a scale characteristic of quark masses. This renormalization enhances the hadronic decay channels; the color factor of 3 is replaced by the expression:

$$3 \;\to\; 2\,C_+^2 \,+\, C_-^2 \;, \qquad (1.20)$$

where C_+ (C_-) is the coefficient of the term in the Hamiltonian with the addition(subtraction) of the contribution from quark interchange [25]. A recent

estimate [26] gives $C_+ \sim 0.8$ and $C_- \sim 1.5$. This leads to an 18 % enhancement in the hadronic decay rate.

Mass effects:

Until now we have considered the quarks and leptons produced at the W decay vertex to be massless. That assumption is reasonable in the case of $(e\nu_e)$,$(\mu\nu_\mu)$, and $(\bar{u}d)$ final states. The production of (τ, ν_τ) and $(\bar{c}s)$ states will be suppressed due to phase space. These effects have been calculated [27]; combining them with the short distance QCD effects, the relative decay ratios of Eqn. 1.15 become:

$$e\nu_e : \mu\nu_\mu : \tau\nu_\tau : \bar{u}d : \bar{c}s \;=\; 1.0 : 1.0 : 0.2 : 3.5 : 0.8 \;. \tag{1.21}$$

With these corrections we now expect a semi-leptonic (electron and muon) branching ratio of approximately 15 %. The current world average is 12.1 ± 0.8 % [14]. The fact that the measured value of the semi-leptonic branching ratio is lower that the theoretical estimate is seen as evidence for further enhancement of the hadronic decay rate. In any case, from the experience with charm decays, it is believed that non-spectator effects in semi-leptonic decays are considerably smaller than those in hadronic decays. Therefore, the total b quark decay rate can be determined most accurately from the expression:

$$\Gamma_{tot} \;=\; \frac{\Gamma(b \to Xl\nu)}{\mathrm{BR}(b \to Xl\nu)} \;, \tag{1.22}$$

where we use the calculated semi-leptonic decay rate (Eqn. 1.18) and the *measured* value of the semi-leptonic branching ratio.

1.3.5 *Beyond the spectator decay model*

Even though we believe the estimate of the semi-leptonic decay rate from the spectator model to be reliable, there is still a strong dependence in Eqn. 1.18 on m_b. This "bare quark" mass is uncertain to the level of 200-300 MeV/c^2 , leading to a sizable uncertainty in the calculation of Γ.

One way to reduce this uncertainty is to use the well measured B meson mass to help determine m_b. The bare quark mass can be related to the mass of the B meson by examining the B lepton spectrum in the context of the spectator decay model

[28]. In this comparison the effects of soft gluon radiation, the mass of the spectator quark, and Fermi motion within the meson have been taken into account. The result of such a comparison with the CLEO data yields a value $m_b = 4.95 \pm 0.04$ GeV/c^2 [29]. Using this mass in Eqn. 1.18 gives a value for the semi-leptonic decay rate:

$$\boxed{\Gamma(b \to X l \nu) \;=\; 2.80 \times 10^{-11} \left[2.01 \, |V_{ub}|^2 \;+\; |V_{cb}|^2 \right] \; (\mathrm{GeV}) \; .} \qquad (1.23)$$

A second, and perhaps more rigorous, approach in reducing the error in Γ from m_b uncertainty is to consider B hadron decays rather than free quark decays. In this approach, it is necessary to calculate matrix elements between exclusive hadron states, and then sum the exclusive contributions to get the total decay rate. Two different models to base such calculations on have been proposed [30,31]. These models have been applied to semi-leptonic decays only.

In the model of Wirbel, Stech, and Bauer (WSB [30]), the hadron wave functions are taken to be the solutions of a relativistic harmonic oscillator potential. Matrix elements are calculated between these wave functions using the hadronic current for the $B \to D l\nu$, $D^* l\nu$, $\pi l\nu$, and $\rho l\nu$ channels. WSB find the maximum total rate for these four channels to be:

$$\Gamma(B \to X l \nu) \;=\; 2.18 \times 10^{-11} \left[1.65 \, |V_{ub}|^2 \;+\; |V_{cb}|^2 \right] \; (\mathrm{GeV}) \; . \qquad (1.24)$$

The $(b \to c)$ rate is close to the value predicted by the free quark model (Eqn. 1.19), but the $(b \to u)$ rate is considerably lower than in the free quark case because only a fraction of the exclusive $(b \to u)$ channels have been considered. Work is in progress to extend this calculation to more exclusive channels [32].

The constituent quark model is used in the work of Grinstein, Isgur, and Wise (GIW [31]). In this model, the hadron wavefunctions are taken to be non-relativistic solutions of a Coulomb plus linear potential:

$$V(r) \;=\; -\frac{4\alpha_s}{r} + c + br \; , \qquad (1.25)$$

with $\alpha_s = 0.5$, $c = -0.84\,\mathrm{GeV}$, and $b = 0.18\,\mathrm{GeV}^2$. The authors calculate the spectra for $(B \to X_u e\nu)$ and $(B \to X_c e\nu)$ transitions, where X_u and X_c

are mesons made from $u\bar{d}$ and $c\bar{d}$ combinations respectively. They find that the $(B \rightarrow X_c e\nu)$ transitions are effectively saturated by production of D and D^* mesons, in agreement with experimental observation. For the $(B \rightarrow X_u e\nu)$ transitions, the total rate is not saturated by the lowest lying states; therefore an uncertainty in the overall normalization of 20 % is assigned, and GIW suggest using the free quark model prediction for this rate.

The total semi-leptonic B decay rate predicted by the model of Grinstein, Isgur and Wise is:

$$\Gamma(B \rightarrow Xl\nu) \;=\; 3.81 \times 10^{-11} \left[2.04\,|V_{ub}|^2 \;+\; |V_{cb}|^2 \right] \;(\mathrm{GeV}) \;. \qquad (1.26)$$

This result is significantly different than that given in Eqn. 1.24. Recently, it has been suggested that the predictions of GIW differ from those of WSB because of incorrect assumptions made by GIW on the behavior of the hadron wave functions in the non-relativistic limit [33].

1.3.6 *Summary of B decay rate calculations*

The different approaches to calculating the B decay rate do not give identical answers, although this is partly due to different effective quark masses being assumed. Clearly, future work is needed to improve these calculations. For the time being, however, we simply make the arbitrary choice of the free quark calculation (Eqn. 1.23) with $m_b = 4.95\ \mathrm{GeV/c^2}$, to give us the relation between the decay rate and KM terms. This calculation lies somewhere between those from the models of WSB and GIW.

The B lifetime can then be related to the semi-leptonic decay rate by the following expression:

$$\tau_b \;=\; \frac{\hbar}{\Gamma_{tot}} \;=\; \frac{\hbar\,\mathrm{BR}(B \rightarrow Xl\nu)}{\Gamma(B \rightarrow Xl\nu)} \;. \qquad (1.27)$$

Using Eqn. 1.23 for the semi-leptonic rate, the lifetime prediction becomes:

$$\boxed{\tau_b \;=\; \frac{(2.35 \times 10^{-14})\ \mathrm{BR}(B \rightarrow Xl\nu)}{[\,2.01\,|V_{ub}|^2 \;+\; |V_{cb}|^2\,]} \;(\mathrm{sec}) \;.} \qquad (1.28)$$

The measured value of τ_b can be used to constrain the KM elements $|V_{ub}|$ and $|V_{cb}|$.

1.4 Testing the KM Model

The direct constraint on elements of the Kobayashi-Maskawa matrix from measurement of the B lifetime is shown in Eqn. 1.28. In general, however, the B lifetime is only one of a number of key measurements that can be used to test the KM model. The problems of accommodating these measurements within the framework of a unitary KM matrix is the subject of much study [34]. This subject is of great importance for a number of reasons. Failure of the KM matrix to obey unitarity might signal new physics or the presence of a fourth generation. In addition, it is hoped that quark mixing provides an explanation for CP violation within the standard model. Finally, careful study of the quark couplings might shed light on possible relations between the quark masses and the matrix elements, so as to reduce the number of free parameters in the model [35].

At this point, we simply enumerate some of the more important experimental constraints on the KM matrix elements. The present knowledge on the matrix elements connecting the first two generations is:

$$|V_{ud}| \sim 0.97\,,\ |V_{us}| \sim 0.22\,,\ |V_{cd}| \sim 0.24\,,\ |V_{cs}| > 0.66\ . \tag{1.29}$$

These results come from experiments on nuclear β decay, hyperon and K_{e3} decay, and neutrino charm production [36]. Eqn. 1.29 indicates that the off-diagonal elements of the KM matrix are significantly smaller than one.

Turning to the b quark sector, there is a limit on the ratio:

$$R \equiv \frac{|V_{ub}|}{|V_{cb}|} < 0.23\ . \tag{1.30}$$

This limit comes from examination of the endpoint lepton spectrum from B meson decay at the $\Upsilon(4S)$ resonance [37]. The shape of the endpoint region is sensitive to the relative contributions from $(b \to u)$ and $(b \to c)$ transitions and is somewhat model dependent.

In addition, the ARGUS group reports the preliminary observation of $(b \to u)$ transitions in the modes $(B \to p\bar{p}\pi, p\bar{p}\pi\pi)$ [37]. They translate the measured

branching ratios for these modes into a conservative lower limit:

$$\frac{|V_{ub}|}{|V_{cb}|} > 0.07 \ . \tag{1.31}$$

Since the decay rate is proportional to the KM matrix elements *squared*, it is clear from Eqn. 1.30 that b quarks almost always decay into c quarks. Therefore, the B lifetime puts strong constraints on $|V_{cb}|$ independent of the value of $|V_{ub}|$. Even for b quark couplings as large as the Cabibbo angle ($|V_{cb}| \sim 0.22$), $|V_{ub}|$ is smaller than a few percent. Therefore, to a good approximation:

$$s_{12} \sim \theta_{12} \sim \theta_c \ ; \ c_{13} \sim 1 \ , \tag{1.32}$$

where θ_c is the Cabibbo angle. By setting c_{13} to 1, the KM matrix in Eqn. 1.8 becomes:

$$V = \begin{pmatrix} c_{12} & s_{12} & s_{13}e^{-i\delta} \\ -s_{12}c_{23}-c_{12}s_{23}s_{13}e^{i\delta} & c_{12}c_{23}-s_{12}s_{23}s_{13}e^{i\delta} & s_{23} \\ s_{12}s_{23}-c_{12}c_{23}s_{13}e^{i\delta} & -c_{12}s_{23}-s_{12}c_{23}s_{13}e^{i\delta} & c_{23} \end{pmatrix} \ . \tag{1.33}$$

In this form, measurement of the B lifetime directly determines the value of s_{23}.

Now consider the t quark elements in the KM matrix (the bottom row). A number of quantities measurable by experiment have influence on the allowed range of the t quark couplings:

- The top quark mass m_t.
- CP violation in the K system.
- $B\bar{B}$ mixing.
- Rare K and B decays.

The top quark mass is bounded to lie within:

$$22 \text{ GeV/c}^2 < m_t < 180 \text{ GeV/c}^2 \ , \tag{1.34}$$

where the lower bound comes from the measurement of $\sigma(e^+e^- \rightarrow \text{Hadrons})$ at PETRA [9] and the upper bound comes from the constraint within the standard model from Δr assuming $\rho = 1$ [38].

The only place where CP violation has been conclusively observed is in the neutral kaon system. In particular, $K^0\bar{K}^0$ mixing is believed to account for all observed CP violation [39]. The box diagram for this process is shown in Figure 1.7. The parameter ϵ describes CP violation in the K mass matrix; it can be written as:

$$\epsilon \sim C_1 (B_K f_K^2) s_{12} s_{13} s_{23} s_\delta f_1(m_c^2, m_t^2) \ , \tag{1.35}$$

where C_1 is a constant of proportionality, B_K is a parameter resulting from the hadronic matrix element of the box diagram, f_K is the kaon decay constant, and f_1 is a function of the charm and top quark masses (mostly top) [40]. The value of ϵ is experimentally well determined [9], therefore Eqn. 1.35 puts constraints on the top quark mass and s_δ, after input from other sectors of the KM matrix (e.g. s_{23} via the B lifetime). There is, however, a great deal of theoretical uncertainty in the calculation of B_K [8]. This uncertainty dilutes the constraints imposed by Eqn. 1.35.

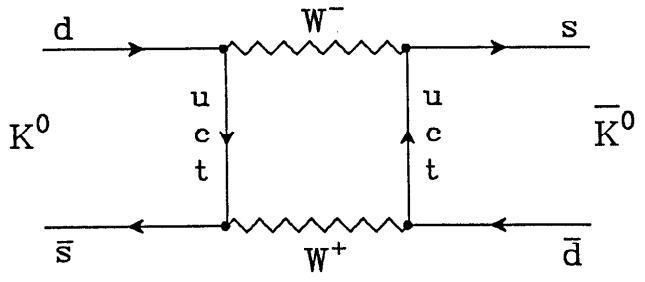

Figure 1.7: Box diagram for $K^0\bar{K}^0$ mixing.

In $K \to \pi\pi$ decays there may exist a small amount of CP violation present in the decay amplitude for the $I = 2$ transition. This CP violation is described by the parameter ϵ'. The ratio of ϵ'/ϵ is also proportional to $s_{12}s_{23}s_{13}s_\delta$ [40], and a non-zero value for this quantity may be able to confirm the KM model and to rule out other models of CP violation [39]. A number of experimental attempts are underway to measure this ratio [41].

$B\bar{B}$ mixing is mediated by a diagram similar to Figure 1.7 for the kaon system. Because of the large top quark mass, this mixing is largely determined by the diagram involving the top quark. For B_d mesons the amount of mixing depends on $|V_{td}|$, while for B_s mesons it depends on $|V_{ts}|$. A measure of the amount of mixing

is provided by the parameter x, defined as the ratio of the $B_L - B_S$ mass difference to the B decay rate. For $B_d\bar{B}_d$ mixing, this parameter can be expressed as:

$$x_d \equiv \frac{\Delta M}{\Gamma} \sim C_2\, \tau_b\, s_{23}^2\, (B_B f_B)\, |V_{td}|^2 f_2(m_t^2) \ , \tag{1.36}$$

where C_2 is a constant of proportionality, B_B and f_B are analogous to B_K and f_K in the kaon system, and f_2 is a function of the top quark mass [42]. Just as in the expression for ϵ, there is a strong dependence in Eqn. 1.36 on m_t.

Experimentally, mixing can be observed by looking at dilepton $B_d\bar{B}_d$ events. The strength of the mixing is measured by a parameter r_d, the ratio of like sign to unlike sign dilepton events. This parameter can be expressed in terms of x_d by the relation:

$$r_d = \frac{x_d^2}{x_d^2 + 2} = 0.22 \pm 0.09 \pm 0.04 \ . \tag{1.37}$$

The experimental value for r_d comes from a recent measurement by the ARGUS group [43]. Since $|V_{ts}|$ is expected to be much larger than $|V_{td}|$, Eqn. 1.37 implies that $r_s \sim 1$. The ARGUS results are consistent with a previous result from the UA1 group [44].

Limits on rare decay modes of K and B mesons also help to constrain the KM matrix [45]. In particular, the rate for the process $K^+ \to \pi^+ \nu\bar{\nu}$ puts similar constraints as ϵ'/ϵ on the KM model [46].

1.5 Analysis Objective

Before 1983, it was conventional to assume that $(b \to c)$ couplings were approximately of the same magnitude as the coupling between the first two generations ($|V_{bc}| \sim \theta_c$). These assumptions lead to a predicted B lifetime of ~ 0.07 ps, too short to be measured by existing experiments. Conventional wisdom proved wrong. In the summer of 1983, the MAC and Mark II groups reported the first B lifetime measurements [47,48]:

$$\begin{aligned} \tau_b &= 1.80 \pm 0.60 \pm 0.40\,\text{ps} \ \ (\text{MAC}) \ , \\ \tau_b &= 1.20\ ^{+0.45}_{-0.36} \pm 0.30\,\text{ps} \ \ (\text{Mark II}) \ , \end{aligned} \tag{1.38}$$

where the first error is statistical and the second systematic. These measured lifetimes were some twenty times longer than originally predicted, indicating that

the second and third generations are much more weakly coupled than are the first two. A number of other measurements have followed those listed in Eqn. 1.38 and are summarized in Chapter 10.

The primary objective of this thesis is to measure the B lifetime and significantly reduce the error on the measurement (both statistical and systematic). The first critical step in the lifetime measurement is the isolation of a sample of events that are enriched in B hadron production. This enrichment is most reliably done by selecting events containing a high transverse momentum lepton [49]. A B purity of approximately 65 % is obtained in this manner (an amount considerably better than 1/11, the fraction of produced $b\bar{b}$ pairs).

The second step in the analysis is to measure the displacement from the origin of tracks in these events coming from B hadrons. In principle, one would like to measure the B decay length. Unfortunately, full reconstruction of B hadrons is quite difficult. This difficulty arises partly because of the large number of tracks in a typical event and partly because of the neutral particles that are often produced in B decay and remain undetected. For this reason, in this thesis, only charged particles reliably known to have come from B hadron decay are used in the lifetime determination.

A schematic representation of a $B\bar{B}$ event is shown in Figure 1.8. In addition to the tracks from B decay, there are tracks from the primary (e^+e^-) interaction point and from secondary charm decays. Therefore the only track known with confidence to have originated from B hadron decay is the high p_t lepton. The distance of closest approach (impact parameter) of this lepton track measured relative to the B production point contains information about the parent lifetime.

The high p_t lepton is used to provide a measure of the B lifetime as well as to enrich the sample. Therefore we measure the B lifetime *averaged* over the various types of B hadrons produced and *weighted* by the relative semi-leptonic branching ratios for these hadrons.

For a B lifetime in the vicinity of 1 ps, the average lepton impact parameter is approximately 145 μm. As discussed in Chapter 2, the addition of a high precision inner drift chamber (the Vertex Chamber) greatly enhanced the ability of the Mark II detector to measure such short distances. Even so, with an experimental resolution that is only comparable to the lifetime effect, a large number of events

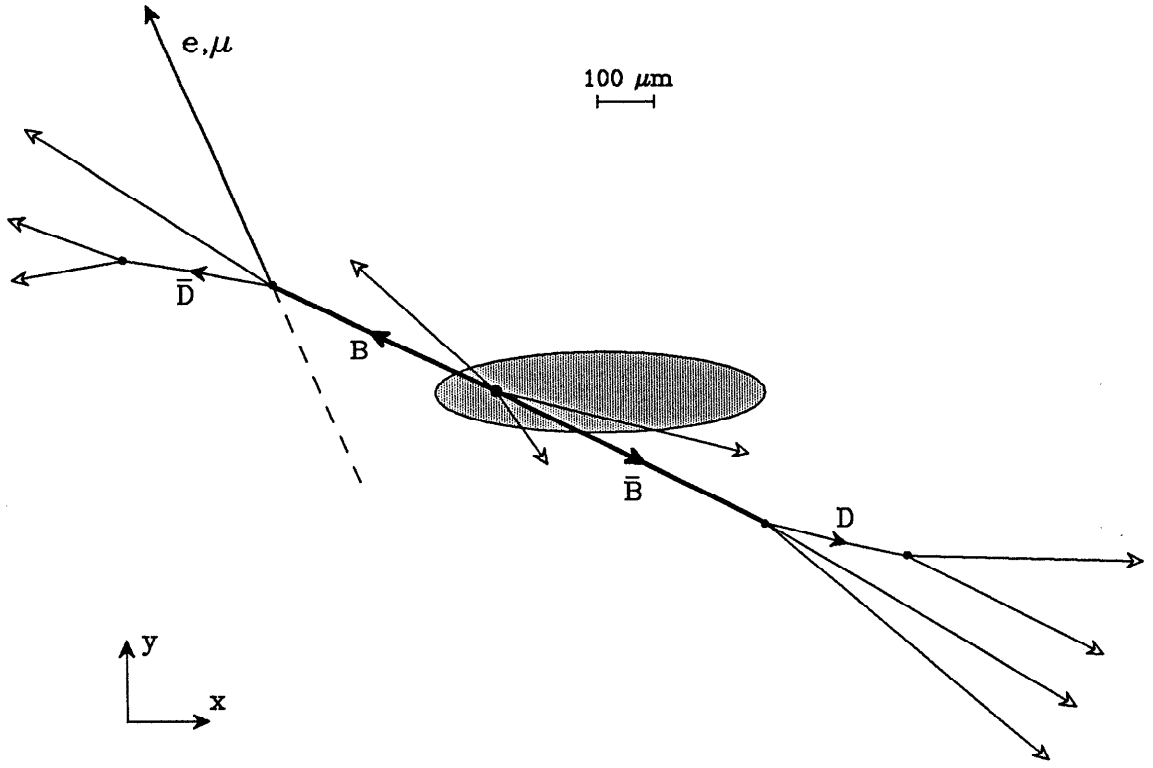

Figure 1.8: Schematic representation of a $B\bar{B}$ event. This figure shows a hypothetical event viewed near the center of the detector. The shaded ellipse represents the e^+e^- collision region. Each B hadron originates at the e^+e^- collision point and travels a distance proportional to its lifetime. It then decays to a charm (D) hadron. The reconstructed tracks can originate from the e^+e^- collision point, a B decay vertex, or a D decay vertex. There can be additional neutral particles not shown. In general, only the origin of the lepton (e,μ) track is known. The B lifetime is determined by measuring the distance of closest approach from the lepton track to the e^+e^- collision point.

are required to have a statistically significant result. In addition, a Monte Carlo simulation is needed to relate the average B lifetime to the measured impact parameter distribution.

In order to achieve the maximal statistical and systematic accuracy, the analysis presented in this thesis concentrates on the following issues:

- **Measuring the B enrichment.** The lifetime determined from the data clearly depends on the purity of the B event selection. There is significant systematic error associated with uncertainty in the "B fraction". In this

thesis, a separate analysis of inclusive leptons is done to measure this fraction in the data.

- **Determining the average B hadron energy.** The relationship between the impact parameter distribution and the corresponding lifetime depends on the average B hadron energy. In this analysis, we determine this average energy by measuring $<z>$ of the B fragmentation function.
- **Understanding the impact parameter resolution.** Improvements in the charged particle tracking can lead to a higher efficiency and resolution for the reconstruction of tracks. In addition, an understanding of the shape and tails of the resolution function (by measuring it in the data) is needed to have confidence in the lifetime fit and to reduce the systematic errors caused by resolution effects.

1.6 Thesis Outline

In Chapter 2, the experimental apparatus used to make the lifetime measurement is introduced. A discussion of the event reconstruction procedure and the Monte Carlo follows in Chapter 3, while Chapter 4 is devoted to a careful study of the Vertex Chamber resolution. The identification and analysis of inclusive leptons in hadronic events are outlined in Chapters 5 and 6. The use of the impact parameter technique and the resulting lifetime determination are presented in Chapter 7 and 8, respectively. Checks on the analysis procedure and the estimation of systematic errors are presented in Chapter 9. The final chapter contains a summary of the results, the theoretical implications, and a comparison with other experiments. The appendices document some of the analysis details.

Experimental Apparatus

2.1 The PEP Storage Ring

The data used in this thesis were taken with the Mark II detector at the PEP (Positron Electron Project) storage ring. PEP is a large positron-electron colliding beam facility with a circumference of 2.2 km, located at the Stanford Linear Accelerator Center (SLAC) [50]. Figure 2.1 illustrates the location of the PEP ring and the Mark II detector on the SLAC site.

In the PEP ring, three bunches of electrons and positrons circulate, colliding every 2.4 μs at each of the six interaction regions. The e^+e^- collision region (the interaction point) has an effective rms width of approximately 400 μm in the horizontal (x) direction, 70 μm in the vertical (y) direction, and 1.5 cm in the direction parallel to the beams (z). The typical luminosity seen by the Mark II at PEP was $\sim 1 \times 10^{31}\,\mathrm{cm}^{-2}\,\mathrm{sec}^{-1}$ ($= 0.01\ \mathrm{nb}^{-1}\,\mathrm{sec}^{-1}$). The integrated luminosity over the years 1981-1984 was approximately 206 pb^{-1} .

2.2 The Mark II Detector: Overview

The Mark II detector was designed and built by a collaboration of scientists from SLAC and the Lawrence Berkeley Laboratory (LBL). Completed in 1977, the Mark II first operated at the SPEAR storage ring at SLAC and accumulated data from e^+e^- annihilations at center of mass energies between 3.0 and 7.5 GeV.

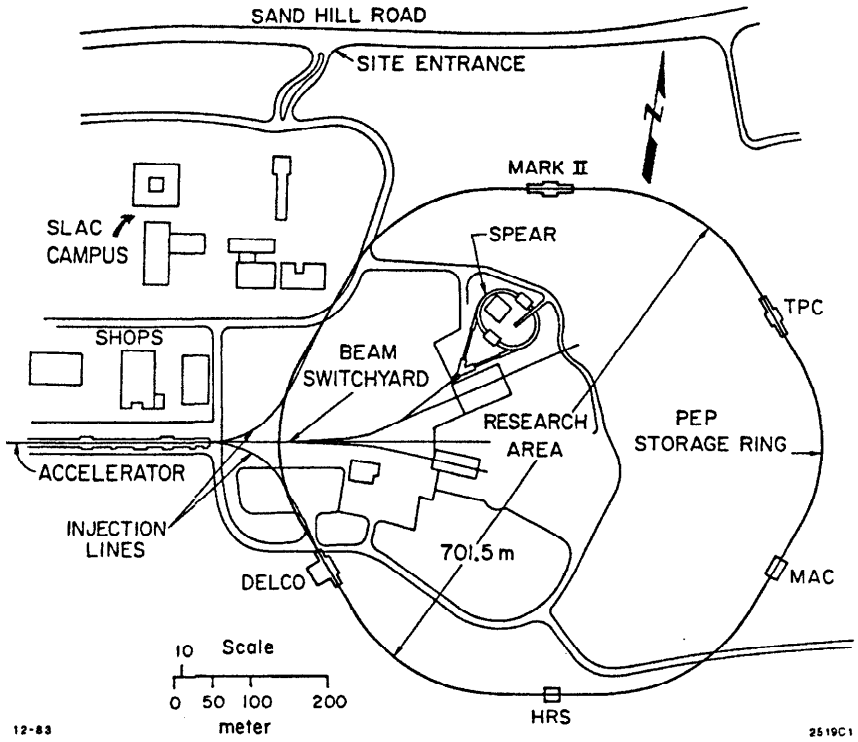

Figure 2.1: The SLAC site. Beams of electrons and positrons are accelerated to high energy by the 3 km long Linear Accelerator (not completely shown). These beams are injected into the SPEAR storage ring or into the larger PEP ring. The experiments taking data on PEP are indicated by the names next to each interaction region.

After two years of operation at SPEAR, the Mark II was moved to the larger PEP ring [51]. The detector recorded data at PEP for four years at a center of mass energy of 29 GeV. In the summer of 1981, after the first year of operation at PEP, a high precision drift chamber (the Vertex Chamber) was installed in the Mark II to improve the track position resolution. The Vertex Chamber is the single most important detector component used for the measurement presented in this thesis. For that reason, we place particular emphasis on that device.

In the summer of 1984, the Mark II detector was upgraded for operation at the Stanford Linear Collider (SLC). The analysis presented in this thesis uses only the data taken at PEP from 1981 to 1984, after the installation of the Vertex Chamber and before the SLC upgrade.

The Mark II detector at PEP is shown in Figure 2.2 ; the detector is a general purpose spectrometer designed to study the charged and neutral particles produced

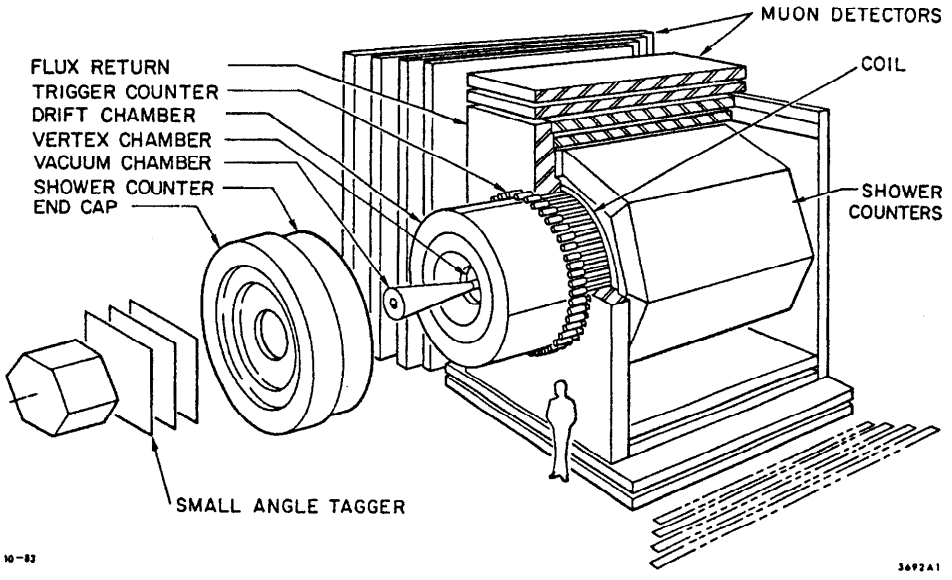

Figure 2.2: The Mark II detector.

from e^+e^- collisions [52].

The components of the Mark II detector were designed using detection methods commonplace in the field of particle physics [53]. The analysis presented in this thesis relies most heavily upon the following detector components:

- The Vertex Chamber and main Drift Chamber: These two detector elements, in conjunction with a solenoidal magnetic field, provide charged particle tracking and momentum determination. These components cover 80 % of the solid angle.
- Liquid Argon Calorimeter: This device identifies photons and electrons over 65 % of the solid angle by measuring their energy deposition.
- Muon System: This system consists of layers of hadron absorber and proportional tubes used to provide muon identification over 45 % of the solid angle.

The individual components of the detector are described in the following sections, moving radially outward from the interaction point.

2.3 Beam Position Monitors

To monitor the movement of the PEP electron and positron beams, a beam position monitor (BPM) is located on each side of the detector, 4.9 m from the interaction point along the beam line. Each monitor consists of 4 copper electrodes which protrude into the beam pipe. A passing beam bunch induces voltages on the electrodes; the voltages were read out every four minutes during data taking. An offline program used the BPM readings to produce an estimate of the average beam position over a data run (typically 1-2 hours long). Although measurements of the relative beam positions within a run have a precision of $\sim 50\,\mu$m, long term drifts in the BPM system compromise the absolute determination of the beam position. For that reason, information from the beam position monitors is used only to check for possible beam motion within an individual run. Runs having an rms spread of beam position measurements greater than $250\,\mu$m in the horizontal direction, or greater than $150\,\mu$m in the vertical direction, are eliminated. Approximately 5 % of the runs are removed by these cuts. The average beam position within a run is determined from reconstructed tracks in the Vertex and Drift Chambers, as discussed in Chapter 4.

2.4 Beam Pipe and Detector Materials

To minimize the effects of multiple scattering, the PEP beam pipe serves as the inner wall of the Vertex Chamber. The section of the beam pipe through the detector consists of a beryllium tube, 1.42 mm thick, 15.2 cm in diameter, and 1.4 m long. A $50\,\mu$m thick layer of titanium foil was placed inside of the beryllium tube to absorb synchrotron radiation.* A $50\,\mu$m thick Mylar layer was wrapped outside of the beam pipe, along with $25\,\mu$m of aluminum foil which acted as the ground shield of the chamber. Details of the beam pipe construction are illustrated in Figure 2.3.

In addition to the beam pipe material, a particle from the interaction point traverses material in the Vertex Chamber and main Drift Chamber, as listed in Table 2.1. Including the gas in the Vertex Chamber, there is only 0.7 % of a radiation length of material before the first track measurement points.

* This radiation was largely due to photons produced from the scattering of electrons off masks located 3 m from the interaction point along the beam line.

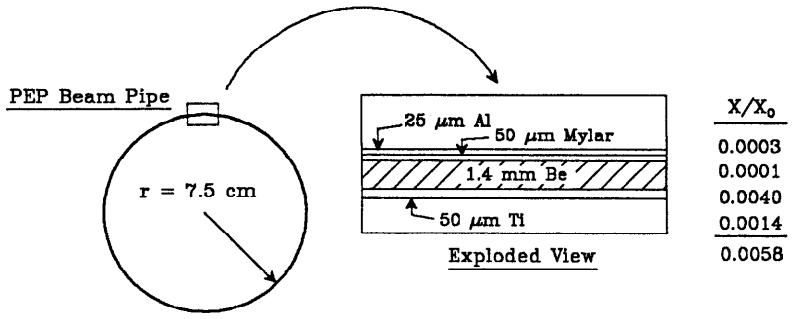

Figure 2.3: Mark II beam pipe at PEP. The exploded view shows the thickness of the materials used, along with the number of radiation lengths.

Table 2.1: Mark II detector materials. Only the materials within the Drift Chamber outer wall are tabulated. These are the materials affecting charged particle tracking.

Detector Component	Material Type	Average Radius(cm)	Thickness (cm)	Radiation Lengths (%)
Beam Pipe	Be (Ti,Mylar,Al)	7.6	0.153	0.6
VC wires	Au-Al, Cu-Be	19.9	0.017	0.1
VC gas	Ar-Ethane (50:50)	21.4	27.3	0.2
VC shell	Al	35.0	0.18	2.0
DC inner wall	Lexan	37.3	0.32	0.9
DC gas	Ar-Ethane (50:50)	93.9	112.9	0.9

2.5 Vertex Chamber

The Vertex Chamber (VC) is a cylindrical high precision drift chamber, with an outer radius of 35 cm and a length of 1.2 m [54]. Figure 2.4 shows a cross-sectional view of the Vertex Chamber.

The VC has seven layers of wires divided into two concentric bands. The inner band consists of four wire layers at an average radius of 11 cm; the outer band has three wire layers at an average radius of 31 cm. There are a total of 825 sense wires in the VC; 270 wires in the inner layers and 555 wires in the outer layers. All wires are strung in the axial direction; no attempt is made to measure the z-coordinate. In Figure 2.5, the wire pattern for a section of the inner band is shown. Sense wires

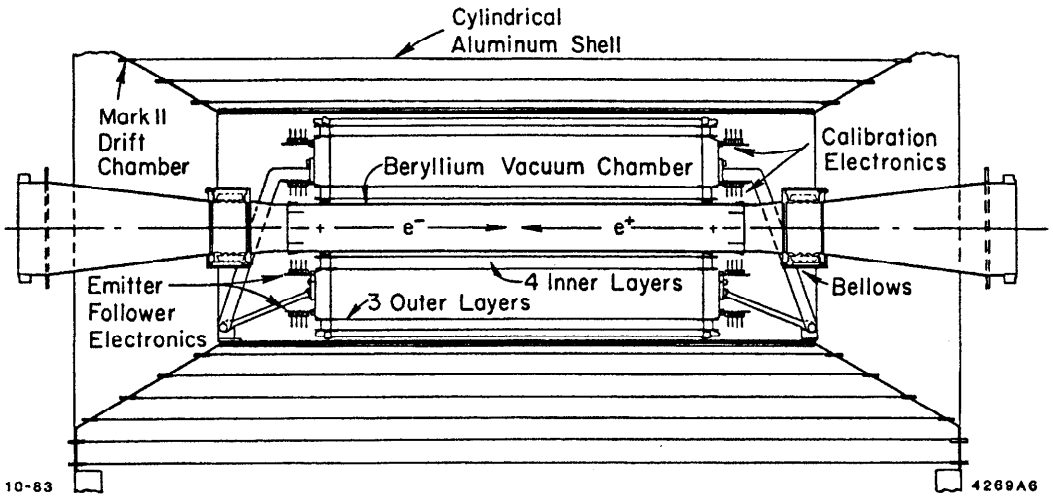

Figure 2.4: The Mark II Vertex Chamber. Cross-sectional view of the Vertex Chamber showing its position inside the main Drift Chamber and around the PEP beam pipe.

are separated from adjacent field wires by 4.2 mm in the radial direction and 5.3 mm in the azimuthal direction. The cell-to-cell cross-talk is minimized by the presence of a field wire placed almost exactly between two sense wires. 20 μm diameter gold-coated tungsten wires are used for the sense wires. The field wires in the outer band are 150 μm diameter gold-coated copper-beryllium wires and those in the inner band are 150 μm diameter gold-coated aluminum wires. The aluminum wires were chosen to minimize multiple Coulomb scattering. The chamber operated with 50:50 premixed argon-ethane gas at an absolute pressure of 15.5 $\pm$ 0.05 psi.

The excellent spatial resolution of the Mark II Vertex Chamber is achieved to a large degree by the following conditions:

1. The wires in the VC were precisely located. By the use of precision machining in the drilling of the endplates and the visual inspection of each wire feedthrough, the chamber wires were positioned to an accuracy of 20 μm throughout the array. More discussion of the feedthrough design and selection can be found in Ref. 55. The positions of the feedthrough holes were measured during construction to allow for later software correction.
2. The Vertex Chamber contains two bands of wires separated by a significant radial distance. This design feature allows precision tracking in the Vertex Chamber to be largely decoupled from the main Drift Chamber. Details of

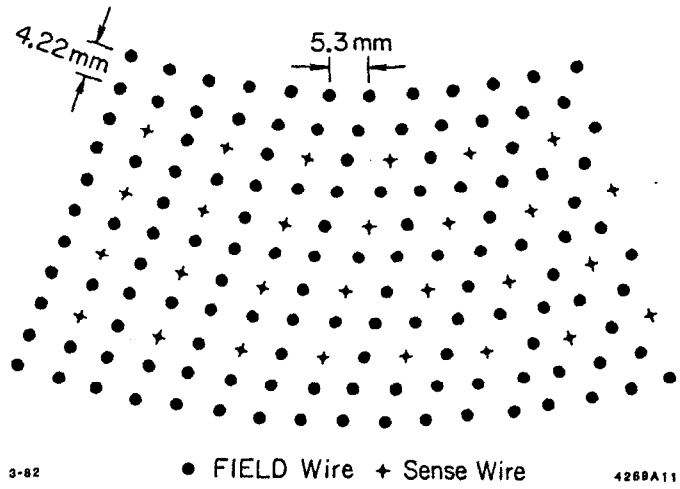

Figure 2.5: VC wire pattern. One-tenth of the inner band of wires is pictured here. Sense wire locations are given by the '+' symbol; field wire locations are given by the '• ' symbol.

tracking in the Vertex Chamber are presented in Chapters 3 and 4.

3. The multiple Coulomb scattering is minimized by the use of a thin beryllium beam pipe, as discussed in the previous section.
4. High resolution electronics are used to read out the VC signals. The electronic components used are shown in Figure 2.6. The chamber pulses are coupled to 6 m of 50 Ω coaxial cable via a fast emitter-follower mounted on the chamber endplates. The amplifier/discriminators* drive 17 m of twisted pair cable connected to a time to amplitude converter (TAC) [56], and read out with a dedicated microprocessor (BADC) [57]. The readout electronics has a timing resolution of 250 ps. Calibration every eight hours during data taking ensured a common start time on all signal channels to within 300 ps. The contribution to the position resolution of the Vertex Chamber due to the electronics is no more than 25 μm.

   In addition to the MVL-100 pre-amplifier shown in Figure 2.6, a separate transformer pre-amplifier is used on wires in the inner layers. This additional pre-amp is shown in Figure 2.7.
5. The chamber operates at high gain and high efficiency. The voltages on

* LeCroy Research Systems Model 7791 amplifier/discriminator, based on the MVL-100 chip. The MVL-100 amplifier has a rise-time of ~ 20 ns at a gain of 10.

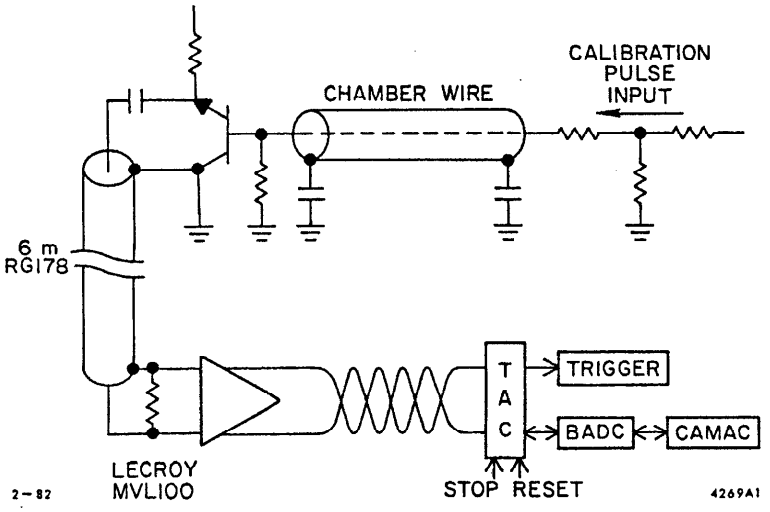

Figure 2.6: Vertex Chamber electronics.

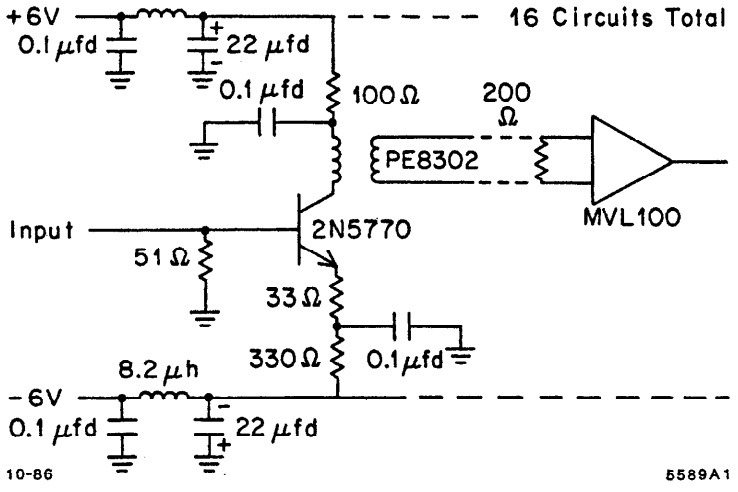

Figure 2.7: Transformer pre-amplifier circuit. These amplifiers were installed on the inner VC layers before the MVL-100 circuit; they provided a gain of three.

the field wires were set to -2.25 kV; the sense wires were placed at ground potential. This operating point yields a gas gain for the 20 μm wire of $\sim 5.0 \times 10^5$. As shown in Figure 2.8, the chamber is fully efficient at these voltages.

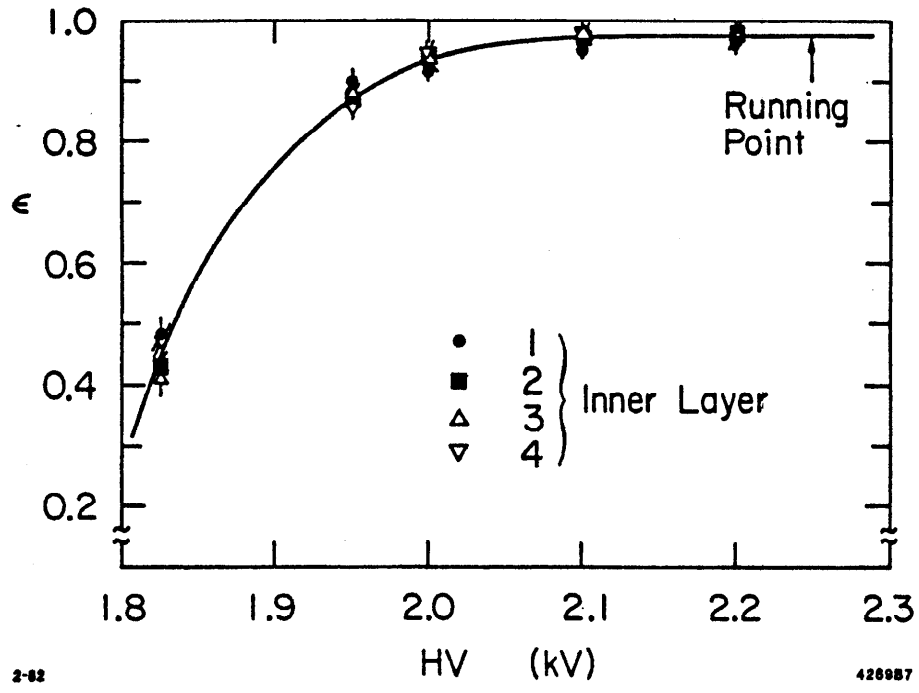

Figure 2.8: Vertex Chamber efficiency.

6. The chamber operates with a fully saturated gas (one in which the drift velocity is constant over the cell). This condition gives rise to a space-time relation (STR) (i.e. the algorithm by which the measured times are turned into drift distances) that is linear over most of the cell area. The parameters for the STR (namely the drift velocity and the time corresponding to zero drift length T_0) were monitored online and found to be very stable [58].

The position resolution for individual wires can be derived from the residual distributions for Bhabha tracks (accounting for the fact that the wire whose residual being measured is included in the fit). This position resolution, is illustrated in Figure 2.9; it is 85 μm in the center of the drift cell, rising to 100 μm at the edges of the cell. The tracking resolution relevant to impact parameters is discussed in Chapter 4.

2.6 Main Drift Chamber

The main Drift Chamber (DC) [59] consists of sixteen concentric layers of sense wires located between radii of 0.41 and 1.45 m from the beam axis. Six of the layers

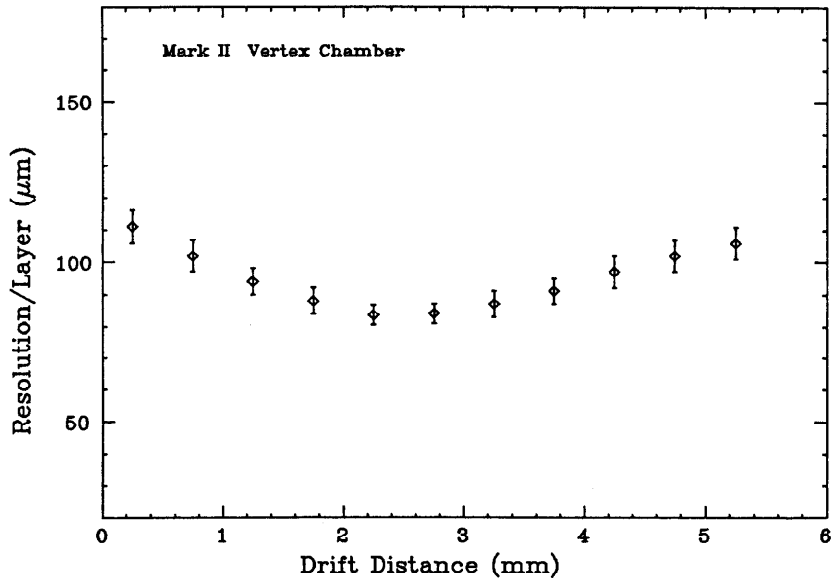

Figure 2.9: VC position resolution for a typical individual wire.

contain wires strung axially, the wires in the other ten layers are strung at a $\pm 3°$ stereo pitch. The stereo wires provide track information in the direction parallel to the beam axis. The chamber operated with 50:50 argon-ethane gas at atmospheric pressure. The inner wall of the Drift Chamber is made of Lexan; the outer shell is constructed of aluminum.

The Drift Chamber contains a total of 3204 drift cells; the wire array for a 30° sector of the chamber is illustrated in Figure 2.10. The drift cells of the six innermost layers are 1.8 cm across; they operated at an electric field strength of 900 V/cm. The cells in the outer ten layers are 3.6 cm across; they operated at 600 V/cm. The processing of the signals from the Drift Chamber sense wires is done in a similar manner to the Vertex Chamber.

The position resolution of the Drift Chamber in the plane transverse to the beam (the xy plane) is $\sim 220\,\mu$m /layer. The position resolution in the axial (z) direction is ~ 3 mm.

The Vertex Chamber and Drift Chamber have a combined momentum resolution in the xy plane of

$$\delta p/p \;=\; \sqrt{(0.025)^2 + (0.011p)^2} \quad , \tag{2.1}$$

with p in GeV/c (in a 2.3 kG field). The first term in Eqn. 2.1 is the contribution

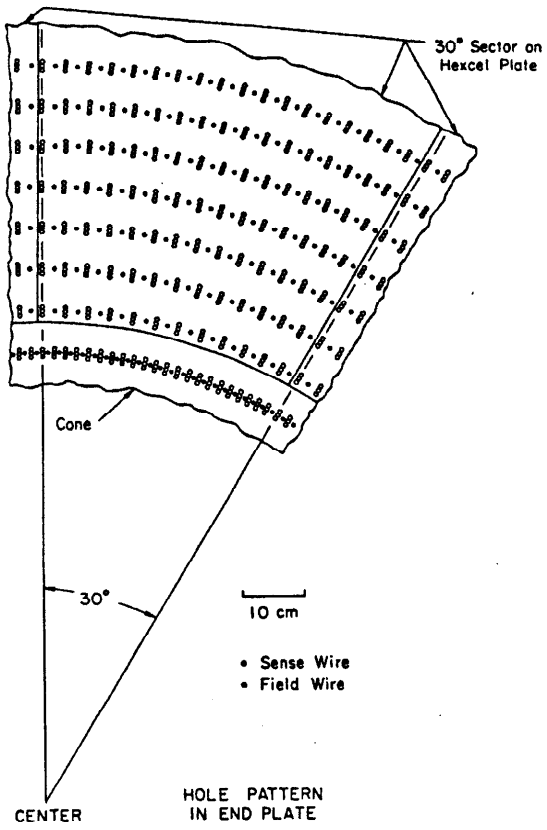

Figure 2.10: Drift Chamber wire array.

from multiple scattering (largely due to the outer VC shell and the Lexan wall); the second term comes from the measurement error made in making a χ^2 circle fit to a set of individual hits.

2.7 Magnet Coil

The Mark II magnet coil is a conventional room temperature solenoid located at a radius of 1.6 m from the interaction point. The coil consists of two water-cooled aluminum conductors separated by a layer of insulating material. These conductors have a thickness of 1.4 radiation lengths, producing a uniform magnetic field parallel to the beam axis.

Although originally designed for a field strength of 4.6 kG, the magnet coil developed a short circuit between the inner and outer conductors. Because of this short circuit, only the outer conductor was powered (giving a magnetic field strength of 2.3 kG) for essentially all of the data used in this analysis. The magnetic field

was mapped by a Hall probe before magnet installation, and was monitored online by NMR probes. These measurements lead to an accuracy of the absolute field strength of $\sim 1\,\%$.

2.8 Liquid Argon Calorimeter

The liquid argon (LA) calorimeter system consists of eight modules arranged in an octagonal array outside of the magnet coil [60]. The front of each module consists of three aluminum planes separated by 8 mm LA gaps. These planes, collectively known as the trigger gap, are designed to sample showers that begin in the 1.4 radiation lengths of magnet coil preceding the calorimeters. The remainder of each module consists of 14.4 radiation lengths of material divided into 37 layers of 2 mm thick lead planes and 3 mm thick liquid argon gaps. Alternating lead planes are kept at ground potential; the remaining planes are placed at a high voltage of +3.5 kV and segmented into readout strips. This arrangement results in eighteen readout planes, each plane corresponding to 0.8 radiation lengths of material.

As illustrated in Figure 2.11, the readout planes are ganged in the following manner:

- F planes: Nine of the planes have 3.8 cm wide strips oriented parallel to the beam line. These planes provide information about the azimuthal angle, ϕ, of a shower and are ganged into three readout layers: F1, F2 and F3.
- T planes: Six of the planes have 3.8 cm wide strips oriented perpendicular to the beam line. These planes provide information about the polar angle, θ, of a shower and are ganged into two readout layers: T1 and T2.
- U planes: The remaining three planes have 5.4 cm wide strips oriented at a 45° angle with respect to the F and T planes. These planes provide information useful in resolving multi-hit ambiguities and are ganged into one readout layer: U.

The signal on each readout strip (due to the collection of charge from the ionization of the liquid argon) is amplified by a low noise JFET mounted on the detector. The signal is then shaped to form a bipolar pulse that drives an output line. The shaped analog signal is sampled at the peak by a Sample and Hold Analog Module (SHAM) and digitized by an BADC microprocessor. The LA system

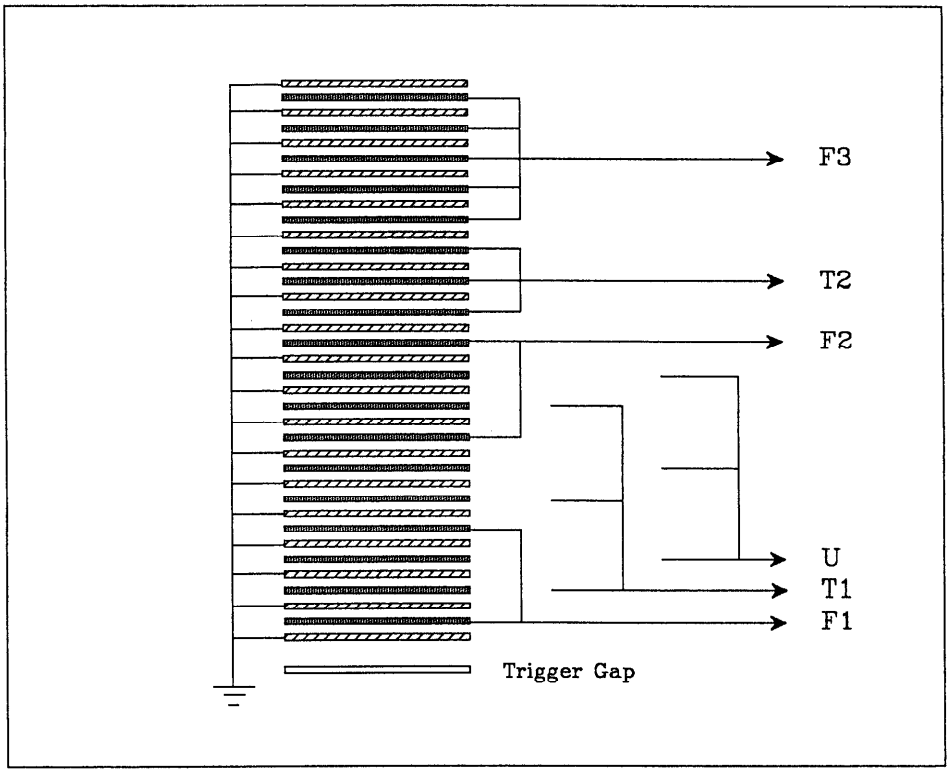

Figure 2.11: LA calorimeter ganging pattern. The strips are ganged into six different readout layers, as described in the text. Particles enter the calorimeter through the trigger gap at the bottom.

contains a total of $\sim$ 3000 electronic channels.

The calorimeter measures the entering position of a Bhabha electron to an accuracy of $\sim$ 8 mm and determines its energy with a resolution of $\sigma(\mathrm{E})/\mathrm{E} = 15\,\%/\sqrt{\mathrm{E}}$, with E in GeV. The energy deposition in the LA calorimeter for Bhabha electrons (E=14.5 GeV) is shown in Figure 2.12.

The fiducial volume of each LA module is defined to be that region of the module less than 1.75 m from the module center in z and less than 0.345 radians from the module center in ϕ. The detection efficiency for 14.5 GeV electrons within this fiducial region is greater than 98 % [61].

2.9 Muon System

The Mark II muon system consists of layers of iron hadron absorber and proportional tubes mounted on four sides around the central detector [62]. Each wall of the muon system is made up of 4 layers of alternating hadron absorber

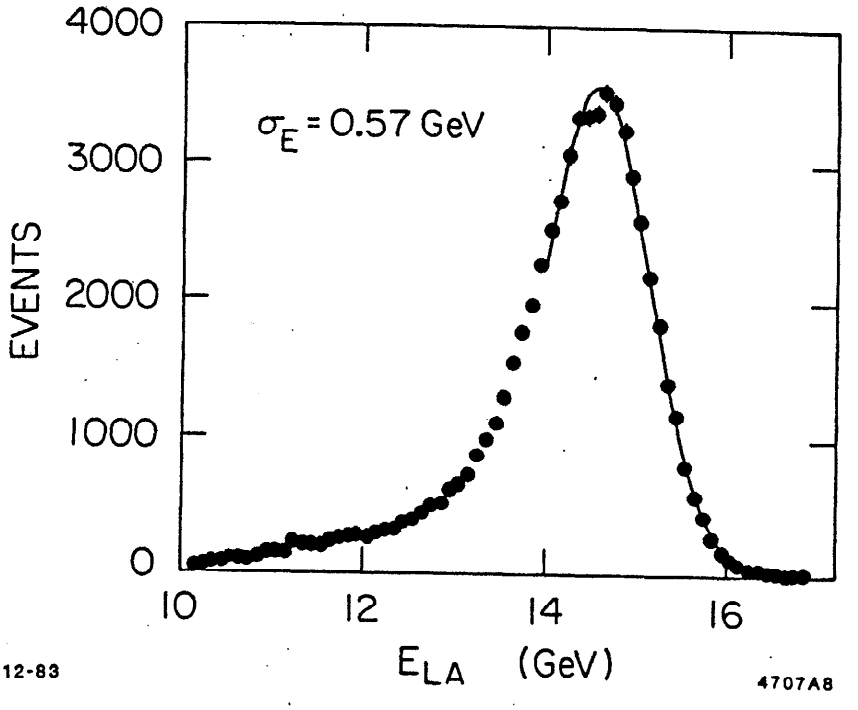

Figure 2.12: LA energy deposition. The measured energy of electrons from Bhabha events is shown. The curve corresponds to a Gaussian fit excluding the radiative tail.

and proportional tubes. The tubes in the first layer of each wall are oriented perpendicular to the beam line; they measure the polar coordinate of a track. The outer three layers are oriented parallel to the beam line in order to measure the azimuthal coordinate. The average amount of material preceding each proportional tube layer is given in Table 2.2.

Each proportional tube layer is made from extruded aluminum modules consisting of eight triangular tubes. One such module is illustrated in Figure 2.13, Each tube contains one 45 μm wire spaced 2.5 cm from the wire in an adjacent tube. The muon system contains 408 modules for a total of 3264 channels. Signals from the muon system are amplified, discriminated and stored in a shift register array. Upon receipt of the secondary trigger signal, the shift registers are read out in a serial chain.

Table 2.2: Hadron absorber thickness. The number of interaction lengths is given (averaged over the four muon walls) for a hadron at normal incidence.

Layer	Interaction Lengths
Coil and LA	1.2
1	2.6
2	4.0
3	5.8
4	7.4

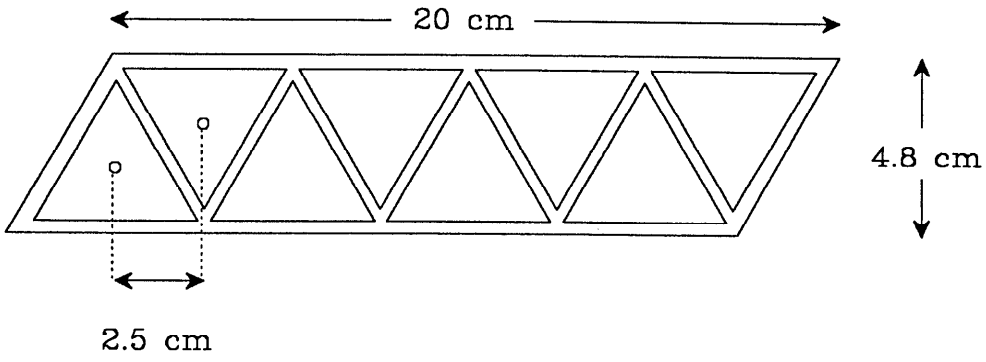

Figure 2.13: Muon system cross-sectional view. A single module is shown.

2.10 Other Systems

Several components of the Mark II detector are not directly used in this analysis. For completeness, they are briefly described here.

2.10.1 Time of flight system

The Time of Flight (TOF) system is positioned on the outside of the Drift Chamber and inside the magnet coil. This system consists of 48 plastic scintillation counters at a radius of 1.51 m; it covers 75 % of the solid angle. Each counter (1 in thick Pilot F scintillator) runs parallel to the beam direction and is viewed at each end by a photomultiplier tube. The rms timing resolution is $\sim$ 350 ps. The TOF system provides π/K separation up to a momentum of 1 GeV/c and proton identification up to 2 GeV/c. The TOF system is used in the event trigger and to reject cosmic ray events.

2.10.2 Endcap calorimeters

The endcap calorimeters are positioned at each end of the detector, covering polar angles between 15° and 40° . These calorimeters consist of 2.3 radiation lengths of lead followed by two layers of proportional chambers; they achieve an energy resolution of $\sigma(E)/E = 50\,\%/\sqrt{E}$ (E in GeV) for photons and electrons.

2.10.3 Small angle tagging system

The small angle tagging (SAT) system provides charged particle tracking and calorimetry in the region on each side of the detector at low angles (20 to 80 mr) from the beam line. The SAT system is used to detect electrons from small angle Bhabha scattering events or from two-photon interactions. From the rate of small angle Bhabha events the luminosity is determined to $\pm 5\,\%$ accuracy.

2.11 Event Trigger System

The time between beam crossings at PEP is quite short (2.4 μs); therefore a trigger system is needed to control the selective recording of data onto magnetic tape. The Mark II trigger system is composed of two levels: a fast primary trigger designed to work between beam crossings and a slower (intelligent) hardware track-finder [63].

The primary logic demands that any one of the following conditions be met in coincidence with a beam crossing signal:

Primary Trigger Conditions

1. *Charged trigger:* There must be hits in at least nine layers of the VC and DC systems and in at least one TOF counter.
2. *Neutral trigger:* The summed energy deposition in the front half of the eight LA modules and in the endcap modules must be greater than 4 GeV or there must be at least 1 GeV of energy deposited in the front half of two LA modules.
3. *Bhabha trigger:* The SAT system must signal the presence of a collinear e^+e^- event. This trigger is prescaled by a factor of 16 to reduce its rate.

The primary trigger determination takes $\sim$ 1 μs to complete, resulting in no system deadtime.

If the primary trigger logic is satisfied, data collection halts and secondary trigger processing begins. A hardware track processor searches for charged tracks employing the information from the VC, DC and TOF systems. These tracks (called hardware tracks) are identified by programmed curvature modules which search for track candidates by requiring a certain number of hits along an arc extending from the interaction point.

The secondary trigger logic requires that any one of the following conditions be met:

Secondary Trigger Conditions

1. *Charged trigger:* There must be at least two hardware tracks; each track must have momentum greater than 100 MeV/c and must lie within the central 65 % of the detector.
2. *Neutral trigger:* The same conditions as in the neutral primary trigger must be met, or there must be one hardware track found and one LA module found with energy deposition in the front half greater than 1 GeV.
3. *Bhabha Trigger:* Every one out of sixteen Bhabha primary triggers.

The secondary trigger determination takes 33 μs to complete. At a typical primary trigger rate of 1 kHz, the secondary trigger processing results in a deadtime of $\sim$ 3 %. Typical secondary trigger rates were 1-2 Hz.

2.12 Operating Conditions

The Mark II experiment accumulated a total of 206 pb^{-1} of data in three years of operation at PEP. During this time, a number of detector systems experienced hardware problems. Because of the importance of the charged particle tracking on the analysis presented in this thesis, only the problems associated with the Drift Chamber and Vertex Chamber are discussed here.

2.12.1 Drift Chamber operation

In the fall of 1982, the Drift Chamber experienced problems associated with high voltage discharge. These problems necessitated a lowering of the operating voltages in the chamber for a time; the lower voltages resulted in a reduction of 10 % in the overall tracking efficiency. Approximately 25 pb^{-1} of data were accumulated

with the Drift Chamber in this degraded condition. After the addition of 0.7 % O_2 to the gas mixture, the discharge problems were mitigated, allowing the Drift Chamber voltages to be raised to their normal level.

2.12.2 Vertex Chamber operation

As discussed in Section 2.5, the Vertex Chamber was initially operated with a voltage of -2.25 kV on the field wires and at a relatively high gas gain of $\sim 5.0 \times 10^5$. This gain yielded pulses of a few mV at the input of the discriminator, which had its threshold level set at 200 μV. The electric field strength was $\sim$ 150 kV/cm at the surface of a sense wire, $\sim$ 11 kV/cm at the surface of a field wire, and at least 1 kV/cm at any point within the drift cell.

Typical currents drawn in the first year of running were 125 nA/wire in the inner layers and 15 nA/wire in the outer layers. It was observed that the current drawn in the chamber was strongly correlated with the amount of beam current, as shown in Figure 2.14.

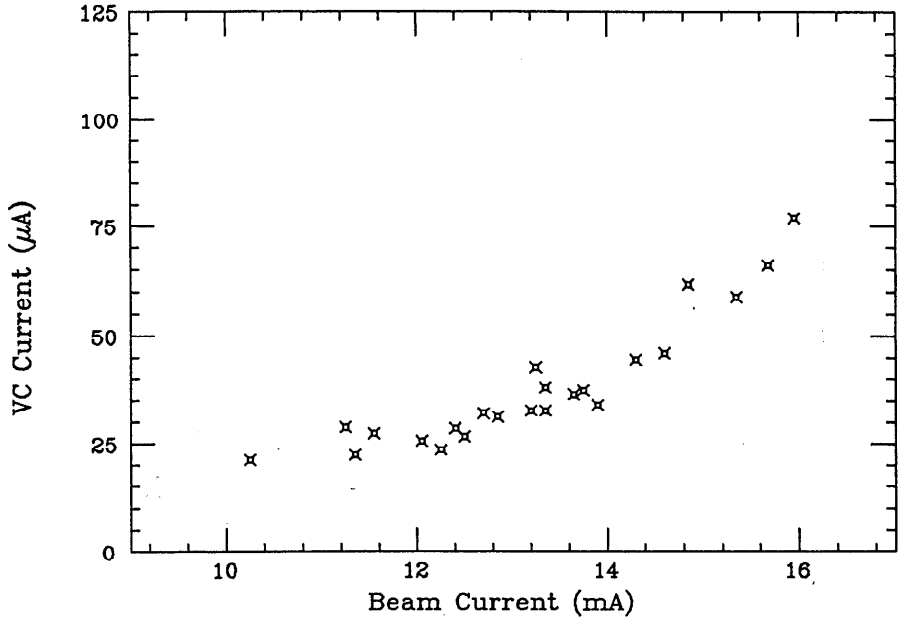

Figure 2.14: VC current versus PEP beam current. The data shown in this figure were taken in the first year of operation. The VC current is measured for the whole chamber; the beam current is the average of the electron and positron currents.

In the second year of operation, the Vertex Chamber began to have problems with high current draw ($>$ 2 μA/wire) on a few wires in the inner layers. Although

the high voltage on several wires was removed, it became difficult to operate one-fifth of the inner band of wires because of high voltage trips. The voltages on the field wires in this section were lowered to 1.95 kV and those on the wires in the remaining four-fifths of the inner band were lowered to 2.1 kV. At the suggestion of Atac [64], the chamber gas was bubbled through ethanol at 0° C, giving 1.5 % ethanol by volume. With these operating conditions, wires in the inner layers typically drew 80 nA of current each and the chamber was stable.

2.12.3 *Test chamber study*

In order to reproduce the symptoms of chamber aging seen in the VC, a small test chamber was constructed. This test chamber contained twelve complete drift cells with the same cell geometry and types of wire as in the inner band of the VC. The test chamber was operated with -2.25 kV on the field wires and with 50:50 argon-ethane gas (no ethanol). A 4.3 mCi Co^{60} source was used to bombard the chamber with radiation; this source induced $\sim$ 500 nA/wire of current. The test chamber began to show serious degradation after approximately 0.08 C/cm of charge had been collected on each wire. Once degradation was evident, a smaller 1.5 mCi Co^{60} source was used to irradiate the chamber.*

The degradation in the test chamber was characterized by symptoms quite similar to those observed in the VC. The test chamber drew large currents or suffered high voltage breakdown at the designated operating point. Reducing the high voltage lowered these currents until a threshold voltage (1.8 kV) was reached, below which the current was close to normal. By raising the high voltage again, the breakdown conditions could be re-established.† This behavior was consistent with the deposition of polymer layers on wires observed by other experimenters [65]. This layer acts as an insulator (capacitor) and allows the build-up of charge on its surface to the point where breakdown can occur. In order to determine if the breakdown behavior observed in the test chamber was consistent with the presence of a layer

* The large source was used to produce degradation in the chamber in a reasonable amount of time, while the smaller source was used to study the symptoms of the degradation after it occured. This latter source was positioned so that the amount of current drawn per wire by the test chamber was the same as that drawn by the VC in the PEP beam.

† At first, it seemed as if the threshold voltage to re-establish breakdown conditions was higher than the voltage where breakdown disappeared, i.e. that a hysteresis behavior was being observed. This hysteresis behavoir was eliminated, however, by waiting at each point while raising the high voltage.

of dielectric material, the time that the chamber took to charge-up to breakdown condition (the "breakdown time") was studied while varying the time with the high voltage off (the "relaxation time"). Figure 2.15, shows that the relaxation time varies logarithmically with the breakdown time.

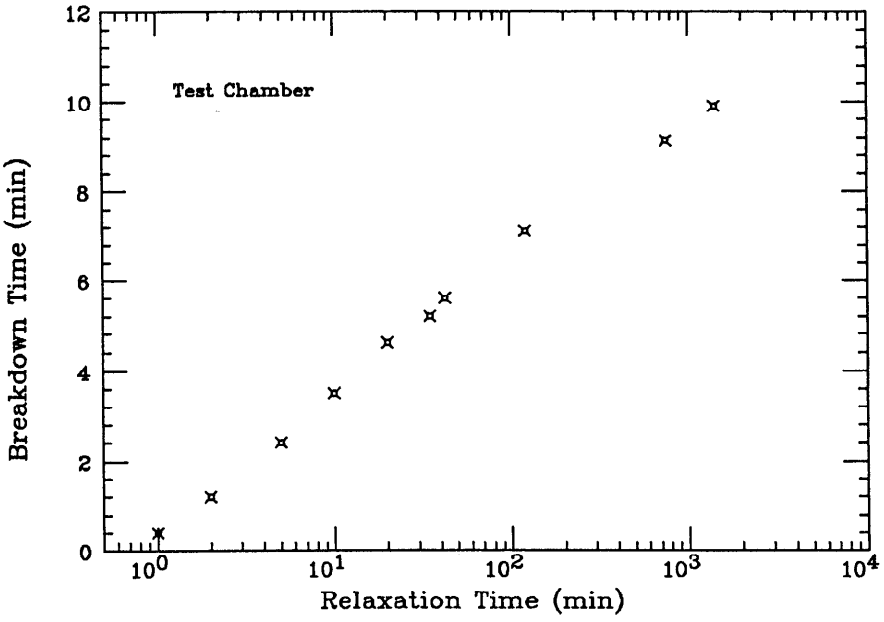

Figure 2.15: Test chamber study. This plot shows the time with high voltage off versus the subsequent time needed to re-establish breakdown conditions.

When ethanol was added, the breakdown problems in the test chamber were substantially mitigated. With ethanol, wires in the test chamber drew normal currents up to a high voltage of 2.2 kV (400 Volts above the threshold voltage without ethanol). The chamber remained stable at voltages less than 2.2 kV even after 1.4 C/cm of charge had been collected on the sense wires. A summary of the results from the lifetime studies using the test chamber is shown in Table 2.3; these results are compared to those observed by the Vertex Chamber in the PEP beam.

Wires from the test chamber were examined under a microscope and various deposits were found on both the anode and cathode wires. These deposits were found to be hydrocarbon in nature.

In order to ensure that the data taken with the ethanol added was of good quality, studies were made of the drift velocity of argon-ethane gas with alcohol added [66]. As shown in Figure 2.16, the drift velocity was still fully saturated in

Table 2.3: Chamber lifetime study. Q_1 is the charge integrated on sense wires before degradation occured; Q_2 is the charge integrated after the addition of ethanol. V_1 is the breakdown voltage, above which the chamber drew unacceptable current without ethanol; V_2 is the same quantity with ethanol. The integrated charge for the Vertex Chamber was estimated by assuming that all the charge was collected in the central 50 cm of the chamber.

Quantity	Test Chamber	Vertex Chamber
Q_1 (C/cm)	0.08	0.03
Q_2 (C/cm)	> 1.3	> 0.14
V_1 (kV)	1.80	1.75
V_2 (kV)	2.20	NA

four-fifths of the inner band of wires in the VC after the addition of ethanol. In the remaining one-fifth of the inner band, the drift velocity was saturated over most of the drift cell.

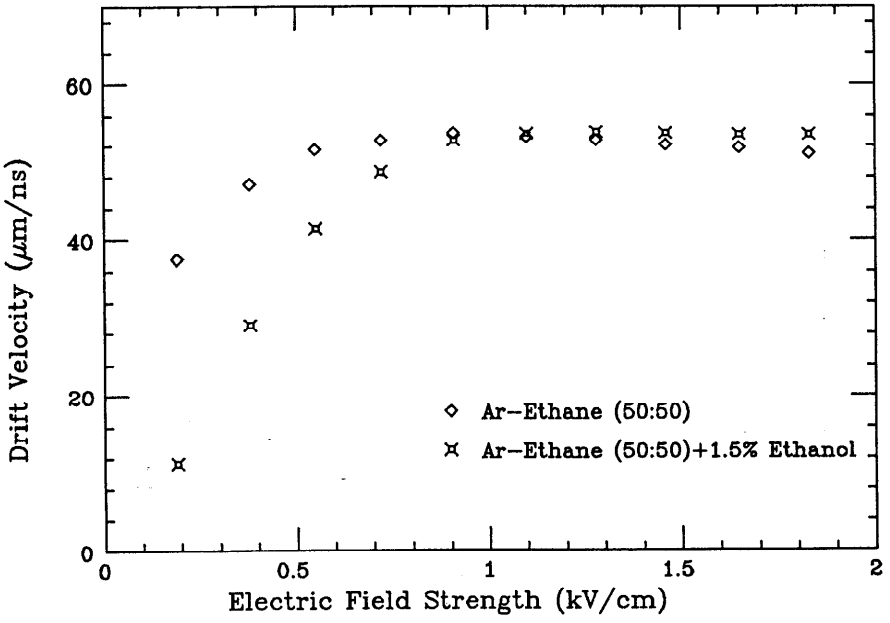

Figure 2.16: Drift velocity with and without ethanol added to VC gas. The Vertex Chamber operated at typical field strengths of $\sim$ 1.1 kV/cm (no lower than 0.9 kV/cm) for four-fifths of the inner band of wires. In the remaining one-fifth of the inner band, the field strengths were typically 0.9 kV/cm (no lower than 0.7 kV/cm).

The tracking efficiency of the Vertex Chamber with ethanol added was checked,

as illustrated in Figure 2.17. This figure indicates that the Vertex Chamber was fully efficient in the inner layers.

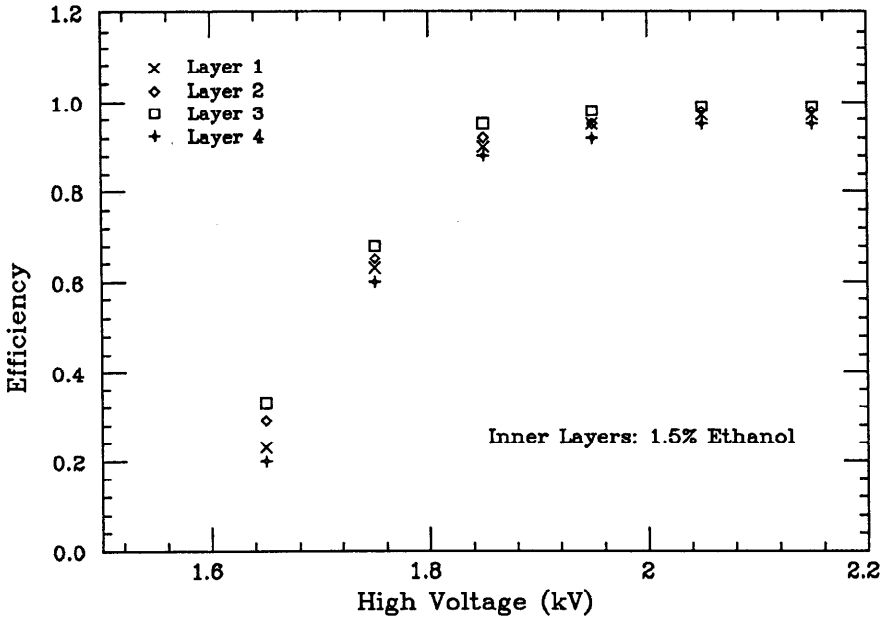

Figure 2.17: Efficiency with ethanol added to VC gas.

After the addition of ethanol, the Vertex Chamber experienced stable operations for the remaining period of data-taking at PEP. In the total three years of operations, one field wire and no sense wires were broken in the VC, although several sense wires were isolated because of unacceptable current.* A total data sample of 195 pb^{-1} was collected by the Mark II experiment with the Vertex Chamber in good operational order.

The conclusion that can be drawn from the operating experience with the Vertex Chamber, and from the test chamber studies, is that the ethanol added to the chamber's gas mixture substantially mitigated the problems associated with aging. In addition, the added ethanol did not cause any significant degradation in the chamber performance.

* One-tenth section of the outer layers developed a short in the spring of 1982. This short was caused by a small stub of wire that had been trapped inside the chamber (against the endplate) by a feedthrough during construction. The stub was surgically removed (!).

Event Reconstruction and Simulation

Before it can be used for physics analysis, the raw data taken by the experiment must be processed and manipulated into a more readily understood form. This processing, or event reconstruction, involves charged particle tracking and particle identification.

In this chapter, the basic procedure by which charged tracks are found in the Vertex Chamber and Drift Chamber is discussed. A discussion of the improvements to this basic procedure to achieve the optimum position resolution is postponed until Chapter 4. Charged tracks are extrapolated from the Drift Chamber into the LA calorimeter and muon system in order to identify electrons and muons, respectively. The procedures for lepton identification are outlined in Chapter 5; these procedures constitute the only use of particle identification in this thesis.

In addition to digesting data taken by the detector, the event reconstruction package is used to process events generated by Monte Carlo programs. These programs simulate the relevant physics for the production of final state particles from e^+e^- collisions, as well as the detector response to the final state particles. The Mark II Monte Carlo simulation is outlined in the latter half of this chapter; the optimization of the Monte Carlo is discussed. This discussion outlines the basic properties of C and B hadron production and decay not covered in Chapter 1.

3.1 Charged Track Reconstruction

Track reconstruction is initiated by a pattern recognition algorithm which assigns individual drift points in the VC and DC to a track. This algorithm also makes a first attempt at resolving the left-right ambiguities of each drift time. A χ^2 minimization technique is then used to fit the chosen drift times to a helical track orbit [52,67]. The χ^2 used in this minimization has the form:

$$\chi^2 = \sum_{i=1}^{N} \frac{\left(D^i_{fit}(\alpha_j) - D_{str}(t_i)\right)^2}{\sigma_i^2} , \tag{3.1}$$

where N is the total number of hits associated with the track, D^i_{fit} is the distance of closest approach from the fitted track to the wire i, $D_{str}(t_i)$ is the distance of closest approach to the same wire as determined from the space-time relation using the measured time, and σ_i is the expected position resolution of the hit. The orbit of the fitted track depends on the parameters α_j; these parameters are the track curvature, the polar and azimuthal angles, the distance of closest approach to the origin (DC center) in the xy plane and the distance of closest approach to the origin along the beam line (z). An additional parameter is used in the fit to allow for a kink in the track due to multiple Coulomb scattering at the boundary between the VC and DC. Minimization of the track χ^2 in Eqn. 3.1 yields the optimal orbit parameters for a track.

In the determination of the track χ^2 the positions of the wires used in the track fit and the space-time relation (STR) must be known. The wire positions are initially chosen to be the feedthrough hole positions. Additional parameters are then introduced to describe the geometrical orientation of the VC relative to the DC coordinate system. These parameters, and more accurate determinations of the wire positions, are found by iteratively minimizing the χ^2 equation. The space-time relation is found by the same iterative procedure. In the case of the VC, the STR is parameterized by a polynomial function (up to third order) of the drift time. (For complete details on the determination of the STR, see Ref. 55.) The parameters for the STR of the Vertex Chamber are accurately determined using high momentum tracks; in this determination, the data are divided into run blocks of approximately one week duration. The VC space-time relation is found to be quite linear over

most of the drift cell. As discussed in Section 2.5, this linearity is due to operating the chamber with a fully saturated gas. The χ^2 minimization procedure is also used to determine the dependence of the expected resolution (i.e. σ_i in Eqn. 3.1) on drift distance. As illustrated in Figure 2.9, the VC resolution is nearly flat as a function of drift distance.

Tracks are reconstructed by the procedure described above with high efficiency ($>$ 98 % for isolated tracks) over 75 % of the solid angle. Bhabha tracks are used to determine the momentum resolution of the VC and DC systems in the 2.3 kG magnetic field, yielding the expression given in Eqn. 2.1. The momentum resolution is improved by 15 % by constraining tracks to pass through the interaction point.*

3.2 Monte Carlo Simulation

A detailed set of Monte Carlo programs are used to simulate events in the Mark II detector. These routines can be divided into two sections: the hadronic event generator and the routines subsequently used to trace particles and their decay products through the detector.

In this analysis, the event generator used is that incorporated in the LUND model [68], JETSET version 6.3. The event generator initially produces partons (quarks and gluons) resulting from the electron-positron collision using a second order matrix element calculation. Although two parton ($q\bar{q}$) states are the most common, the event generator also produces three ($q\bar{q}g$) and four ($q\bar{q}q\bar{q}$, $q\bar{q}gg$) parton states. The relative production of two, three and four parton states is determined by the strong interaction coupling constant α_s, and by a parameter $y_{\rm min}$. This latter parameter is the minimum scaled invariant mass two partons must have to prevent them from being combined into one. As discussed in Chapter 1, hadrons are produced from the partons by the process of fragmentation. In this analysis, light quarks (u, d and s) are fragmented according to the LUND string scheme [69]. Heavy quarks (c and b) are fragmented using the Peterson formula. The values used for some of the more important parameters of the Monte-Carlo event generator are given in Table 3.1.

Except for the heavy quark fragmentation function parameters (i.e. ϵ_c and ϵ_b),

* This type of constraint is not done in this analysis because we are interested here in the decay of particles giving tracks with finite impact parameters.

Table 3.1: Event generator parameters. The LUND parameters A and B control the light quark fragmentation function, as well as the overall multiplicity for all quark species.

Parameter	Description	Value
$\Lambda_{\overline{MS}}$	QCD scale (GeV)	0.5
$y_{\min}$	Cutoff for combining partons	0.015
A	Light quark frag. (LUND)	0.9
B	Light quark frag. (LUND)	0.7
ϵ_c	Charm quark frag. (Peterson)	0.05
ϵ_b	Bottom quark frag. (Peterson)	0.005
σ_q	Parton Gaussian p_t (GeV/c)	0.265

the values for the parameters in this table are determined by adjusting the Monte Carlo to reproduce measured distributions (e.g. the overall multiplicity, thrust and p_t distributions) [70]. The values of the heavy quark fragmentation function parameters are determined by fitting the inclusive lepton spectra.

Each particle that is produced by the event generator is propagated through the various elements of the detector and allowed to decay according to its known lifetime and branching ratios. The effects of multiple Coulomb scattering, energy loss (radiation and DE/DX), photon conversions and nuclear interactions are taken into account. Charged particles leave hits in the Vertex and Drift Chambers. The drift times are derived from an inverted form of the measured space-time relation and are smeared with the expected resolution function. Single cell inefficiencies and dead wires are included in the simulation of the drift chambers. Electromagnetic interactions in the LA calorimeter are simulated by the EGS shower code [71]. A library of pion interactions from a 4 GeV/c pion beam test run is used to simulate hadronic interactions in the LA calorimeter. The simulation of the muon system includes the effects of range straggling, proportional tube inefficiencies, tracking extrapolation errors and hadron punchthrough.

3.3 Optimization of the Monte Carlo

In order to ensure that the Monte Carlo simulation is reasonably correct, it is important to compare results of the simulation to measured data. For the time being, we limit this comparison to showing that the Monte Carlo accurately reproduces some general distributions. The comparison of the detector simulation to the data is considered later.*

3.3.1 *Charged particle multiplicity*

The charged particle multiplicity in hadronic events from e^+e^- collisions at 29 GeV/c has been measured by the Mark II detector at PEP [72]. The Monte Carlo parameters are tuned to reproduce the results of this measurement, as well as results from other experiments. In this thesis, the multiplicity of heavy quark events is of greater interest than multiplicity averaged over all quark species. A well identified lepton of momentum greater than 2 GeV/c signals the presence of heavy quark decay. In Figure 3.1, the charged particle multiplicity distribution observed in the data for such events is compared to the distribution generated by the Monte Carlo. The data and simulation agree, indicating that the overall multiplicity in heavy quark events is well understood. In a separate analysis of Mark II data, the charged particle multiplicities for charm and bottom events have been measured to be $13.2 \pm 0.5 \pm 0.9$ and $16.2 \pm 0.5 \pm 1.0$, respectively [73].

3.3.2 *Event thrust*

The jet-like structure of hadronic events from e^+e^- interactions was first observed in the SLAC-LBL magnetic detector at center of mass energies of 6.2 and 7.4 GeV [74]. Results from experiments at higher center of mass energies show even more pronounced jet-like behavior [75]. This behavior can be understood in terms of fragmentation of the partons produced from the e^+e^- collision into hadrons with limited transverse momentum relative to the original parton direction [76]. The parameters sphericity and thrust have been introduced to quantify the two-jet

* In this analysis, great importance is placed on the detector's ability for precision charged particle tracking and lepton identification. These topics are considered in Chapters 4 and 5, respectively.

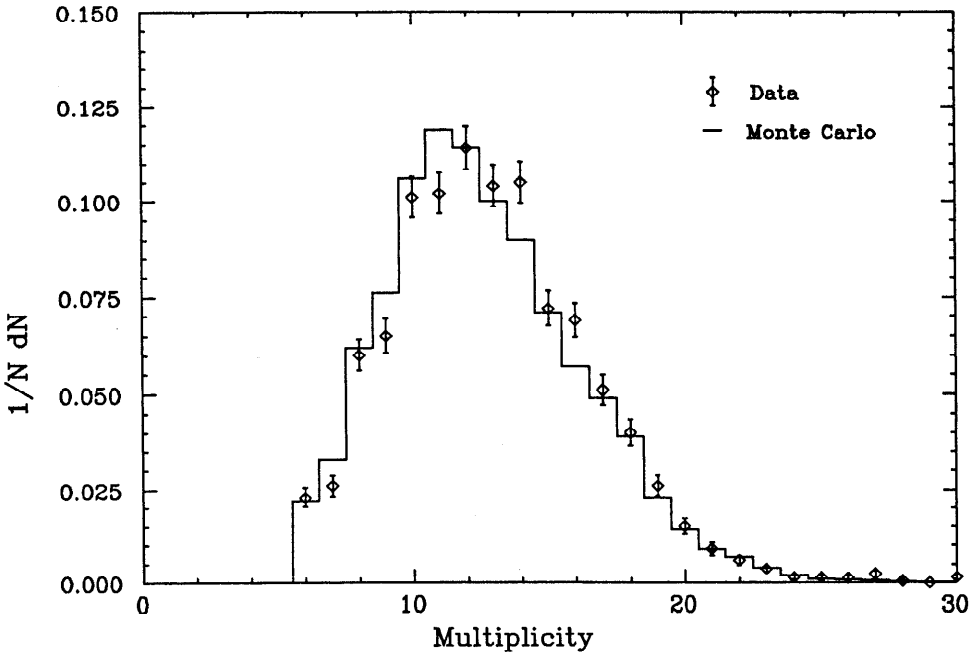

Figure 3.1: Charged particle multiplicity. Events are required to have a lepton of momentum greater than 2 GeV/c. The amount of background to the lepton signal in the Monte Carlo is adjusted to agree with the amount seen in the data. The lower edge of the multiplicity distribution is cut off by the hadronic event selection criteria.

nature of events [77]. The event thrust is defined as:

$$T \equiv \max \frac{\sum_i |p_{ij}|}{\sum_i |p_i|} , \tag{3.2}$$

p_i is the momentum of particle i and p_{ij} is the longitudinal momentum of the same particle relative to the thrust axis. The sums are performed over all the particles in the event; the thrust axis is chosen so as to maximize the event thrust.

In this analysis, the thrust axis serves several important functions. The leptons p_t is defined relative to the thrust axis. This axis serves as an estimate of the B hadron direction and determines the impact parameter sign. To ensure that the event thrust is being calculated in a reasonable manner, we compare the distribution of thrust seen in the data with that expected from the Monte Carlo in Figure 3.2, for a set of data enhanced in heavy quark production.

It is important to understand how good the thrust axis estimates the B hadron direction. In Figure 3.3, the rms error made in this estimate is plotted as a function

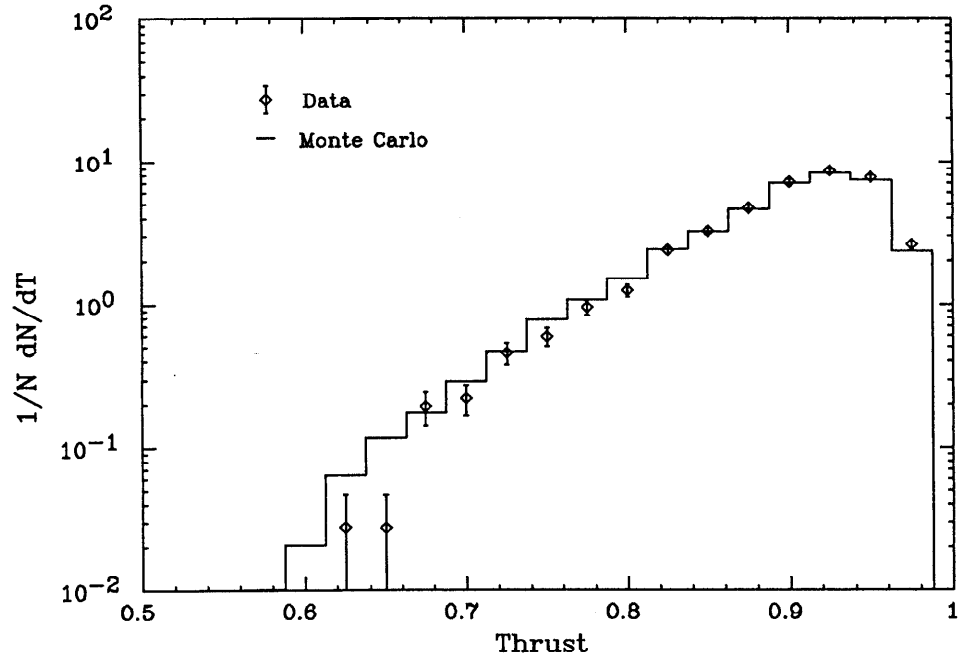

Figure 3.2: Event thrust comparison. The magnitude of thrust in the data is compared with that expected seen in the Monte Carlo. The thrust is calculated from charged tracks only. Only events containing a lepton with momentum greater than 2 GeV/c are used.

of the magnitude of thrust for $b\bar{b}$ events in the Monte Carlo. It is convenient to parameterize the thrust axis error as:

$$\sigma_\phi \;=\; 0.12 + 2.50\,(1-T)^2 \;;\quad T \in (0.75, 1.0)\;, \tag{3.3}$$

where σ_ϕ is the angular thrust axis error and T is the magnitude of thrust. This parameterization comes from a quadratic fit to the data in Figure 3.3. In Chapter 9, the systematic error in the lifetime measurement introduced by not perfectly determining the B hadron direction is discussed.

3.3.3 *Charm and bottom hadron production and branching ratios*

The Monte Carlo is adjusted to incorporate the known production and decay properties of charm and bottom hadrons. The relative ratios for the production of D^0 /D^+ /D_s^+ /Λ_c^+ charm hadrons are taken to be 0.52/0.26/0.14/0.08, respectively (the Λ_c category contains all possible types of charm baryons). These ratios agree with measurements of the relative charm production from other experiments

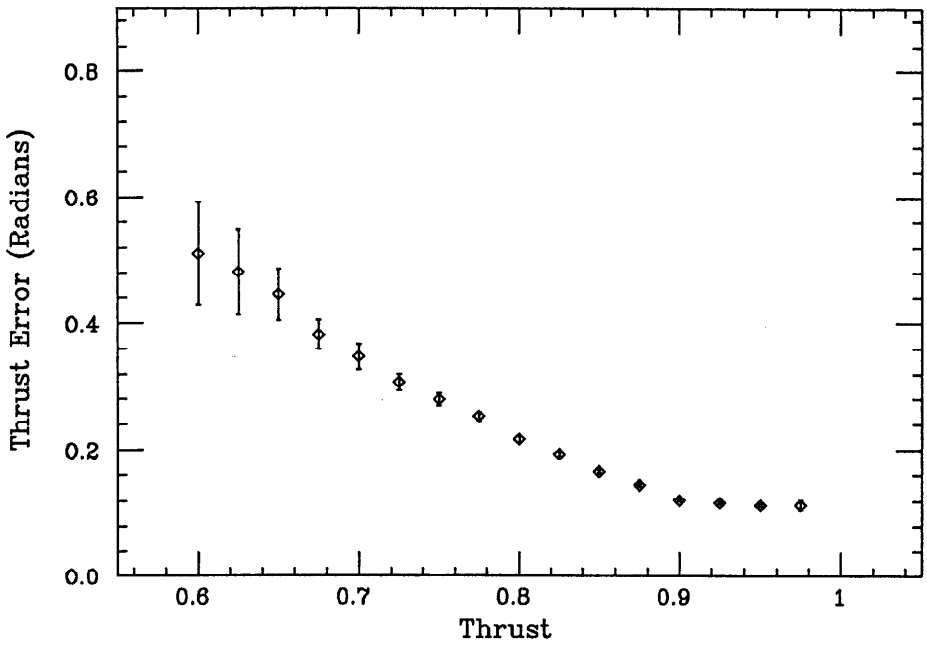

Figure 3.3: Thrust axis error. The thrust axis error in a $b\bar{b}$ event is defined as the rms angular difference in the xy plane between the measured thrust axis and the true B hadron direction. The increase in this error at lower values of thrust is due to a larger percentage of three jet events there.

[78]. The production of D^0 and D^+ mesons are controlled by a number of things, including the amount of their direct production, as well as production from secondary D^* or B hadron decays.* The amount of D_s production in the Monte Carlo is determined by the strange quark suppression factor (i.e. the ratio of strange quark to up or down quark production, here taken to be 0.33). The amount of charmed baryon production is determined by the suppression factor for di-quark production (here taken to be 0.09) and by phase space considerations.

The branching ratios for the decay of the charmed hadrons are taken from measurements, where available. The branching ratios for the D^0 and D^+ are taken to agree with recent measurements from the Mark III collaboration at the ψ'' resonance [79]. The measured exclusive branching ratios for D^0 and D^+ account for most ($\sim$ 85 %) of their possible decays; therefore, it is not surprising that the multiplicity generated by the Monte Carlo for charm decays agrees well with that

* The production of D^0 mesons is enhanced relative to that of the D^+ mesons because of the large number of D^0 's produced from D^* decay. The ratio of spin one (D^{*0}, D^{*+}) to spin zero (D^0 ,dplus) charm meson production is taken to be 3:1. D^{*0} decays 100 % of the time to D^0; D^{*+} decays 64 % of the time to D^0 and only 36 % of the time to D^+.

measured by the Mark III collaboration. The fraction of D^0 and D^+ decays not accounted for by inclusive measurements, as well as D_s^+ and Λ_c^+ decays, are done by phase space production of hadrons according to LUND string model.

The relative ratios for the production of $B^0/B^+/B_s/\Lambda_b$ bottom hadrons are taken to be 0.42/0.42/0.14/0.02, respectively. These ratios are determined by the suppression factors for strange quark and di-quark production; there is no B^0 enhancement like that for the D^0. Since a very small percentage of bottom hadron decays have been exclusively reconstructed, the Monte Carlo uses the weak decay matrix element for all bottom decays. In this scheme, a B hadron decays into a charm jet and a virtual W boson. The charm jet is fragmented into hadrons according to the string model and the quarks from the virtual W decay are converted into particles, according to phase space in the W rest frame. The branching ratios assumed for B meson decay are given in Table 3.2.

Table 3.2: B meson branching ratios in the Monte Carlo. The semi-leptonic branching ratios measured in this analysis agree with the values given below. The final entry in the table corresponds to inclusive ψ and ψ' production.

W product	Spectator product	Branching ratio
$e\ \nu_e$	c jet	0.11
$\mu\ \nu_\mu$	c jet	0.11
$\tau\ \nu_\tau$	c jet	0.03
$\bar{u}d, \bar{d}u$ jet	c jet	0.55
$\bar{c}s, \bar{s}c$ jet	c jet	0.18
$\bar{c}c$ jet	s jet	0.02

In the Monte Carlo, it is assumed that the bottom quark couples only to the charm quark (i.e. that the $(b \rightarrow u)$ coupling is zero). The relative yields of charm mesons produced from B decay in the Monte Carlo can be compared to measurements made by the CLEO and ARGUS experiments [80,81]. The fraction of D^0 and D^{*+} mesons produced per B meson decay is given in Table 3.3. This table also includes a comparison of the average charged particle multiplicity in B meson decays in the Monte Carlo with that seen by CLEO [82].

Table 3.3: Charm production and mean multiplicity in B meson decay. $<D^0>/B$ and $<D^+>/B$ represent the average number of D^0's and D^+'s produced per B meson decay, respectively, including those produced via D^* decays. The numbers in the data column are calculated from the average of the results from CLEO and ARGUS [80], adjusted to account for new measurements of the D^0 and D^+ branching ratios [79]. $<N>_{Lep}$ corresponds to the average number of charged particles in semi-leptonic B meson decays; $<N>_{Had}$ represents the same quantity for hadronic B meson decays.

Quantity	Data	MC
$< D^0 > / B$	0.58 ± 0.06	0.62
$< D^+ > / B$	0.25 ± 0.05	0.28
$< N >_{Lep}$	3.8 ± 0.4	3.8
$< N >_{Had}$	6.0 ± 0.3	5.8

3.3.4 Charm and bottom hadron decay spectra

In this thesis, we measure the average charm and bottom hadron lifetimes using a set of events in which a lepton from a heavy hadron decay is identified. The impact parameters for such leptons and the heavy flavor enrichment fractions depend on the lepton (p, p_t) distributions. It is important, therefore, to ensure that the lepton (p, p_t) distributions in the Monte Carlo agree with those in the data. These distributions depend on the initial hadron momentum spectrum as well as the momentum distributions of leptons in the hadron decay rest frame. The hadron momentum spectrum is calibrated in this analysis from the measurement of $<z>$ of the fragmentation function. The lepton decay momentum distributions are adjusted in the Monte Carlo to fit measured decay spectra from other experiments.

In Figure 3.4, the electron momentum spectrum from the decay $D \rightarrow Xe\nu$ used in the Monte Carlo is compared to data taken by the Mark III and DELCO collaborations at SPEAR [83,84]. The electron momentum spectrum used in the Monte Carlo for the decay $B \rightarrow Xe\nu$ is compared in Figure 3.5 to data taken by CLEO [85]. The muon momentum spectrum from CLEO is in good agreement with that for electrons, but with significantly poorer statistics. The spectrum shown in Figure 3.5 is also in agreement with less precise measurements from the CUSB group [86], and with preliminary results from the ARGUS collaboration [80].

Although less important for our purposes than the leptonic spectra, the

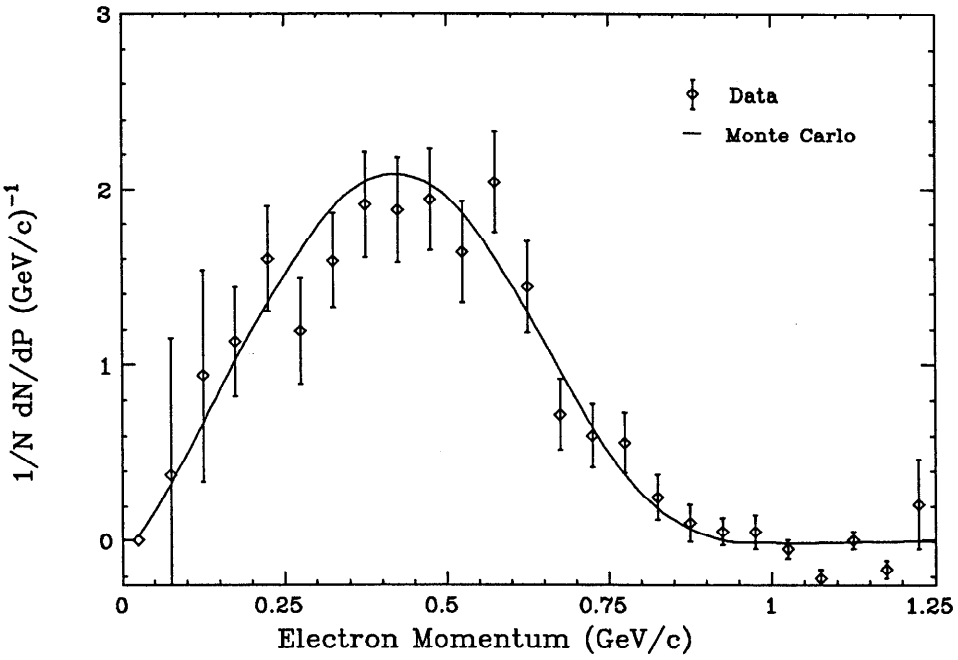

Figure 3.4: Electron momentum spectrum from D decay. The data values used are determined from an average of the D^0 and D^+ measurements made by the DELCO and Mark III groups.

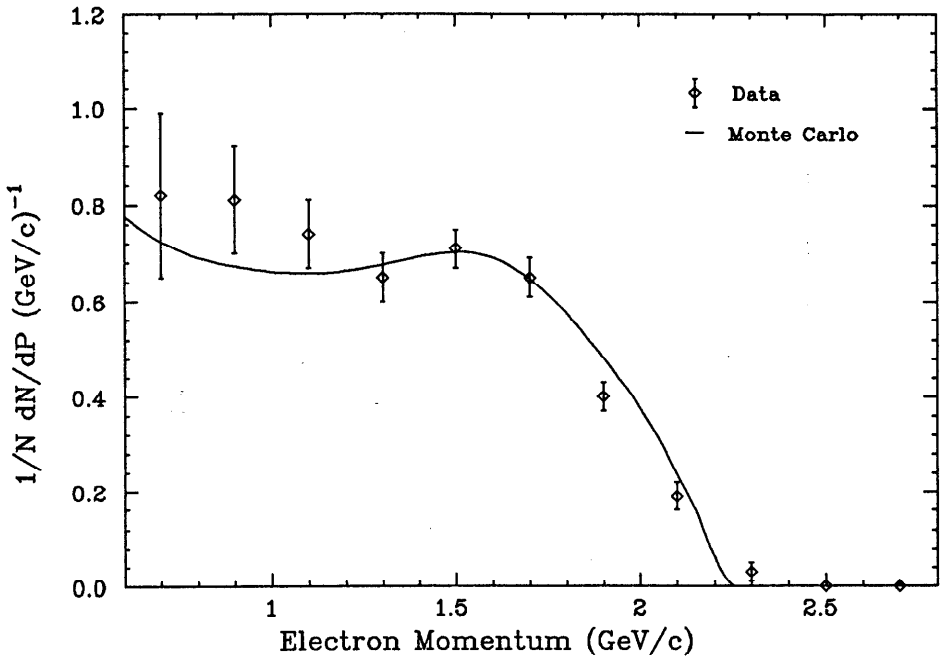

Figure 3.5: Electron momentum spectrum from B decay.

momentum distribution for D mesons from B decay is adjusted in the Monte Carlo to agree with the data given in Ref. 81. The momentum distribution for D^0 mesons from B decay is shown in Figure 3.6.

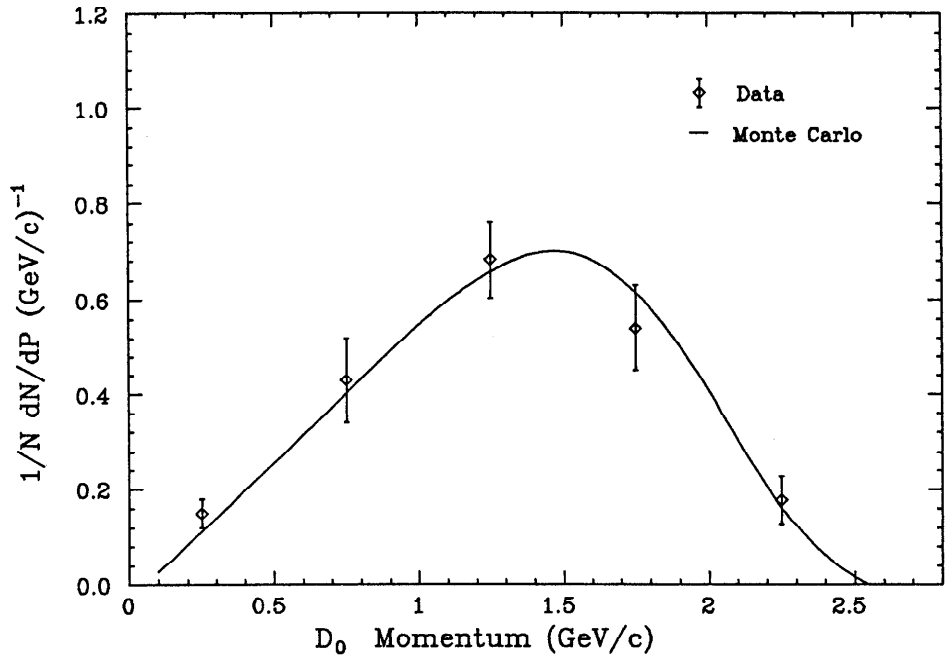

Figure 3.6: D^0 momentum spectrum from B decay. In this plot, the D^0's can be produced directly from B meson decay, or from the secondary decay via the D^*.

There is also data on the momentum spectra of D^+ and D^{*+} mesons from B decay. Although this data is less precise than that of the D^0, it shows similar good agreement when compared to the Monte Carlo. Since D^0 and D^+ mesons are found in $\sim$ 80 % of all B decays, the agreement between the Monte Carlo and data on the momentum spectra for these mesons indicates that the Monte Carlo accurately reproduces most of hadronic B decays.

3.3.5 Charm and bottom hadron lifetimes

Charm hadron lifetimes have been measured by a number of experiments. The lifetimes for the different charm hadrons used in the Monte Carlo are listed in Table 3.4. These values are taken from world averages [80].

Using the lifetimes listed in Table 3.4 and the relative production ratios for the various charm hadrons given previously, the average charm hadron lifetime at PEP

Table 3.4: Charm hadron lifetimes. The lifetimes used in the Monte Carlo for various charm hadrons are listed in this table. All charm baryons are given the same lifetime as the Λ_c.

Particle	Lifetime (ps)
D^0	0.43 ± 0.02
D^+	1.03 ± 0.05
D_s^+	0.35 ± 0.06
Λ_c^+	0.19 ± 0.05

energies is:

$$< \tau_c > \; = \; 0.56 \; \pm \; 0.09 \text{ ps} \quad . \tag{3.4}$$

The error on the average lifetime is estimated by combining the errors on the separate charm hadron lifetimes together and by including the uncertainty in the relative production of the various charm hadrons. More relevant for this analysis is the average charm lifetime in semi-leptonic events:

$$< \tau_c >_{SL} \; = \; 0.68 \; \pm \; 0.12 \text{ ps} \quad ; \tag{3.5}$$

this average lifetime is determined from the individual charm hadron lifetimes weighted by their relative production ratios *and* by their branching ratios into leptons. The semi-leptonic branching ratios for D^0 , D^+ , D_s^+ , and Λ_c^+ hadrons are taken to be 17.0 %, 7.5 %, 10.0 % and 5.0 %, respectively. The first two values are taken from measurements [9]; the latter two are simply estimates.

The lifetimes for the different types of B hadrons are set equal to each other in the Monte Carlo. For cases in which the average B hadron lifetime is not important (such as in measuring the thrust distribution or multiplicity distributions), it is set to 1.1 ps (consistent with the world average given in Ref. 80). For situations where the Monte Carlo is used to understand the sensitivity of the analysis to the assumed B lifetime, the input lifetime is allowed to vary from 0.0 to 4.0 ps. This range in the assumed lifetime is used to ensure that we are capable of measuring a B hadron lifetime consistent with zero or considerably larger than the average of previous measurements.

Tracking and Resolution Studies

In this chapter the precision tracking of charged particles in the Mark II detector is discussed. Tracking of this type depends almost completely on the performance and position resolution of the Vertex Chamber. This chapter presents a complete description of the issues relevant to VC tracking.

The method by which tracking in the Vertex Chamber is decoupled from that in the Drift Chamber is first discussed. A number of improvements to the tracking procedure are outlined; these improvements result from a careful chamber survey made via wire residual distributions. From a study of the distributions of track χ^2 values and impact parameters, it is shown that the VC resolution is well understood for isolated tracks and for tracks in hadronic events. Understanding the resolution for this latter set of tracks is vital because such tracks are used in the lifetime determination.

4.1 Vertex Chamber Tracking

The basic tracking procedure treats the Vertex Chamber and Drift Chamber as a single large system. Although this procedure is optimal in determining track momenta and in finding tracks with high efficiency, it does not provide the most accurate tracking in regard to position resolution. Any geometrical aberrations in the DC, or in the relative alignment between the VC and DC can translate into increased (systematic) error in extrapolating tracks to the origin. For that reason, after the track-finding procedure is applied, tracks are refit by an algorithm which

allows separate track fits in the Vertex Chamber and Drift Chamber [87]. These fits are allowed to be discontinuous by as much as 0.3 mr in ϕ and 200 μm in the xy plane. By means of this technique, the Vertex Chamber with its higher resolution and smaller systematic errors, is largely responsible for determining the track position in the xy plane. The Drift Chamber remains primarily responsible for determining the track curvature, polar angle and z position.

4.2 Wire Residual Survey

With the algorithm for tracking in the Vertex Chamber established, we now turn our attention to a survey of the Vertex Chamber wires. This survey was made to correct for position offsets, timing offsets, and defects in tracking due to various hardware problems. Wires were studied in this survey by means of their residual distributions.

An individual wire residual is defined by:

$$R_i = |D_i| - D_{str}(t_i) \ . \tag{4.1}$$

Here D_i is the distance of closest approach of the fitted track to the sense wire. $D_{str}(t_i)$ is the distance determined from the space-time relation for the measured time t_i. The sign of the residual defined in Eqn. 4.1 is determined by the difference in the absolute value of the fitted distance minus the measured distance; a residual defined in this manner probes any systematic bias in the space-time relation.*

The following quantity is quite useful:

$$\frac{R}{\sigma} \equiv \frac{|D_i| - D_{str}(t_i)}{\sigma(t_i)} \cdot \sqrt{\frac{N}{N-2}} \ , \tag{4.2}$$

where $\sigma(t_i)$ is the expected error for the measured time t_i and N is the number of hits on the track. As discussed in Section 3.1, the expected error is found from minimization of the track χ^2 . (The square root term in Eqn. 4.2 accounts for the fact that the residual distribution will be narrower than the actual error because the

* One can also define a residual signed on the basis of ambiguity (i.e. whether a track passes on the right or the left of a wire). This latter type of residual is used to look for geometric bias (e.g. wire position offsets).

wire was used in the fit. This term is an approximation for the full expression of the weighted residuals). If there is no bias in tracking, either in offset or in estimated error, the distribution of residuals for a wire should be centered on zero and the distribution of $\frac{R}{\sigma}$ should be a unit width Gaussian centered on zero.

The residual distributions for all wires in the Vertex Chamber were studied for Bhabha events in various run blocks of the data. Bhabha events were used because of their simplicity in comparison with the more complicated topology of hadronic events. As a result of this study, the following software fixes were implemented:

1. Each wire location was corrected for the feedthrough hole positions measured during the chamber construction. After these corrections, a few percent of the wires had residual distributions offset from zero by more than $\sim 25\,\mu$m . These residuals became centered on zero after corrections were applied for wire position offsets. An example of a wire with a position offset is shown in Figure 4.1.

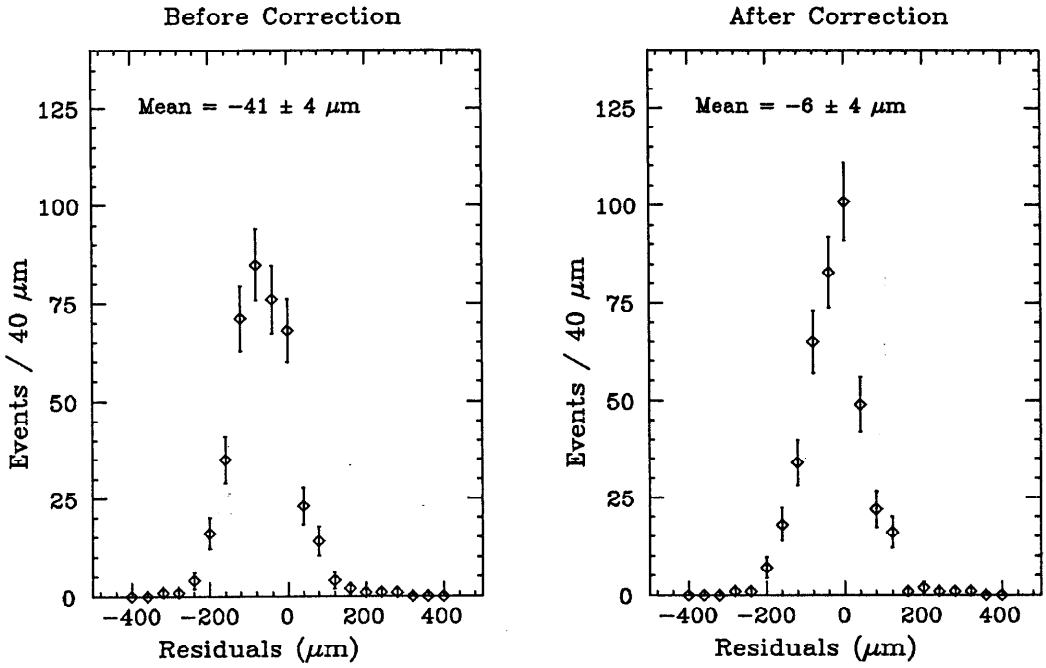

Figure 4.1: Wire position offset correction. The residual distribution for a wire is shown before and after correction for a position offset.

2. A few percent of the wires were corrected for T_0 offsets (i.e. offsets in the time corresponding to zero drift distance). An example of a wire with a T_0

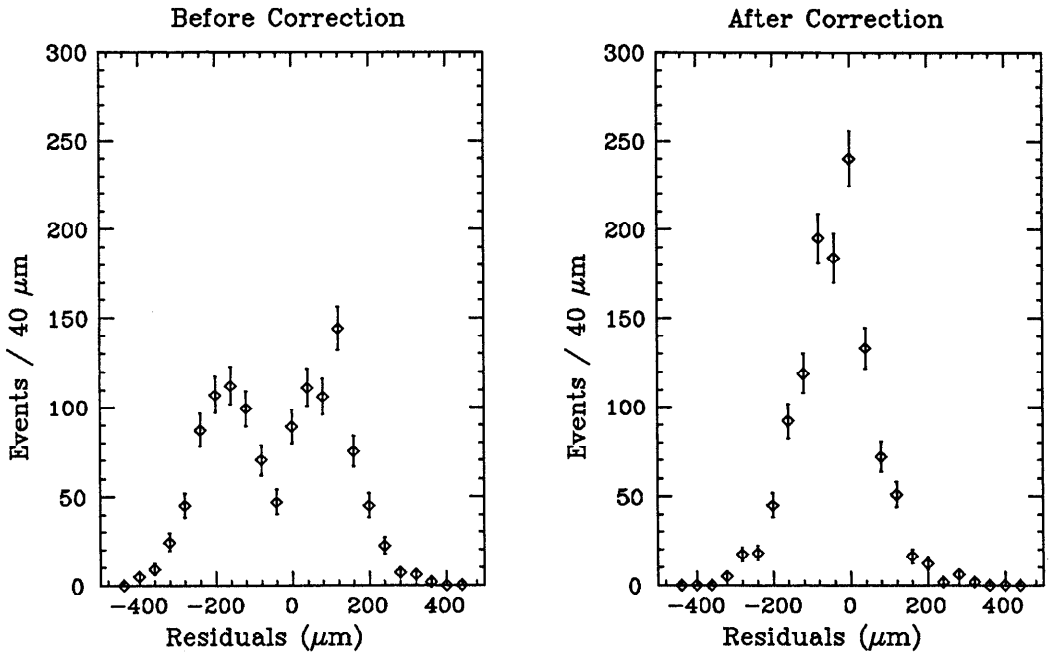

Figure 4.2: Wire T_0 offset correction. The residual distribution for a wire is shown before and after correction for a T_0 offset.

offset is shown in Figure 4.2.

3. A few wires had very broad residual distributions resulting from serious chamber or electronic problems. No attempt was made to salvage the information on these wires; they were removed from track fitting.
4. As discussed in Section 2.12, a one-fifth section of the inner layers in the Vertex Chamber experienced high current that necessitated a reduced operating voltage. The residual distributions in this section were significantly broadened and skewed from zero; this behavior was attributed to a somewhat non-linear space-time relation in the region. By constructing separate space-time constants for this region, these residual distributions were improved. The distributions for wires in this region were still broader than those in the rest of the chamber by $\sim$ 50%, but were centered on zero. The expected error for tracks passing through this region was increased to account for the degraded resolution.
5. The space-time relation was modified to account for slight non-linearities observed at long and short drift distances.

Using these fixes, the inclusive residual/error distribution for all hits on Bhabha tracks was examined. This distribution was found to have a mean consistent with zero and a width consistent with one, indicating that on an individual hit level, Vertex Chamber tracking for Bhabha events is well understood.

4.3 Study of Isolated Tracks

Although the individual wire residual distributions are understood, we would also like to verify the correctness of our reconstruction programs for whole tracks. To do this, we examine the track χ^2 distribution and the resolution of tracks extrapolated to the interaction point. The extrapolated track resolution is a major contributor to the impact parameter resolution for the lepton tracks from which the B hadron lifetime is determined. (The other contributor to the impact parameter resolution is the uncertainty in the position of the e^+e^- interaction point due to the finite beam sizes).

For the time being we concentrate on tracks that are isolated (e.g. those in Bhabha and two-photon events). Later, we turn our attention to tracks in the more dense environment of hadronic events.

4.3.1 Isolated track χ^2

The χ^2 for the track fit has been defined previously (Eqn. 3.1). In the track fit in which the VC is largely decoupled from the DC, the VC becomes responsible for determining two track orbit parameters (e.g. the impact parameter at the origin and the azimuthal angle ϕ). Therefore, the χ^2 distribution for tracks with N hits should agree with a classical χ^2 distribution for $N-2$ degrees of freedom. The χ^2 distribution for Bhabha tracks with seven hits in the VC is shown in Figure 4.3. The good agreement between the measured χ^2 distribution and the expected distribution indicates that the hit errors assumed in the track fit are correct.

4.3.2 Bhabha separation distance

Now consider the extrapolation of tracks back to the interaction point. A schematic drawing of the tracks in a Bhabha event near the interaction point is shown in Figure 4.4. This figure illustrates the elliptical shape of the PEP beams.

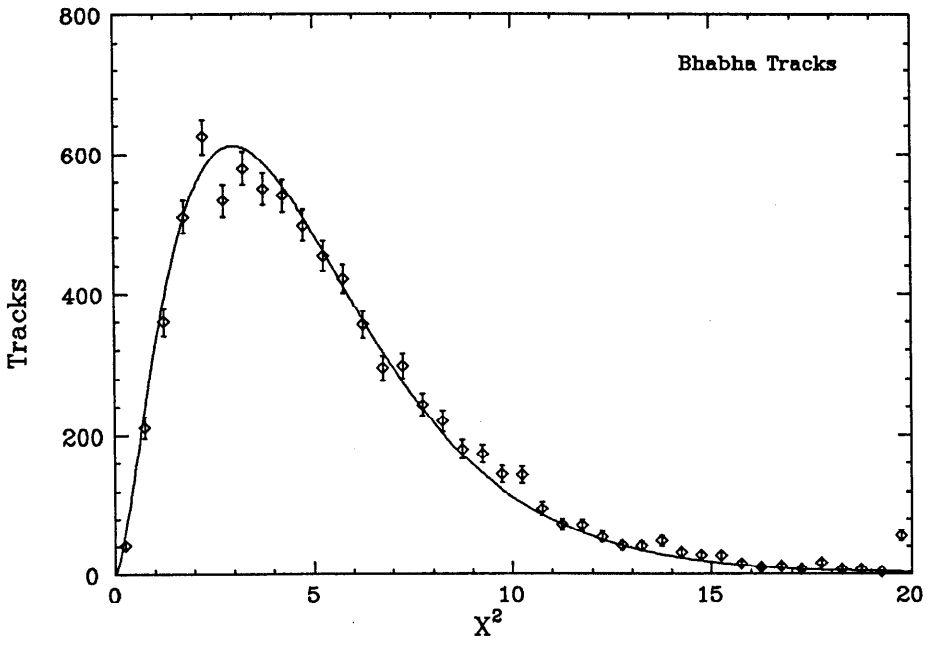

Figure 4.3: Track χ^2 distribution for Bhabha events. Tracks are required to have seven hits in the VC. The curve drawn is the expected χ^2 distribution for five degrees of freedom.

The major axis of the ellipse runs parallel to the horizontal (x) direction. The size of this ellipse is determined in the next section; for the time being, we wish to measure the extrapolated track resolution of the Vertex Chamber independent of the beam spread. To do this, we take advantage of the back-to-back topology of the tracks in Bhabha events and calculate the separation distance between the tracks, as indicated in Figure 4.4.

The separation distance for Bhabha events in a subset of the Mark II data in shown in Figure 4.5.*

Since Bhabha tracks have high momenta, multiple Coulomb scattering does not contribute to the error in the separation distance. The width of the separation distance distribution should be equal to the extrapolated track resolution for two tracks combined in quadrature. The width of the distribution in Figure 4.5 divided by $\sqrt{2}$ gives an extrapolated track resolution $\sigma_{ext} = 83.4\ \mu\text{m}$. A plot of the

* The sign of the separation distance is determined by the following convention: consider the vector formed by the cross product of the z direction and the positron direction $\vec{z} \times \vec{e}^{+}$. The separation distance is signed positive (negative) if this vector points toward (away from) the electron track. In Figure 4.4, the separation distance is negative. Tracks going through the inner section of the VC with degraded resolution are not included in Figure 4.5; the separation distance distribution for such tracks has a 50 % larger width.

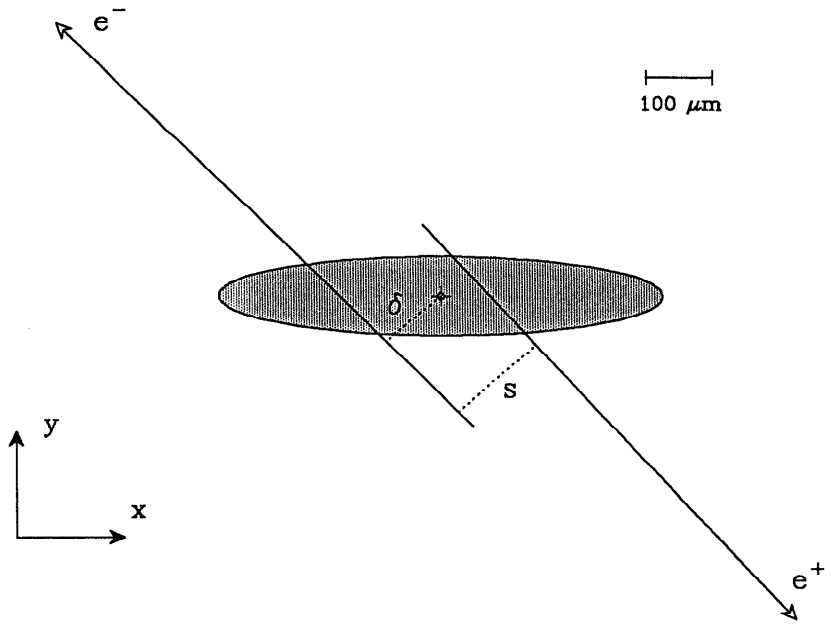

Figure 4.4: Schematic close-up of the interaction point. A Bhabha event is shown projected onto the xy plane with the beam size indicated by the shaded ellipse. The average beam position is the center point of the ellipse. The separation distance is the segment labelled S; the impact parameter for the electron track is labelled δ.

separation distance over the expected error on the same set of data yields a unit width Gaussian. This result indicates that the extrapolated track resolution is well understood with the same errors used to give the nice χ^2 and residual results discussed earlier.

4.3.3 *Measurement of multiple scattering contribution*

There is approximately 0.7 % of a radiation length of material preceding the first measurement points of the Vertex Chamber (see Table 2.1). The amount of scattering expected from this material can be calculated using the standard formula for multiple Coulomb scattering [9,88]. This calculation gives a contribution to the error on the impact parameter measurement of:

$$\sigma_{mcs} = \frac{95\,\mu\mathrm{m}}{p_{xy}}, \tag{4.3}$$

for p_{xy} in GeV/c. Although there is no reason that the actual amount of scattering is grossly different from that given in Eqn. 4.3, it is reasonable to check it.

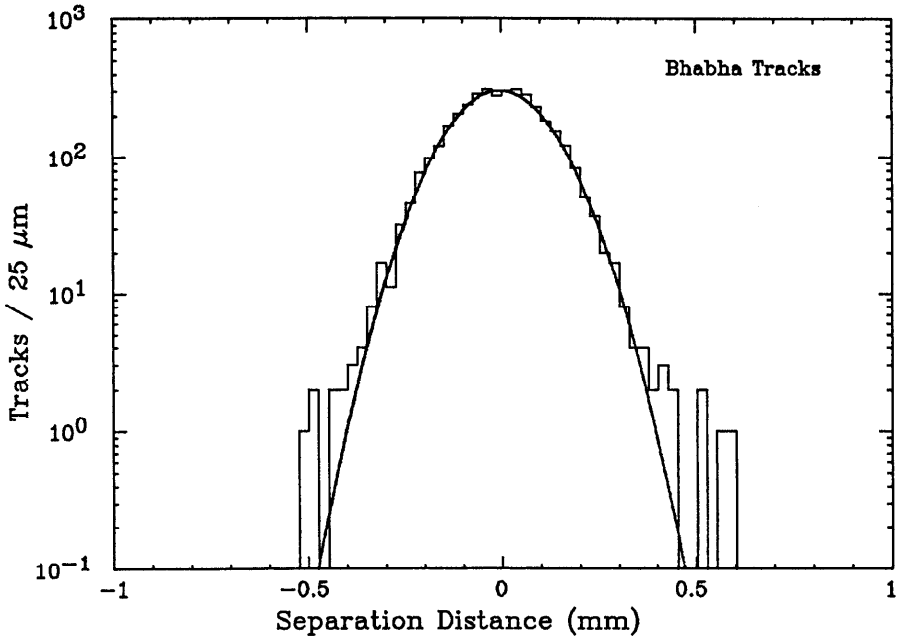

Figure 4.5: Bhabha separation distance. Tracks in this plot are required to have at least four VC hits and a track χ^2 probability fit larger than 0.1 %. The curve drawn corresponds to a Gaussian fit to the data out to ± 3 standard deviations.

The amount of scattering can been determined by measuring the impact parameter distribution for tracks in two-photon scattering events. In this measurement, events of the type $e^+e^- \rightarrow e^+e^-e^+e^-$ and $e^+e^- \rightarrow e^+e^-\mu^+\mu^-$ are used, where two leptons are scattered into the central detector and the other two escape along the beam axis. The criteria for selecting events of this type have been described previously [89]. These events are chosen because they contain tracks produced at the interaction point (i.e. there is no lifetime bias). The tracks are at low momenta and are well isolated, enhancing the amount of scattering and permitting quality tracking, respectively.

The impact parameter δ of each track that passes minimum quality cuts is measured in the xy plane with respect to the beam position. The event axis is determined by the momentum sum of the two tracks in the central detector. The sign of the impact parameter is determined by whether a track crosses the event axis at a point in the same hemisphere as the track (+), or at a point in the opposite hemisphere (−). Because the momentum sum of the two tracks in the xy plane is close to zero, this method effectively randomizes the sign. In order to maximize the contribution of multiple Coulomb scattering to the impact parameter error, only

horizontal tracks with momentum below 2 GeV/c are used. Figure 4.6 shows the distribution of impact parameter divided by the expected error for tracks in these two-photon events. The expected error includes an amount of scattering equal to that given in Eqn. 4.3. The distribution has a width equal to one within 5 %, verifying the assumed amount of scattering. Since multiple Coulomb scattering contributes 35 % of the impact parameter error, this measurement of the amount of scattering is accurate to about 15 %.*

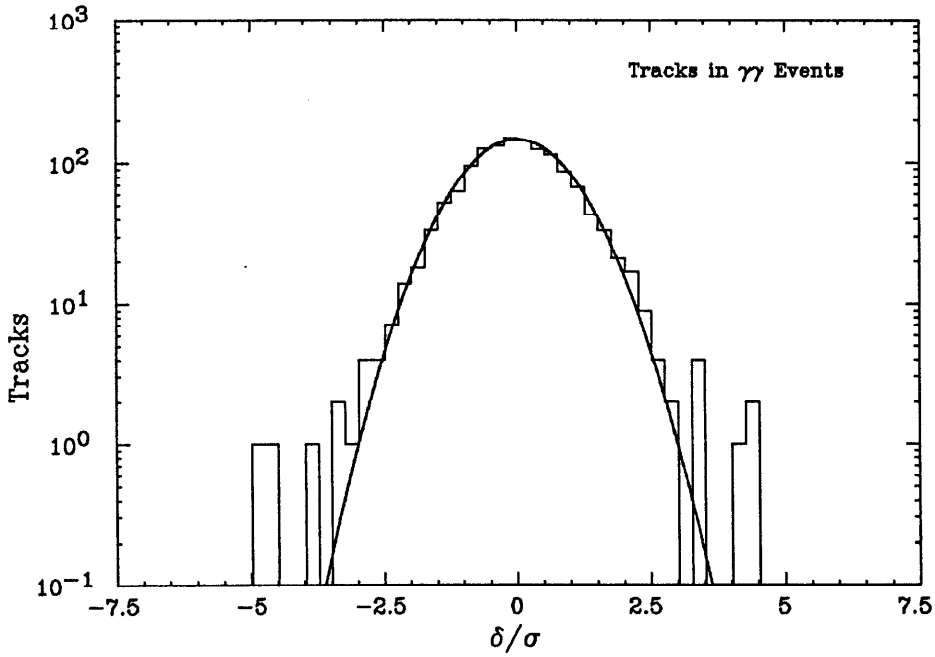

Figure 4.6: Impact parameter/error distribution for two-photon events. The fit curve is a Gaussian of width equal to 0.98.

To summarize, the overall impact parameter resolution in the Vertex Chamber is measured to be:

$$\sigma_{VC}\,[\mu\mathrm{m}] \;=\; \sqrt{(83)^2 + \frac{(95)^2}{(p_{xy})^2}} \tag{4.4}$$

p_{xy} corresponds to the track momentum in the xy plane in GeV/c. The first term

* Tracks used in the B lifetime analysis have an average momentum above 3 GeV. Therefore, the uncertainty in the amount of multiple Coulomb scattering induces negligible systematic error.

in Eqn. 4.4 is the intrinsic extrapolated track resolution of the Vertex Chamber; the second term is the contribution to the resolution from multiple Coulomb scattering.

4.4 Beam Parameters

4.4.1 Beam position determination

The technique for determining the average beam position has been described in another thesis [55]. This technique looks at the average intersection point of good tracks taken from blocks of ten to twenty runs (typically several days). Tracks within a few degrees of the vertical (horizontal) direction determine the horizontal (vertical) position of the beam. The statistical error on the location of the beam position determined by this method is $\sim 15\,\mu$m in both x and y.

This method of beam position determination requires data from a large number of runs. Therefore, its accuracy could be compromised if there was a significant amount of beam steering between fills of the PEP machine. To study the effects of beam steering between runs, an algorithm for determining the beam position within a single run was developed [58]. This algorithm uses all the good tracks in a run; it determines the beam position by minimizing the impact parameters for the entire ensemble of tracks. Beam positions are determined by this method with a statistical precision of $\sim 20\,\mu$m in the vertical direction and $\sim 50\,\mu$m in the horizontal direction. There is good agreement between the two different estimates of the beam positions. In addition, as outlined in Section 2.3, blocks of data having excessive beam motion within a run are eliminated by using the information from the hardware Beam Position Monitor.

The impact parameter distribution for Bhabha tracks provides a useful check on the azimuthal symmetry of the Vertex Chamber and on the accuracy of beam position determination. In Figure 4.7, the mean Bhabha impact parameter is plotted as a function of the azimuthal angle ϕ. The impact parameter is defined to be positive (negative) if the vector formed from the cross product of the z direction and the track direction points toward (away from) the beam position. On the scale of $\sim 20\,\mu$m, no angular dependence of the mean impact parameter is observed.

4.4.2 Beam size determination

The PEP vertical and horizontal beam sizes are determined from the

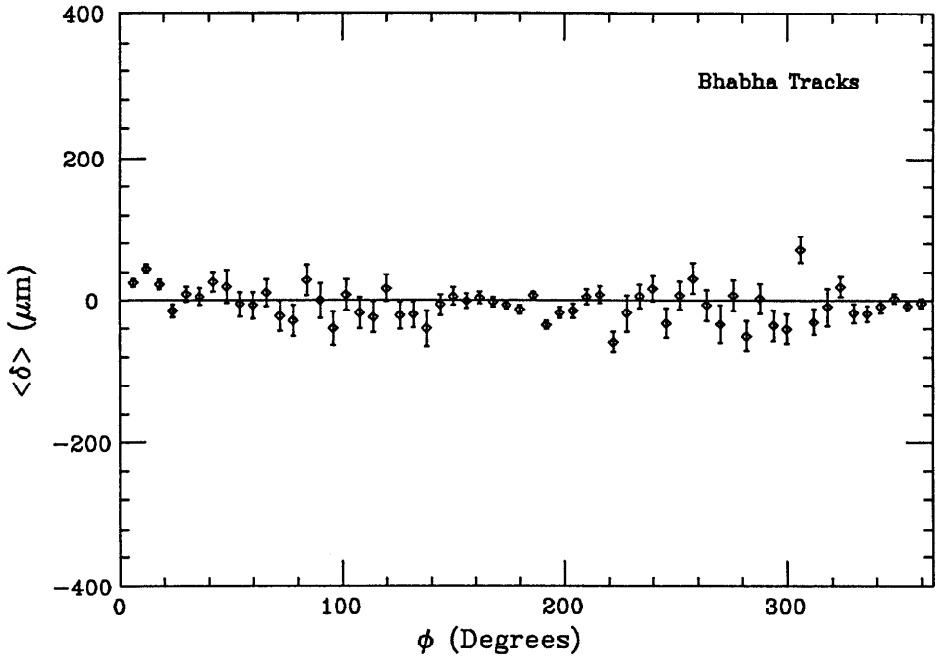

Figure 4.7: Mean impact parameter versus azimuthal angle. The variation in the sizes of the error bars is due to the beam spread.

distributions of Bhabha impact parameters for horizontal and vertical tracks, respectively. These distributions have widths given by the quadrature sum of the beam size and the extrapolated track resolution. In Figure 4.8, the distributions of impact parameters for horizontal and vertical Bhabha tracks are shown for data taken in the second half of 1983-84. The widths of the distributions in Figure 4.8 a and Figure 4.8 b are $112 \pm 3\,\mu$m and $438 \pm 11\,\mu$m, respectively. Accounting for the chamber resolution, these widths yield a vertical beam size of $76 \pm 5\,\mu$m and a horizontal size of $430 \pm 17\,\mu$m. The beam sizes are measured with the data divided up into several sets, as listed in Table 4.1. Other groups at PEP report similar estimates for the beam sizes [90-92].

The numbers presented for the beam sizes in Table 4.1 are different than those given in Ref. 58 and Ref. 93. The numbers in these references were obtained using Bhabha events in those runs in which a D^0 and D^+ candidate was found. Significantly more D's were found in the early data (1981-1982) than later on.†

† The momentum resolution in the early data was twice as good as later on due to the higher magnetic field.

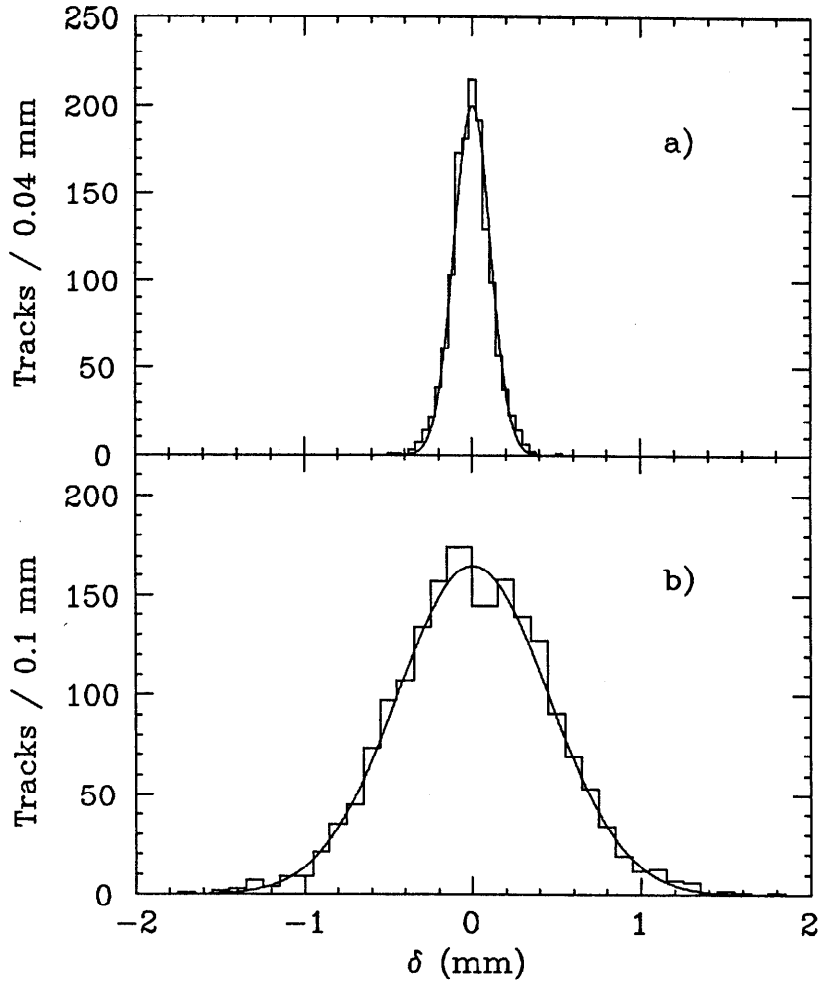

Figure 4.8: Impact parameters for horizontal and vertical Bhabhas. Tracks used lie within 3° of the x and y axes. The curves correspond to Gaussian fits to the data.

Table 4.1: PEP beam sizes.

Years	Run Numbers	σ_y (μm)	σ_x (μm)
1981 - 1982	8068 - 9099	62 ± 6	463 ± 21
1982 - 1983	9099 - 10122	84 ± 7	437 ± 22
	10123 - 11108	69 ± 5	395 ± 16
	11109 - 11472	61 ± 6	360 ± 18
1983 - 1984	11473 - 12400	79 ± 6	456 ± 21
	12401 - 13311	76 ± 5	430 ± 17

4.5 Study of Tracks in Hadronic Events

The Mark II Vertex Chamber has a double track resolution of $\sim$ 5mm,* approximately equal to the VC cell size. With the measurement points in the first layer of the VC at an average radius of 11 cm, this double track resolution translates into an angular resolution of 45 mr. In hadronic events at PEP energies, the average angular separation between a charged track and its nearest neighbor is $\sim$ 160 mr, but about one quarter of the tracks have another track within 50 mr. Therefore, the density of tracks in typical hadronic events often reaches the maximum density in which the Vertex Chamber can efficiently reconstruct tracks. A loss in tracking efficiency in a high density environment is expected. Since the Monte Carlo is able to simulate much of this efficiency loss, only the difference between the tracking efficiency in the data and in the Monte Carlo is of interest.

In this analysis, however, the systematic error in the lifetime measurement due to the difference in tracking efficiency between the data and Monte Carlo is small in comparison with the uncertainty in the shape of the resolution function. Therefore, our main concern about tracking in a dense environment is not the track *efficiency*, but rather the *quality* of reconstuction. The bulk of this section is devoted to understanding the tracking resolution in the Mark II Vertex Chamber for hadronic events. We will see that the position resolution for tracks in hadronic events is degraded by 25 % from that observed for isolated tracks. This degradation is largely due to electronic cross-talk in the VC pre-amplifiers and although it cannot be eliminated, it can be corrected for. At the end of this section, we return to the question of track efficiency in hadronic events.

4.5.1 *Hadronic track* χ^2

The VC χ^2 distribution for tracks in hadronic events is shown in Figure 4.9. There is a large disagreement between the χ^2 distribution observed in the data and the expected distribution. "The disagreement is embarrassing" [55].

---

* The double track resolution defined here is the minimum distance two tracks must be separated so that they are both resolved with 90 % efficiency. The value of 5 mm is determined from a sample of τ three prong decays.

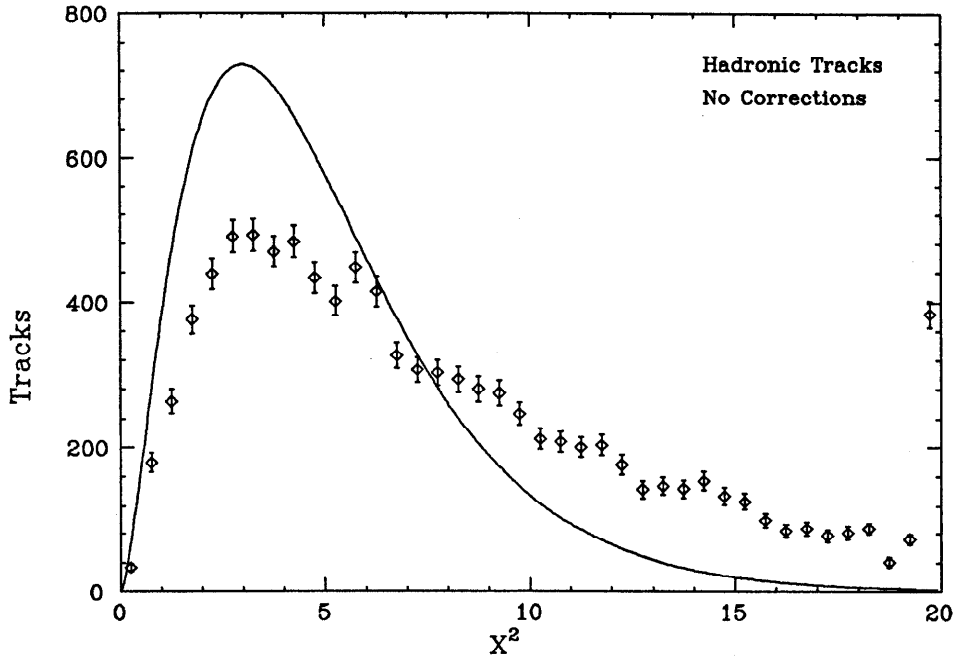

Figure 4.9: Track χ^2 distribution for hadronic events. Tracks are required to have seven hits in the VC. No time-slewing corrections are applied. The curve drawn is the expected χ^2 distribution for five degrees of freedom.

The following possible causes of the resolution degradation have been studied:

- Splash: Synchrotron radiation or excessive scattering can cause splash (many hits with the same time) in the VC. A program which finds splash was written that looked for pileups of hits in the Vertex Chamber with similar times and locations. This routine found that less than 1 % of the hits used on tracks were associated with splash.

  Random noise hits in the VC and/or DC can lead to tracking problems. For example, noise hits in the Drift Chamber can produce "ghost" tracks in the Vertex Chamber. Although the majority of events have few extra hits, it was found that even these events show considerable resolution degradation. Therefore, splash or noise hits cannot explain the degradation in resolution.
- Pattern Recognition: A number of potential pattern recognition problems exist when tracks get close to one another. Hits can be dropped from tracks or assigned to the wrong track. For short drift times, the ambiguity of a hit can be mistaken. In principle, most of the serious pattern recognition problems that are not associated with noise should be evident in the Monte Carlo. Yet

the track χ^2 distribution in the Monte Carlo shows excellent agreement with the expected distribution, leading to the conclusion that pattern recognition problems are insufficient to explain the degradation observed in the data.

- Cross-talk: It is possible to have cross-talk in the electronics or in the chamber itself (i.e. ionization from one cell leaking into an adjacent cell). The chamber cross-talk is expected to be small from electrostatic studies, and the pre-amplifier cross-talk was measured on the bench to be less than 1%. In order to check the amount of cross-talk, the distribution of time differences between adjacent hits in the VC was examined. This distribution should be triangular and centered on zero if no cross-talk existed.* A pile-up of events at zero time difference would be evidence for large cross-talk. No such evidence was observed, leading to the conclusion that cross-talk (of the type in which an adjacent wire is caused to fire) is not the cause of resolution degradation.

There is, however, a type of cross-talk somewhat more subtle than the usual one discussed above. Imagine two adjacent wires both having real hits on them (i.e. hits caused by the passage of a charged track). If a certain amount of capacitive or inductive coupling exists between the signal on one wire and that on the other wire, it is possible for the early hit to cause time *slewing* of the later hit. The slewing might not fire the wire with the later arriving time, but cause its time to be shifted. This type of cross-talk could cause significant degradation in the resolution of the slewed time without causing that time to be dropped from the fit. To explore the possibility of slewing effects, individual wire residual distributions were studied in detail.

4.5.2 *The time-slewing effect*

The usefulness of wire residual distributions was demonstrated in Section 4.2. In particular, the inclusive distribution of $\frac{R}{\sigma}$ (see Eqn. 4.2) for all hits is a good indicator of bias in the determination of residuals. This distribution for hits on Bhabha tracks has a mean centered on zero and a width consistent with one. The mean is also flat as a function of drift time.

* The drift time spectrum is essentially a uniform distribution. The difference between two uniform distributions is a triangular one.

In Figure 4.10, the mean of the $\frac{R}{\sigma}$ distribution is shown as a function of drift time for hits on tracks in hadronic events. Figure 4.10 demonstrates a dramatic systematic effect. The mean of the $\frac{R}{\sigma}$ distribution is negative; on the average , hits on hadronic tracks are systematically retarded so that their times predict a distance larger than the track fit would like. The magnitude of this effect increases for longer drift times, indicating that earlier times from adjacent cells are the likely cause of the problem.

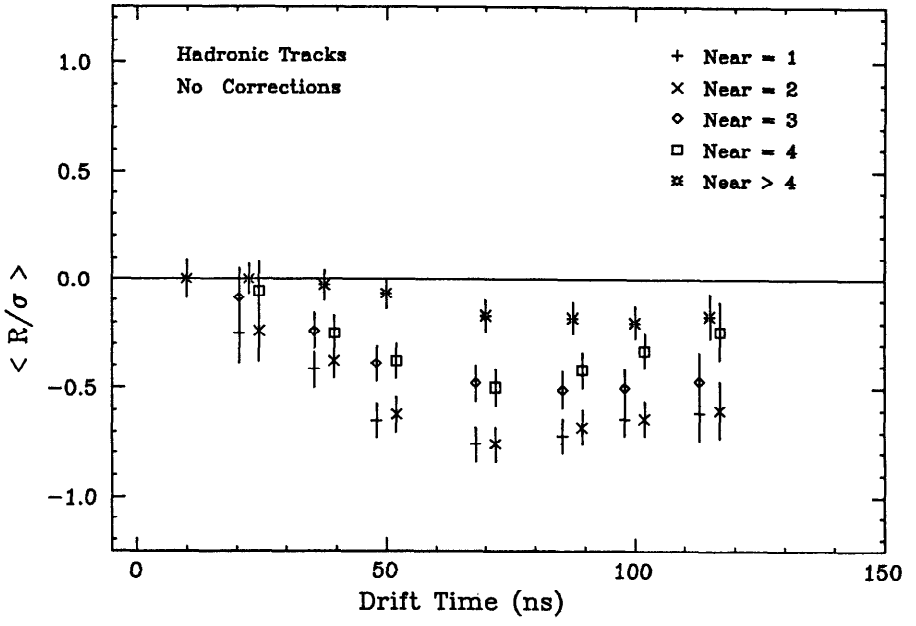

Figure 4.10: Mean of residual/error distribution without fixes. The mean of the $\frac{R}{\sigma}$ distribution for hits on hadronic tracks is shown as a function of the hit drift time. The parameter NEAR is defined in the text.

We define a parameter NEAR in the following manner:

NEAR = 1, if there is at least one hit with an earlier time within one VC cell

= 2, if there is at least one hit with an earlier time within two cells, but none within one cell

= 3, if there is at least one hit with an earlier time within three cells, but none within two cells

= 4, if there is at least one hit with an earlier time within four cells, but none within three cells

> 4, all other occurrences.

Note that a hit can have many neighboring times and still be classified as NEAR > 4, as long as all the neighboring times within four VC cells occur later in time.*

The systematic bias observed in Figure 4.10 is more pronounced for lower NEAR values. This fact demonstrates that the bias is strongly correlated with the presence of early neighboring hits. The width of the $\frac{R}{\sigma}$ distribution also illustrates the correlation between the bias and nearby times. This width is equal to 1.4 for hits with NEAR=1, but falls to a value close to 1.0 for hits with NEAR>4.

Figure 4.11 provides final proof that the systematic bias observed in the wire residual/error distribution is caused by adjacent early times. This figure shows the mean of the $\frac{R}{\sigma}$ distribution plotted as a function of the time difference between neighboring hits. Negative time differences correspond to those hits having a neighbor with an earlier time and vice-versa.

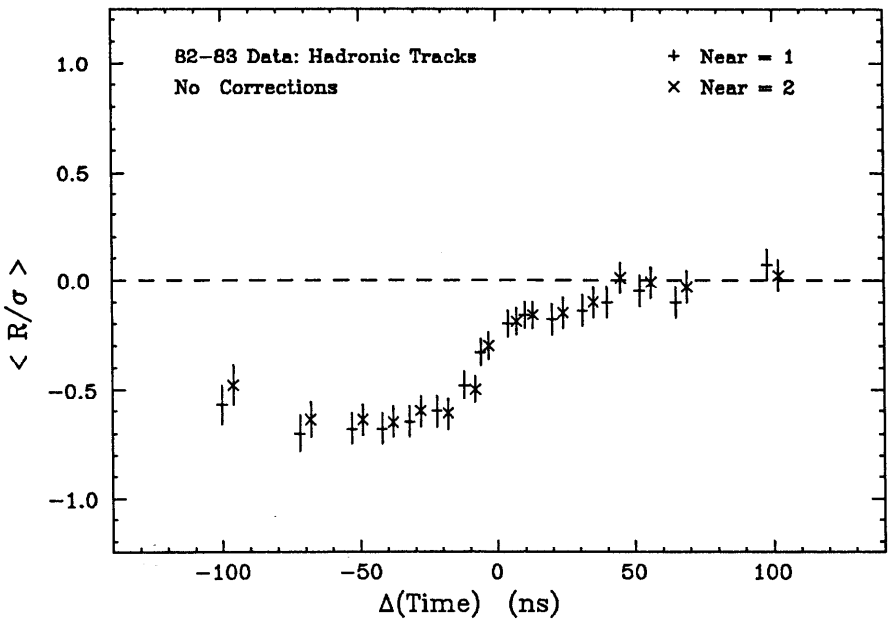

Figure 4.11: Mean of residual/error distribution versus time difference. The mean of the $\frac{R}{\sigma}$ distribution for hits on hadronic tracks is shown as a function of the time difference between neighboring hits. The parameter NEAR and the sign convention for the time difference are described in the text.

* Another point is that a neighboring time is defined as one that occurs *in the same layer*. No time-slewing is observed between VC layers. Since the VC electronics readout is segmented into layers, the results based on NEAR indicate that the problems are likely due to *electronic* cross-talk, and not chamber cross-talk.

The data points in Figure 4.11 lie on a curve that is remarkably similar to a step function. The bias in the mean $\frac{R}{\sigma}$ is large and approximately constant for hits with an early neighbor. This bias is greatly reduced for hits having a neighbor with a later time.

4.5.3 *Probable cause of the time-slewing effect*

As discussed earlier, there are indications that the observed time-slewing effect is due to electronic coupling. For a number of reasons, it was suspected that the coupling took place at the pre-amplifier stage. There were oscillation problems in the metal cage that housed the pre-amps and the board density was rather high in this cage.

To investigate coupling effects in the pre-amps, a test circuit was set up to simulate several parallel channels of readout. The time-slewing effect was observed in this set-up. In particular, time-slewing only occurred for hits having an earlier nearby hit when the transformer pre-amps (Figure 2.7) were used. The magnitude of the slewing observed in the bench test was sufficient to explain the resolution degradation in the data. A likely location for slewing is in the PE-8302 integrated circuit on the transformer pre-amp boards. This IC consists of four individual transformer circuits in a single 16 pin DIP package. The transformers share a common core, allowing for inductive coupling. Another possible cause of coupling is poor placement of ground returns. Without extensive lab work, it is impossible to determine exactly where to lay the blame.

4.5.4 *The fix to the time-slewing effect*

The question now arises as to how to correct for the bias observed in the $\frac{R}{\sigma}$ distribution, regardless of its origin. In principle, it would be nice to know on a hit-by-hit basis exactly how much to correct for. The $\frac{R}{\sigma}$ distribution consists of an average of many hits, each which may be affected by the coupling in varying amounts. This distribution is quite consistent, however, with a single offset Gaussian; therefore, it is possible to treat the coupling in an average sense.

The fix to the time-slewing problem consists of the following recipe. All hits are first categorized by NEAR. For each hit, an offset correction is applied to the space-time relation, and the expected error on the hit is adjusted. These corrections

depend on the value of NEAR. The largest offset and error corrections are 65 μm and 55 %, respectively, made to hits with NEAR=1 or 2 ($\sim$ 20 % of all hits).

In Figure 4.12, the mean of the $\frac{R}{\sigma}$ distribution versus drift distance is shown for various values of NEAR after time-slewing corrections have been applied. The improvement over Figure 4.10 is obvious. The width of the $\frac{R}{\sigma}$ distribution shows similar improvement as a result of the time-slewing corrections.

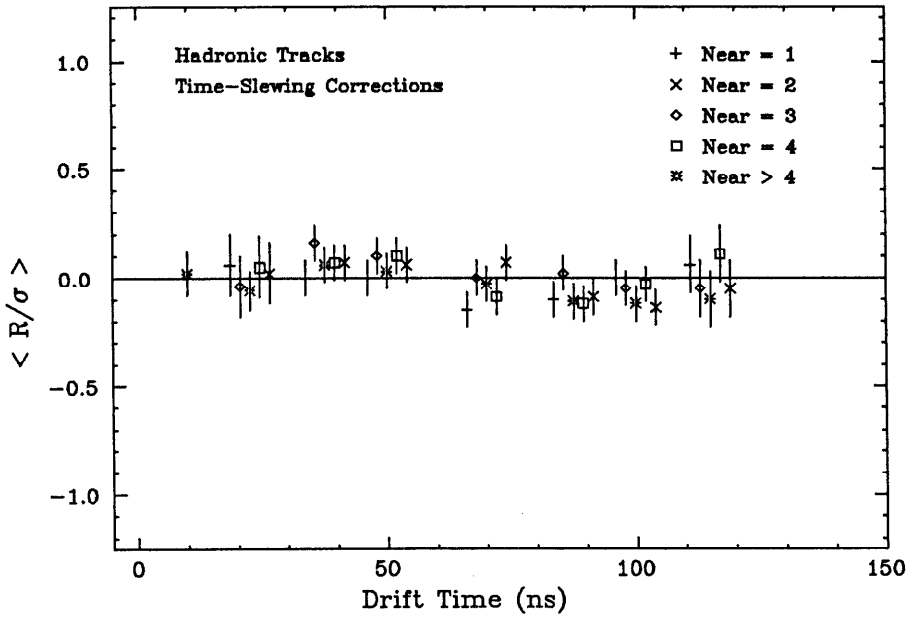

Figure 4.12: Mean of residual/error distribution with fixes. The mean of the $\frac{R}{\sigma}$ distribution for hits on hadronic tracks is shown as a function of drift time. Time-slewing corrections are applied to the hits. The parameter NEAR is described in the text.

In summary, the problem of resolution degradation in the Mark II Vertex Chamber has been found to be largely due to electronic time-slewing. This effect was isolated by looking at the signed $\frac{R}{\sigma}$ distributions. The software fix for this degradation identifies those hits on a track that are likely to have been affected and corrects their times and errors. As shown in Figure 4.13, the χ^2 distribution for tracks in hadronic events agrees reasonably with the expected distribution.

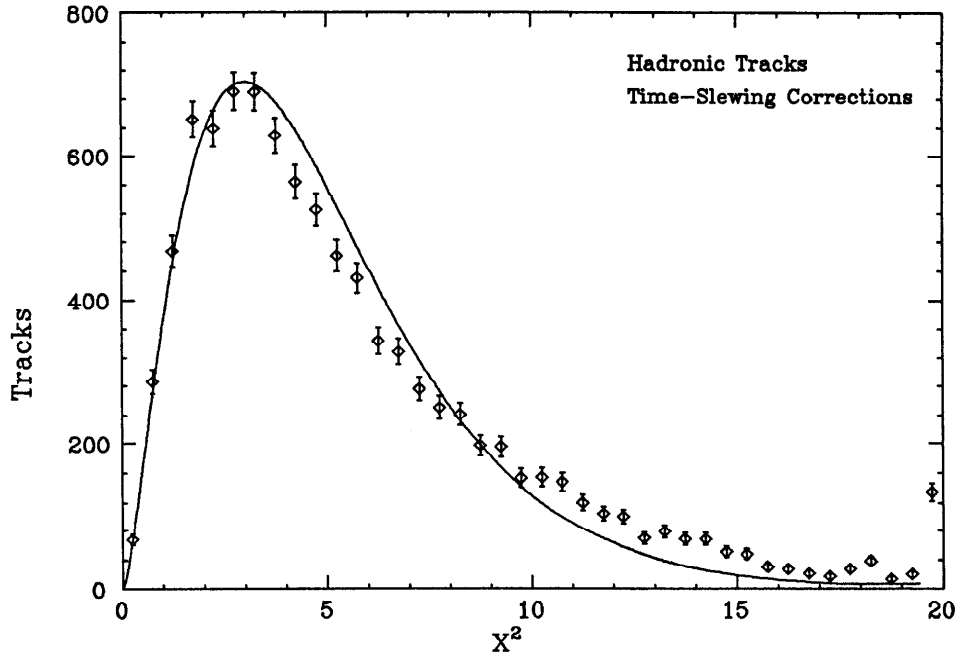

Figure 4.13: Track χ^2 distribution for hadronic events after correction. Tracks are required to have seven hits in the VC. Time-slewing corrections are applied to the hits. The curve drawn is the expected χ^2 distribution for five degrees of freedom.

4.6 Track Quality Cuts

As shown in Figure 3.1, the average charged particle multiplicity at PEP is nearly 13 for events enriched in charm and bottom production. Due to imperfect detector response (typically caused by high track density) and other problems (e.g. scattering, radiation), not all of the charged tracks in an event are suitable for use in a precision lifetime measurement. For this analysis, the most powerful cuts that are used to ensure quality are those that require a reasonable track χ^2 and a minimum number of hits in the Vertex Chamber. We now define general track quality cuts. These cuts will be used later in Chapter 7 to determine those tracks in an event appropriate to use in the lifetime measurement.

We first require events to pass hadronic and jet analysis cuts (these cuts are described in Chapter 6). We remove very poor tracks by requiring to have at least 9 (out of 23) hits in the VC and DC combined and a momentum of at least 200 MeV/c; these cuts are quite minimal. A quality track is then defined as one that

passes the following battery of cuts:

1. The distance of closest approach in z to the average beam position must be less than 5 cm.
2. The distance of closest approach in xy to the average beam position must be less than 5 mm.
3. Track $p_{xy} > 300$ MeV/c and $p < 16$ GeV/c.
4. The track must have at least 12 hits in the VC and DC combined.
5. The track χ^2 per DOF calculated in the VC and DC together must be less than 5.
6. The probability of the χ^2 fit in the VC alone must be greater than 0.1 %. †.
7. The track must have at least two inner and one outer VC hits.

The first two cuts remove tracks that probably do not come from the interaction point.* The third cut removes tracks that have very low momenta (and therefore a large amount of multiple scattering) and tracks whose momenta are likely to have been mis-measured. The remaining four cuts are designed to ensure quality reconstruction of the track in the drift chambers.

In Table 4.2, the cumulative percentages of tracks passing the quality cuts are shown for tracks in the data and Monte Carlo. From this comparison, we see that cuts 5 and 6 have a significantly greater effect on the data than on the Monte Carlo. (This same conclusion is drawn if the cuts are applied in another order from that listed above). In Figure 4.14, the normalized probability distribution of the VC track χ^2 fit is shown.

The bulk of the VC track χ^2 distribution looks reasonable, but there are simply more tracks at large χ^2 in the data than in the Monte Carlo. All studies indicate that the tracks in the tail are simply ones of poor quality. Therefore, although the track quality cuts lead to somewhat lower efficiencies in the data than in the Monte Carlo, the tracks passing these cuts can be considered well reconstructed.

---

† The fit probability is defined as the integral of the χ^2 distribution out to the observed χ^2 value (for the correct DOF). Probability values from an ideal χ^2 distribution are distributed uniformly on the interval (0,1). For small DOF, it is preferable to cut on the probability directly rather than the χ^2 /DOF value; a constant χ^2 /DOF cut for different DOFs corresponds to markedly different probability cuts.

* We will see in Chapter 9 that essentially no systematic error is introduced from the second cut. The average distance of closest approach for leptons from B hadron decay is measured to be $\sim$ 0.14 mm, considerably smaller than the 5 mm cut.

Table 4.2: Track quality cuts. The cumulative percentages of tracks in hadronic events passing the quality cuts is shown.

Cut #	DATA (% passing)	MC (% passing)
1	92.3	93.1
2	89.7	89.9
3	86.5	87.4
4	83.9	85.2
5	78.1	83.4
6	73.5	81.9
7	62.0	72.3

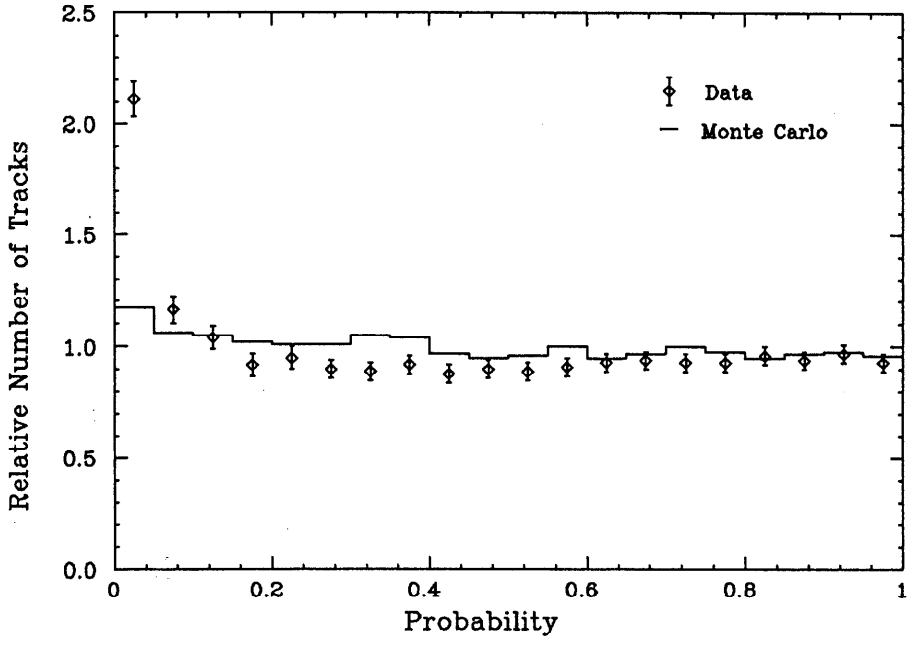

Figure 4.14: VC track χ^2 probability.

Lepton Identification

Electrons and muons can be distinguished from other charged particles by their characteristic interactions with matter. Electrons lose energy upon entering matter primarily by radiating photons through the bremsstrahlung process. These photons produce electron-positron pairs which then can radiate more photons. This cascade process continues, forming an electromagnetic shower of particles. The number of particles increases with increasing depth into the material, but the average particle energy decreases. The shower terminates when the particle energy reaches a critical value below which energy loss through ionization dominates. The scale of an electromagnetic shower in a given material is set by its radiation length X_0, defined as the mean free path length of electrons in the material.

The bremsstrahlung process of energy loss is suppressed for particles other than the electron because of their larger masses. Hadrons lose energy in material by interacting with the nuclei of the material via the strong interaction. This process produces secondary particles (mostly pions and nucleons) which continue to interact, resulting in a hadronic shower of particles. The scale of the hadronic shower is set by the nuclear absorption length λ of the material. For materials with high Z values, the nuclear absorption length is typically much larger than the corresponding radiation length (e.g. in lead, $\lambda = 10.3$ cm and $X_0 = 0.56$ cm.) Electrons can therefore be expected to deposit almost all their energies in an appropriately thick calorimeter made of such material, while hadrons of the same momenta will lose only a small fraction of their energy. This expectation is

the underlying principle behind electron identification in the Mark II calorimeter. Hadrons sometimes resemble electrons because of shower fluctuations (especially in the number of secondary π^0's produced) or because of the presence of overlapping charged tracks and photons.

Muons do not interact strongly and have masses too large to produce bremsstrahlung photons. Muons lose energy in material primarily through uniform ionization. Since the rate of energy loss for muons is much lower than that for hadrons, they can be distinguished by their ability to penetrate material. The Mark II muon system consists of steel absorber designed to stop most hadrons, while allowing muons above a given momentum to penetrate.

The hardware details of the detector are outlined in Chapter 2. Here we discuss how information from the detector is used to identify leptons. The algorithms for electron and muon identification are presented. The identification efficiencies are tabulated, along with the hadron mis-identification, punchthrough, and decay probabilities. The probabilities for hadron mis-identification and punchthrough are derived in part from a previous study of leptons in the Mark II detector [94]. These probabilities have been checked with samples of known hadrons in the data [95].

In this chapter, and in the following one, tables are presented for given quantities divided into bins of momentum (p) and transverse momentum (p_t) measured relative to the thrust axis. In these tables, the units for (p, p_t) are GeV/c; the (p, p_t) values correspond to the low edge of each bin and the last bins contain all overflows.

5.1 Electron Identification

5.1.1 Identification algorithm

Electrons are identified in the lead-liquid Argon (LA) calorimeter. The calorimeter is described in Section 2.8. As shown in Figure 2.11, each calorimeter module consists of 18 layers of lead strips that are ganged into six distinct readout layers.

Identification is done by comparing the amount of energy a track deposits in the calorimeter with the momentum of the track measured in the Drift Chamber. Charged tracks in the DC are projected into the calorimeter and the energy E_{LA}

within a search region around the track is determined. Electrons have values for the ratio E_{LA}/p close to one, while most hadrons have much smaller values. Unfortunately, hadrons can be mistaken for electrons when other charged tracks or photons overlap the hadron track in the calorimeter. The effects of overlap are reduced by using only the first half of the calorimeter (the first four readout layers), by choosing a small search region around the extrapolated track, and by requiring the energies in each of the LA readout layers to be consistent with the amount of energy expected from an electron shower.

The width of the search region is calculated using the following formula:

$$W_{Search} = W_{Shower} + W_{Gang} \times |tan(\delta)| \ . \tag{5.1}$$

Here W_{Shower} is chosen to be the typical width of an electromagnetic shower ($\sim$ 3 cm), W_{Gang} accounts for the added width resulting from the separation between the front and back sections of a ganged layer, and δ is the angle between the extrapolated track and the normal to the layer. The values for W_{Shower} and W_{Gang} for the various readout layers are given in Table 5.1.

Table 5.1: Parameters used in the electron identification algorithm. The parameters are described in the text. The F1, F2, and T1 layers have strip widths of 3.8 cm; the U layer has a strip width of 5.4 cm.

Layer	W_{Shower}(cm)	W_{Gang}(cm)	α
F1,F2	2.9	2.9	0.14
T1	2.9	5.7	0.10
U	3.8	8.1	0.10

For each charged track W_{search} is calculated. The energies in the F1, F2, T1, and U readout layers within that search region are assigned to the track. If the center of a strip for a given layer lies within the search region, the energy of that strip is included. A variable called E_{min}/p is then calculated for each track. E_{min}/p is defined as the minimum of the following four quantities:

- $\dfrac{E_{F1}+E_{F2}}{\alpha_F \cdot p}$,

- $\dfrac{E_{T1}}{\alpha_T \cdot p}$,
- $\dfrac{E_U}{\alpha_U \cdot p}$, and
- $\dfrac{E_{F1}+E_{F2}+E_{T1}+E_U}{\alpha_{Fr} \cdot p}$.

Here p is the momentum of the track and E_{F1} is the energy in the F1 layer (similarly for the F2,T1, and U layers). The α parameters account for the fact that showers deposit only a fraction of their energy in each layer. The values for these parameters are given in Table 5.1 (except for α_{Fr} which is 0.50 for p <4 GeV/c and 0.40 for p >4 GeV/c). The values are chosen so that most electrons have values of E_{min}/p greater than one.*

In Figure 5.1, the values of E_{min}/p for samples of known electrons and pions are shown. Clearly, as E_{min}/p increases, the probability for a pion track being mis-identified as an electron decreases, but so too does the electron identification efficiency.

In this analysis, electron candidates are defined as those tracks within the LA fiducial volume satisfying:

$$E_{min}/p \ > 1.1 \ \text{(Electron criterion)} \ . \tag{5.2}$$

5.1.2 Identification efficiency

The cuts used to define the fiducial region of the LA calorimeter are discussed in Section 2.8. This region covers ~ 65 % of the solid angle. The efficiency for detecting electrons in collinear Bhabha events within the fiducial region is better than 98 %. The identification efficiency for electrons with lower momenta is determined from radiative Bhabha events and two-photon events of the type $e^+e^- \rightarrow e^+e^-e^+e^-$. These two types of events together constitute a clean sample of electrons in the data covering the entire momentum range of interest. The selection criteria for isolating this sample of events and the method of determining the efficiency in an unbiased way are described in Ref. 89.

The electron identification efficiency determined from this sample is given in

* Because of this (somewhat arbitrary) definition, E_{min}/p is typically larger than the simple ratio of the track energy divided by momentum.

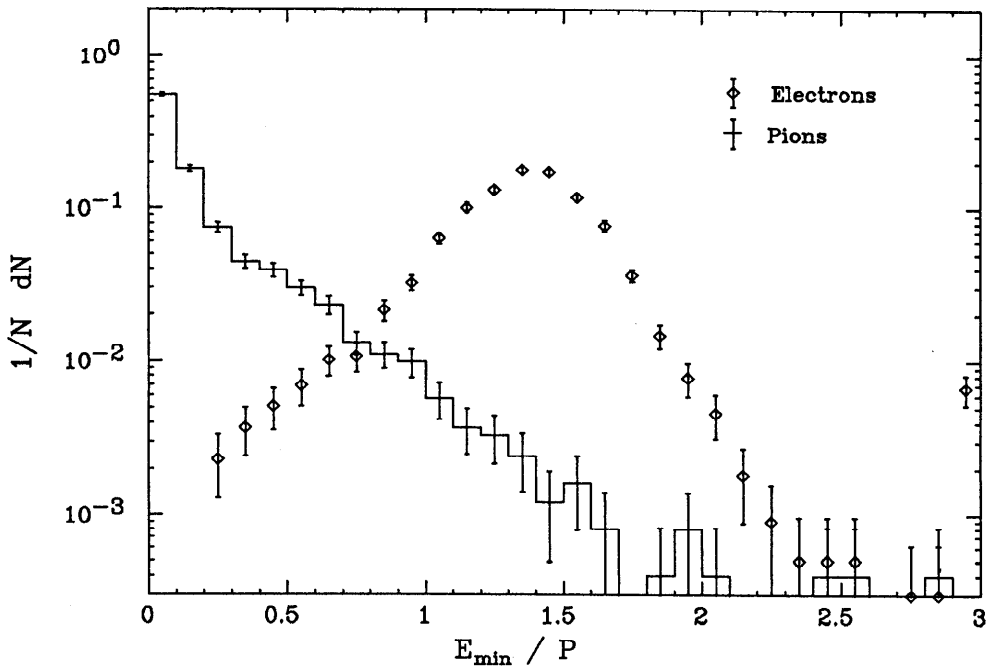

Figure 5.1: E_{min}/p values for electrons and pions. Tracks in this plot are required to have momenta greater than 2 GeV/c. The electrons tracks are isolated from a sample of two-photon events of the type $e^+e^- \rightarrow e^+e^-e^+e^-$. The pion tracks are isolated from a sample of $\tau \rightarrow \pi\pi\pi\nu$ decays.

Table 5.2, as a function of momentum. The detection efficiency in the Monte Carlo is also tabulated; it is typically several percent higher than that for the data.

5.1.3 *Hadron mis-identification*

The dominant source of background to the prompt electron signal comes from mis-identification of charged hadrons (mostly pions). The probability for mis-identifying isolated hadron tracks as electrons has been studied using a sample of known pions from ψ decay at SPEAR and from a pion test beam run. For tracks in a denser environment, the overlap of other charged tracks and photons causes a significantly higher fraction of pions to be mis-identified.

A study was made of track overlap that took advantage of the back-to-back nature of hadronic events at PEP energies [94]. In this study, candidate electron tracks in one jet were "flipped" by 180° so that they projected into the opposite jet of the event. A search was then made in the calorimeter to determine the energy associated with the projected track. This energy should be the same as the amount expected from track overlap effects (except that one must correct for the fact that

Table 5.2: Electron identification efficiency. The numbers in this table have errors of approximately 3 %.

	Efficiency	
P (GeV/c)	Data	MC
2.0	0.88	0.90
2.5	0.89	0.92
3.0	0.90	0.94
3.5	0.90	0.94
4.0	0.91	0.94
4.5	0.91	0.94
5.0	0.91	0.94
5.5	0.91	0.95
6.0	0.92	0.95

there is a somewhat higher energy density in the opposite jet than in the original jet minus the candidate track).

From the study of track overlap effects, and from a sample of isolated pions, the probabilities for hadron mis-identification were determined. These probabilities are given in Table 5.3, as a function of (p, p_t) , for the electron criterion given in Eqn. 5.2. Note that the mis-identification probabilities are larger at lower values of momentum and transverse momentum.

The hadron mis-identification probability can be checked using a sample of known pions in the PEP data. In particular, the E_{min}/p values for pions from the decays $K_s^0 \rightarrow \pi\pi$ and $\tau \rightarrow \pi\pi\pi\nu$ have been studied.* The mis-identification values obtained from this study agree with those presented in Table 5.3, within errors.

5.1.4 Electrons from conversions and Dalitz decays

In addition to the background from mis-identified hadrons, there is a smaller source of background to the prompt electron signal coming from photon conversions and Dalitz π^0 decays.

Photon conversions largely occur at the beam pipe or at the material between the Vertex Chamber and Drift Chamber. Because this analysis requires electron

* The selection criteria for isolating a sample of pions from the K_s^0 decay mode are discussed in Ref. 96, while those used to tag the three pion τ decay are discussed in Ref. 89.

Table 5.3: Hadron mis-identification probabilities (in percent). The numbers in this table have systematic uncertainties of approximately 40 %.

$p \backslash pt$	0.00	0.25	0.50	0.75	1.00	1.25	1.50
2.0	1.6	1.6	0.8	0.8	0.7	0.7	0.7
2.5	1.3	1.3	0.8	0.8	0.7	0.7	0.7
3.0	1.1	1.1	0.6	0.6	0.5	0.5	0.5
3.5	0.9	0.9	0.6	0.6	0.5	0.5	0.5
4.0	0.8	0.8	0.5	0.5	0.4	0.4	0.4
4.5	0.7	0.7	0.5	0.5	0.4	0.4	0.4
5.0	0.7	0.7	0.5	0.5	0.4	0.4	0.4
5.5	0.7	0.7	0.5	0.5	0.4	0.4	0.4
6.0	0.6	0.6	0.4	0.4	0.3	0.3	0.3

candidates to have hits in the Vertex Chamber, almost all conversions between the VC and DC are eliminated. Many of the remaining beampipe conversions are removed by a pair-finding routine [94]. This routine matches an electron candidate with every oppositely charged track in the event, and determines if the pair of tracks were likely to have come from a conversion. The parameters used for the pair-finder in this analysis are the same as those given in Ref. 89. Monte-Carlo studies have shown that the pair-finder eliminates more than 70 % of real conversions with very small chance for error.

The Dalitz decay $\pi^0 \rightarrow \gamma e^+ e^-$ constitutes a relatively minor background because of the small branching ratio for the decay (1.2 %). In addition, many of the Dalitz decays are removed by the pair-finding routine.

The remaining background to the electron signal in hadronic events from conversions and Dalitz decays is determined from the Monte Carlo. As discussed in Section 4.3, the amount of scattering at the beampipe has been measured in the data, and has been found to agree with the amount assumed in the Monte-Carlo. The expected background to the inclusive electron signal from conversions and decays is given in Table 5.4, for the electron criterion given in Eqn. 5.2.

Table 5.4: Expected electron background from conversions and Dalitz decays. The numbers in this table are determined from a large sample of hadronic Monte Carlo events normalized to the number of hadronic events in the data. The numbers have systematic uncertainties of approximately 20 %.

$p \backslash p_t$	0.00	0.25	0.50	0.75	1.00	1.25	1.50
2.0	15.7	12.1	6.6	1.8	0.8	0.5	1.1
2.5	11.7	5.8	4.7	2.0	0.8	0.6	0.8
3.0	5.2	3.8	2.8	1.4	0.7	0.3	0.6
3.5	1.4	2.8	2.6	1.2	0.6	0.3	0.5
4.0	1.2	2.6	2.0	0.8	0.4	0.2	0.5
4.5	1.1	2.3	1.6	0.6	0.3	0.2	0.3
5.0	0.8	2.0	1.5	0.5	0.2	0.1	0.2
5.5	0.6	1.7	1.2	0.4	0.2	0.1	0.2
6.0	1.6	2.4	1.5	0.8	0.4	0.2	0.6

5.2 Muon Identification

5.2.1 Identification algorithm

Muons are identified in the Mark II detector by associating hits in the muon proportional tube layers with tracks in the Drift Chamber. The muon system is described in Section 2.9. Each wall of the muon system consists of 4 layers of alternating hadron absorber and proportional tubes. Each charged track in the DC is projected into the muon system and a search is made around the projected track for proportional tube hits. In this analysis, the search region is set to two times the rms error of track extrapolation. This error is the extrapolated Drift Chamber tracking error (typically $\sim$ 2.5 cm), combined in quadrature with expected error due to multiple Coulomb scattering in the detector elements preceding the given tube layer.

The amount of multiple Coulomb scattering for a particle incident on a piece of material depends on the particle momentum, as well as the material thickness and composition. The rms scattering angle can be written in the Gaussian approximation as [97]:

$$\theta = \frac{21}{p\beta} \cdot \sqrt{\frac{t}{X_0}} \quad , \tag{5.3}$$

where p is the momentum (in MeV/c) and β the velocity of the incident particle. The material thickness and radiation length are given by t and X_0, respectively.

In the Mark II , the detector elements preceding the proportional tubes are the magnet coil (1.4 X_0), the LA calorimeter (14.4 X_0), and hadron absorbers (13.0 X_0/layer). The scattering effects of each element are independent, therefore their contributions can be added in quadrature. In a given layer of the muon system, the mean-squared position error projected in one dimension* due to multiple scattering can be expressed as [98]:

$$\sigma_x^2 = \frac{1}{2}\sum_i \theta_i^2 \cdot \left(\frac{t_i^2}{3} + t_i d_i + d_i^2\right) , \tag{5.4}$$

where d_i is the distance following the element i to the given layer, and t_i and θ_i are the thickness and rms scattering angle of the element i, respectively. The typical position error for a 2 GeV muon due to multiple scattering is 5 cm at the first layer of the muon system and 10 cm at the fourth layer.

For each track, a variable MUSTAT is formed. This variable corresponds to the bit pattern of the muon system layers having hits associated with the given track. (For example, a track with associated hits in the first three layers has MUSTAT=7.) In this analysis, muon candidates are defined as those tracks within the muon system fiducial region (discussed below) satisfying:

$$\text{MUSTAT} = 15 \ (\text{Muon criterion}) , \tag{5.5}$$

i.e. having associated hits in all four of the muon layers.

5.2.2 *Identification efficiency*

Since muons are required to have hits in all four proportional tube layers, the fiducial region of the muon system is defined by the acceptance of the outermost tube layer in each wall. These layers cover $\sim 45\,\%$ of the solid angle. In addition, muon candidates are required to have sufficient momenta to penetrate to the fourth layer. For tracks at normal incidence to the absorber planes, this criterion effectively imposes a 1.8 GeV/c momentum cut.

* In a given layer, the proportional tubes measure only one coordinate.

Muons can fail to be detected because of proportional tube inefficiencies, range straggling (fluctuations in the DE/DX loss causing them not to reach the fourth layer), or because they multiple scatter by a large amount so that their hits lie outside of the 2σ search region. In addition, if a muon track is poorly reconstructed in the Drift Chamber, its extrapolation into the muon system can fail to lie within 2σ of the correct proportional tube hits. These effects are all incorporated into the simulation of the muon system. The detection efficiencies determined by the simulation are shown in Table 5.5 , along with the corresponding efficiencies in the data. These latter numbers are determined from $\mu^+\mu^-$ pairs produced from single and two-photon interactions.

Table 5.5: Muon identification efficiency. The numbers in this table have errors of approximately 3 %.

	Efficiency	
P (GeV/c)	Data	MC
2.0	0.78	0.79
2.5	0.79	0.81
3.0	0.80	0.83
3.5	0.82	0.85
4.0	0.84	0.87
4.5	0.86	0.89
5.0	0.88	0.91
5.5	0.89	0.92
6.0	0.90	0.93

5.2.3 Hadron punchthrough

Approximately half of the background to the prompt muon signal comes from hadron tracks that punchthrough to the muon system. In principle, reliable estimates for the amount of hadron punchthrough can be obtained from the study of clean sources of pions and kaons in the data. Unfortunately, because of insufficient statistics, this method is only useful as a cross-check.

Instead, the MUSTAT distribution for all tracks in hadronic events was studied making no assumption on the particle type [94]. This study used the fact that the

Mark II detector has four layers of muon readout. For momenta greater than 2 GeV/c, real muons tend to penetrate to the fourth layer with typically 85 % probability. Therefore, the ensemble of hits not associated with identified muons in the first three layers is largely made up of hits from punchthrough tracks and random noise, with a small contribution due to real muons. The amount of random noise was determined by looking at activity in the muon system in Bhabha events. A maximum likelihood fit was then made to the combined MUSTAT distribution for all tracks, accounting for the various contributions to this distribution. The free parameters in this fit were the hadron punchthrough probabilities to the first three layers. From these probabilities, an extrapolation was made to determine the punchthrough probabilities to the fourth layer, as given in Table 5.6.

Table 5.6: Hadron punchthrough probabilities (in percent). The numbers in this table have systematic uncertainties of approximately 40 %.

$p \backslash p_t$	0.00	0.25	0.50	0.75	1.00	1.25	1.50
2.0	0.28	0.28	0.28	0.28	0.22	0.22	0.22
2.5	0.28	0.28	0.28	0.28	0.24	0.24	0.24
3.0	0.29	0.29	0.29	0.29	0.25	0.25	0.25
3.5	0.30	0.30	0.30	0.30	0.27	0.27	0.27
4.0	0.32	0.32	0.32	0.32	0.28	0.28	0.28
4.5	0.34	0.34	0.34	0.34	0.30	0.30	0.30
5.0	0.36	0.36	0.36	0.36	0.32	0.32	0.32
5.5	0.38	0.38	0.38	0.38	0.36	0.36	0.36
6.0	0.45	0.45	0.45	0.45	0.43	0.43	0.43

There is a slight p_t dependence to the punchthrough probabilities because tracks with lower p_t are more likely to be in a denser tracking environment. As a result, these tracks are more likely to be associated with hits in the muon system from overlapping tracks.

As a check on the punchthrough probabilities given in Table 5.6, the MUSTAT distributions for clean pion and kaon tracks were studied. As discussed previously, a sample of pions can be obtained from the $\tau \to \pi\pi\pi\nu$ decay. A total of 1717 pion tracks with an average momentum of 4.2 GeV were found within the muon fiducial

volume. The number of tracks with MUSTAT=15 in this sample was found to be consistent with the number expected from punchthrough and decays in flight [95]. In addition, the tau pion data were used to measure the probabilities for punchthrough to the first, second, and third layers of the muon system. These probabilities are shown in Figure 5.2, plotted against the amount of material preceding a given muon layer. Using this figure, the probability for pion punchthrough to the fourth muon layer is extrapolated to be $0.25 \pm 0.12\,\%$. This number agrees with a value of $0.30\,\%$ given in Table 5.6, for a mean momentum of 4 GeV/c.

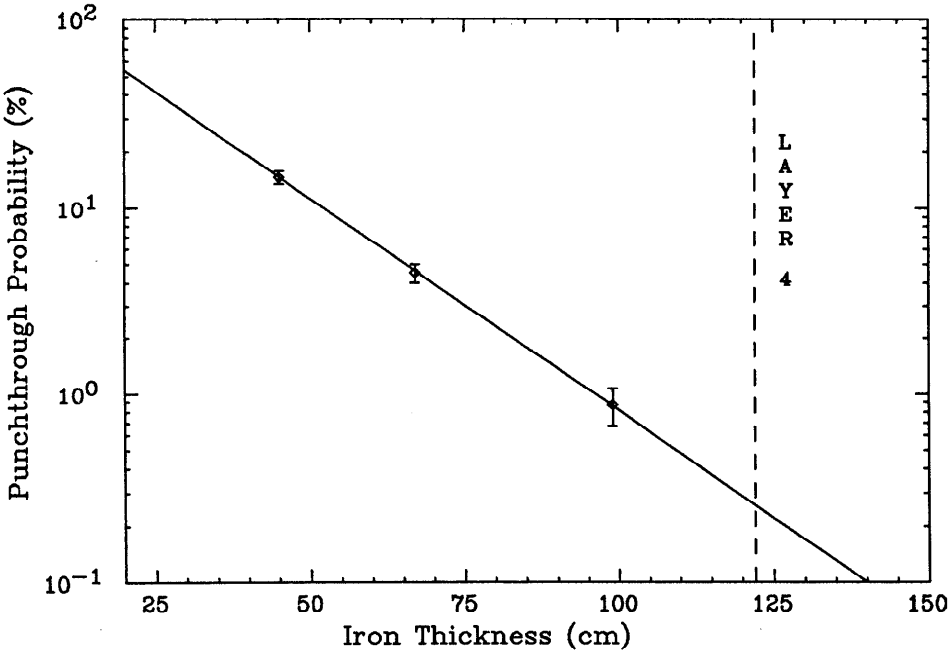

Figure 5.2: Hadron punchthrough probability versus iron thickness. Pion tracks from the decay $\tau \rightarrow \pi\pi\pi\nu$ are used to determine these probabilities.

In Ref. 94, there was some evidence that the punchthrough probability is larger for kaons than for pions.* To check this possibility, a sample of kaon tracks from D^0 decay was studied. As discussed in Ref. 95, within the statistics of this study, it was found that kaon punchthrough is not that much different from that for pions. Since the punchthrough probabilities were determined from a general sample of pion, kaon, and proton tracks, differences between the punchthrough probabilities

* Monte Carlo estimates based on cross section measurements predict kaon punchthrough to be significantly larger than that for pions [99].

of various particle type are insignificant in comparison with the 40 % systematic error assigned to the overall punchthrough probability.

5.2.4 Muons from decays

The second significant background to the prompt muon signal comes from muons produced from the decays of pions and kaons in flight. The amount of this background can only be estimated from the Monte Carlo. The process of producing a detected muon from parent (pion or kaon) decay can be divided into two separate parts: the first part being the parent decay probability and the second part being the fraction of decays yielding a detected muon. This fraction depends on a number of features of pion and kaon decay: for example, where the kink between the parent track and the daughter muon track is produced. This kink can cause the momentum of the detected track to be incorrect, depending on where in the Drift Chamber the decay took place.* If the kink is large enough, the track may fail to be reconstructed. In this analysis, the background estimation for muons from pion and kaon decay was done by two different methods for comparison purposes. These different methods provided very similar estimates.

In the first method, a count was made of the number of muons from decays detected from a large sample of Monte Carlo hadronic events. From the numbers of pions and kaons produced, the probabilities that a pion or kaon decayed to a reconstructed muon were determined. This technique assumed that the Monte Carlo accurately reproduces the details of hadron decay and track reconstruction and it suffered only from limited the statistics available.

The second method of estimating the decay background studied the two separate parts of the mechanism that produced muons from decays. The probability for a particle to decay inside the detector was calculated from the formula:

$$P(l) \;=\; 1 - e^{-l/\gamma\beta c\tau} \;=\; 1 - e^{-ml/pc\tau} \;, \qquad (5.6)$$

where P(l) is the probability for a decay within a distance l (1.6 m for a track normal to the beam axis), for a particle of mass m, lifetime τ, and momentum p.

* If the decay point of the parent track occurs early on in the Drift Chamber, the measured momentum of the detected track reflects that of the muon, while if it occurs near the outer radius of the Drift Chamber, the measured momentum reflects that of the parent.

Using this formula (and BR($\pi \rightarrow \mu\nu$) = 1.0 and BR($K \rightarrow \mu\nu$) = 0.64) , the pion and kaon decay probabilities in the Mark II detector were calculated. Because of its greater mass and shorter lifetime, kaons are approximately four times more likely to decay inside the detector than are pions.

With the decay probabilities in hand, large samples of pion and kaon decays were generated with the Monte Carlo. The number of muons from decays which were detected in the muon system was compared to the number of decays produced. This comparison was done as a function of the *reconstructed* momentum of the detected parent/muon track. It was found that the fraction of decaying pion tracks producing a reconstructed muon is 0.28, for a momentum of 2 GeV/c. This fraction rises to 0.50, for a momentum of 6 GeV/c. For kaons, these same fractions are 0.07 at a momentum of 2 GeV/c, rising to 0.14 at a momentum of 6 GeV/c. Kaons have a smaller fraction of tracks passing pattern recognition than pions because their decay produces a larger average kink angle. Based on the determined muon fractions, and the calculated decay probabilities (Eqn. 5.6), one can determine the overall probability that a pion or kaon track within the muon fiducial volume decays to a reconstructed muon. This probability is given in Table 5.7, as a function of the reconstructed track momentum.

Table 5.7: Probability of pion and kaon decay to a reconstructed muon. The numbers in this table have systematic uncertainties of approximately 20 %.

	Probability(%)	
P (GeV/c)	π	K
2.0	0.35	0.40
2.5	0.40	0.43
3.0	0.41	0.40
3.5	0.39	0.36
4.0	0.38	0.34
4.5	0.37	0.33
5.0	0.34	0.30
5.5	0.30	0.29
6.0	0.22	0.29